Thermomechanical Degradation Mechanisms of Silicon Photovoltaic Modules

By

Michael Owen-Bellini

November 2017

Abstract

The durability and lifetime of photovoltaic (PV) modules is one of the chief concerns for an industry which is rapidly approaching maturity. Guaranteeing the economic viability of potential PV installations is paramount to fostering growth of the industry. Whilst certification standards have helped to improve the reliability of modules, with a significant reduction in early failures, long-term performance degradation and overall lifetimes are yet to be addressed in a meaningful way. For this, it is necessary to quantify the effects of use-environment and module design.

Long-term degradation of the solder bonds in PV modules causes steady power loss and leads to the generation of more devastating, secondary mechanisms such as hot-spots. Whilst solder bond degradation is well-recognised and even tested for in certification protocols, the potential rate of degradation is not well understood, particularly with respect to different environmental conditions and material selection. The complex nature of a standard silicon PV module construction makes it difficult to observe the stresses experienced by the various components during normal operation. This thesis presents the development of a finite-element model which is used to observe the stresses and strains experienced by module components during normal operating conditions and quantifies the degradation of solder bonds under different environmental conditions.

First, module operating temperatures are examined across a range of climates and locations to evaluate the thermal profiles experienced by modules. Using finite-element techniques, the thermomechanical behaviour of modules is then simulated using the same thermal profiles and a quantification of solder bond degradation potential in each location is achieved. It is shown that hot climates are responsible for the highest degradation potential, but further to this, hot environments with many

clear sky days, allowing for large swings in module temperature, are significantly more damaging. A comparison is drawn between indoor accelerated stress procedures and outdoor exposure, such that an equivalence between test duration and location-dependent outdoor exposure can be determined. It is shown that for the most damaging climate studied, 86 standard thermal cycles is appropriate for one-year of outdoor exposure whereas the least damaging environment would require 11 standard thermal cycles. However, these conclusions may only be applicable to the specific module design which was modelled as the material selection and interaction within a device plays a major role in the thermomechanical behaviour and degradation potential.

In addition to a study on the influence of use-environment, a study on the influence of the encapsulating material is conducted with a particular focus on the effects of the viscoelastic properties of the materials. It is shown that the degradation of solder bonds can vary depending on the encapsulating material. Furthermore, the intended use-environment could inform the selection of the encapsulating material. The temperature-dependency of the material properties means that some materials will mitigate thermomechanical degradation mechanisms more than others under certain conditions i.e. hotter or colder climates.

Acknowledgments

I would like to express my most sincere gratitude to my supervisors, Prof. Ralph Gottschalg and Dr. Tom Betts for the opportunities they have provided me as well as the support, advice and kick up the backside when I needed it.

Additional thanks go to Dr. Jiang Zhu for all of his assistance and advice during this time, and to Daniel Montiel-Chicharro and Kenan Isbilir for their help in the lab and for the engaging and useful discussions of the work. Acknowledgments are also made to Prof. Philip Eames for providing access to the rheometer and other lab equipment.

Special thanks go to Nayia Arnou, George Koutsourakis, Elena Koubli, Karl Bedrich and Farhad Anvari Azar who joined me in this experience and have made my time at CREST a memory worth cherishing.

The Applied Photovoltaics Group and CREST as a whole is a community which I have been proud to be a part of and cannot be more thankful for. While I feel that it can never be replaced, I only hope that I will find myself working in a similar collaborative and supportive environment in the future.

Lastly, but most importantly, I wish to thank my parents, to whom I owe everything

Contents

Chapter 1

Introduction

Photovoltaic (PV) technology is one of the major pillars capable of supporting a secure and sustainable future provided for by renewable energies. The growth of global installed PV capacity has been spectacular over the last decade, stimulated by advances in technology, reductions in manufacturing costs and support through political instruments such as feed-in tariffs. In order to maintain this level of growth, assurances need to be made on the financial viability of potential installations. The levelised cost of energy (LCOE) can be defined as the total cost of energy produced by an electricity generating system over its lifetime. It is an important metric for evaluating and justifying the economic feasibility of a potential PV installation. The LCOE considers all of the systems lifetime costs including maintenance, fuel, taxes and insurance which are divided by the system's expected lifetime power output. Assuring PV module reliability and longevity is critical for LCOE.

Decades of research on PV module reliability has created a strong foundation, enabling the growth of the PV industry through certification testing and quality assurances. Certification testing of PV modules is a complex task due to the long-term nature of module degradation and the physical mechanisms involved. Research has led to many intermediate steps for standardised type-approval testing procedures which has created a strong foundation, supporting the growth of the PV industry. The most recent and widely accepted version of this is "Terrestrial photovoltaic (PV) modules – Design qualification and type approval" by the International

Electrotechnical Commission, referred to as IEC61215 [1]. The IEC61215 lays down the requirements for the design qualification and type-approval of PV modules suitable for long-term operation in general open-air environments. Accelerated testing procedures are mandated by the standard. They require that manufacturers subject their modules to extreme conditions to quantify their susceptibility to known failure mechanisms. Despite the relative success of IEC6125 and its positive impact on the industry [2], it harbours some very fundamental shortcomings. Firstly, the tests outlined are mechanism-specific, that is, they were designed specifically to reproduce known failure mechanisms. As a result, modules which pass certification have experienced failures in the field simply because the testing procedures do not identify those failures, with some examples being snail trails or potential-induced degradation [3][4]. Secondly, the IEC6125 maintains a simple pass or fail criteria, and provides no useful information on the potential degradation rate which can be expected in the field. This is particularly troubling when manufactures provide 25-year operating warranties on modules based on IEC61215 without there being any scientifically-supported basis for this. Furthermore, the standard is "one-size-fits-all" and does not address climate-specificity.

Of the most commonly reported field-failure mechanisms, degradation of the solder bonds ranks amongst the highest, particularly in hotter environments [5][6]. The steady degradation of bonds results in a gradual loss of conductivity between the cells and the interconnecting ribbons. Other secondary effects are also attributed to the degradation and failure of bonds, such as hot spots, which are localised regions of extremely high temperatures in the module, causing severe damage to other parts of the module and facilitating a rapid degradation in output power. The structural integrity of the solder bonds is tested for in the IEC61215 procedures, however, the relevance of these tests to real-world environments is not fully understood. Any

conclusions from the tests relating to the actual degradation rates which could be expected in the field and particularly in different environments cannot be drawn. This is, in large part, due to a lack of understanding of the thermomechanical behaviour of the modules within different environments and how the IEC61215 tests related to that.

The thermomechanical behaviour of PV modules is investigated in this work with respect to different operating conditions. The impact this has on the solder bonds is studied and the IEC61215 testing procedures are brought under scrutiny in order to determine their relevance, if any, to solder bond lifetime. In addition to this, the influence of the encapsulation material is also investigated, as different polymeric materials exhibit a complex response to temperature which factors in heavily to the thermomechanical behaviour of modules.

Chapter 2 introduces the typical structure and design of modern PV modules and provides a description of the most common materials used for each component as well as the parameters which are used to define the electrical characterisation of devices. Chapter 3 then provides a concise review of the degradation mechanisms associated with module power loss, with a particular focus on thermomechanical degradation mechanisms and the procedures which are in place to test for susceptibility to these mechanisms. The work in this thesis addresses thermomechanical behaviour using the theory of solid mechanics. As such, relevant theory and modelling techniques are discussed in Chapter 4. Chapter 5 analyses module temperature profiles across 9 different locations to characterise properties such as maximum observed temperatures, rate of change of temperature, magnitude and frequency of temperature changes. These properties are then used for cross-examination in later chapters. Chapter 6 discusses the development of the finite element model which is used to analyse thermomechanical behaviour and quantify solder bond degradation for the 9 locations introduced in Chapter 5. The chapter examines the stresses and

strains induced in module components during thermal cycling, which arise from mismatched thermal expansion coefficients. Solder bond degradation potential for each location is cross-examined with the analysis of module temperature profiles presented in Chapter 5 to determine correlations between profile characteristics and identify critical environmental factors. The analysis conducted in Chapter 6 is done so for a single module design with specific materials. It is anticipated that a different material selection will influence the degradation potential. Chapter 7 focuses on the influence of the encapsulant material, with special consideration given to the viscoelastic properties of these materials and their dynamic behaviour which is heavily dependent on temperature.

Chapter 2

Silicon Photovoltaic Modules

2.1 Introduction

A photovoltaic (PV) module is the central component for a solar energy system and is responsible for the conversion of sunlight into electrical power. Whilst regarded as being highly stable and reliable, PV modules suffer from degenerative effects resulting from their inherent exposure to outdoor environments, of which, thermomechanical degradation is amongst the highest [7]. The following chapter discusses the standard structure of a PV module, the common materials used and the thermomechanical degradation mechanisms contributing to their reduction in performance.

2.2 Photovoltaic Module Structure and Materials

As of 2016, Silicon wafer-based photovoltaic (PV) modules account for 93% of worldwide production, with thin-film technologies such as Cadmium Telluride (CdTe) and Copper Indium Gallium diselenide (CIGS) making up the remaining 7% [8]. A standard silicon wafer-based PV module is structured as a layered assembly of different materials, each with a specific role. The active layer is made up of solar cells which are connected in series via solder-coated copper ribbons (or interconnects). This is entirely encapsulated within a polymer, most commonly Ethylene Vinyl Acetate (EVA), which provides mechanical stability and binds together a protective glass front cover and polymer back sheet. The final assembly is then mounted within a rigid

aluminium frame with a rubber inlay buffer, providing additional structural support and resistance to moisture ingress from the edges. The electrical contact points are housed within a junction box which is attached to the rear surface of the module.

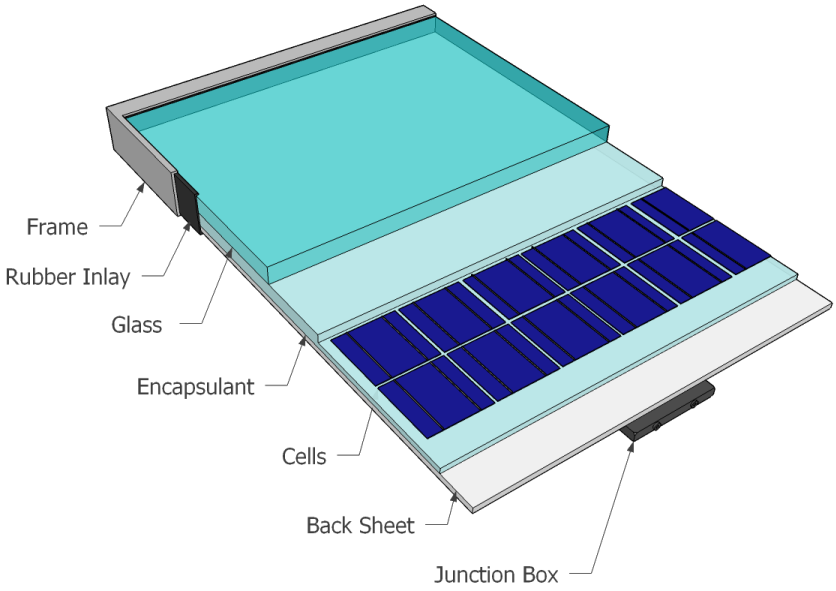

Figure 1: Standard Silicon PV module configuration

Crystalline silicon solar cells

Crystalline silicon solar cells are processed from silicon wafers with a typical thickness of around 0.18 – 0.22 mm [9]. A standard solar cell is made up of a phosphorus or boron-doped Silicon diffusion layer, a passivation layer of Silicon nitride, a front surface of pyramid structures, a metallisation grid of silver paste at the front and a metallisation of aluminium on the rear surface. Typically, cells are manufactured into sizes of 125mm x 125mm or 156mm x 156mm with a pseudo-square or full-square shape. Cells are extremely brittle and susceptible to breakage as a result of mechanical

loading and are therefore laminated within a polymeric material to provide the mechanical stability necessary to prevent breakage.

Interconnects

Highly conductive solder-coated, copper-based flat wires, known as ribbons, are the predominant material used to make the connections between cells. The ribbons have typical thicknesses in the range of 0.2 to 0.5mm. The connections are soldered using either Tin-Lead or lead-free solder alloys from the front surface of one cell to the rear surface of the neighbouring cell, such that current transfer from one cell to the other is made in series. Each cell may have two or three interconnectors, depending on the design. The soldering process is known to induce thermomechanical stress to the cells, which can later become problematic [10].

Encapsulant

The cells and interconnects are completely encapsulated within a protective adhesive layer, which bonds all the components together. The primary role of the encapsulant is to provide the cells with mechanical stability and protection from external factors such as moisture, wind and ultra-violet (UV) light. In addition to this, the encapsulant provides a means of dissipating thermal energy generated by the cells [11] and maximises the optical coupling between the different layers [12][13]. There are many different materials available on the market as encapsulants which can provide, to lesser or greater extents, the general functional requirements.

Whilst many different materials have been used previously for encapsulation, a series of selection and development experiments conducted by the Jet Propulsion Labs (JPL) found that Ethylene Vinyl Acetate (EVA) had the highest quality-to-cost ratio and, as a result, is the most widely used material in the industry today [14]. EVA is a polyolefin, which is a class of polymer produced from simple monomers. It offers very

desirable characteristics such as high optical transmittance, weather resistance and mechanical stability whilst also being easy to process for a relatively low cost. Earlier formulations of EVA suffered from ultra-violet (UV) radiation induced photodegradation, which caused discoloration and optical transmission losses [15]. This problem has since been improved upon through the addition of UV absorbers and stabilisers, however this has not solved the problem entirely since the additives tend to deplete with time [16].

Poly-vinyl Butaryl (PVB) was one of the earlier materials utilised as an encapsulant. PVB offers strong bonding properties and high transparency, but is highly sensitive to UV and moisture. Improvements have been made to the PVB formulation to reduce these sensitivities and is a popular encapsulant for thin-film and glass-glass modules, having been shown to offer greater stability than other materials for such configurations [17].

Ionomer-based encapsulants are a newer generation of material which have shown remarkable performance over older materials in terms of transparency, mechanical strength and resistance to yellowing and UV-induced degradation [18]. One of the key highlights for ionomer-based encapsulants is the substantial increase in volume resistivity, up to four times higher than PVB. Ionomer-based encapsulants have been shown to eliminate potential-induced degradation (PID) and snail trails, two degradation mechanisms associated with many highly publicised system failures in recent years [19][20].

As polymers, all of these materials exhibit viscoelastic properties, undergoing changes in viscosity and elasticity with temperature and time. The impact this has on the thermomechanics of the module, whose operating temperatures can extend beyond 75°C, is the focus of chapter 7.

Bypass Diodes

Cell or interconnect damage, partial shading or mismatching can cause a cell to generate less current than the rest of the cells in a string. The defective cell is reverse biased and behaves as a load which dissipates power generated by the other cells as heat [21]. Typically, a single bypass diode is connected in parallel with a reverse polarity to a group of cells such that when a defective cell is reverse biased to a sufficient degree, the bypass diode becomes forward conducting and short-circuits the group of cells. This alleviates the power being dissipated by the defected cell and reduces the potential for module damage.

Front Cover

Whilst light-weight polymeric front sheets have been used in the past, the mechanical strength, optical transmittance and general weatherability was less desirable than glass. Therefore, most PV modules have a tempered low-iron float glass front sheet. Glass provides high optical transmittance, mechanical stability, impact resistance and electrical insulation. The standard thickness for the glass front sheet is around 4mm, which makes up approximately 70% of the total thickness of the module and therefore dominates much of the mechanical behaviour of a device [22]. Anti-reflective coating is sometimes used on the front-side of the glass to reduce reflectance losses, and a UV absorption screen might also be used on the rear-surface to minimise the influence of UV on the encapsulating layer.

Back Cover

The rear surface of a module is made up of a protective layer which reduces the impact of environmental factors such as UV and moisture. Whilst glass back layers have been used in the past and are currently a remerging trend, it was found that they prevented the release of bi-products generated during normal operation, leading to increased

degradation [23]. In addition to this, glass increases the weight and cost of a module considerably. Multi-layered polymeric film backsheets allow for an increased thermal dissipation [24] cover glass, as well as the release of aforementioned bi-products. The typical structure of these backsheets, as illustrated in Figure 2, include an outer layer, core layer and inner layer which are sandwiched together using adhesive inter-layers. Materials such as polyethylene terephthatlate (PET), Polyvinylidene fluoride and EVA are used for these layers. Some popular combinations include TPE (Tedlar™/PET/EVA), TPT (Tedlar™ /PET/Tedler), PPE (PET/PET/EVA), PVDF (PVDF/PET/PVDF).

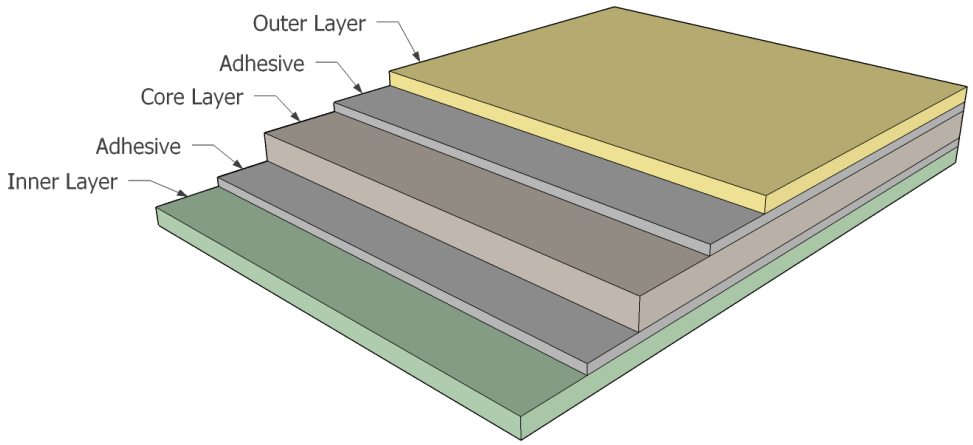

Figure 2: Typical multilayer back sheet structure

Frame

A frame, typically aluminium, is used around the edge of the module to provide mechanical stability. The frame also contains a rubber inset to seat the layers, and a silicone sealant is used to provide additional protection from moisture ingress.

Junction Box

The junction box provides a protective housing for the electrical contacts which are fed through the rear side of the module. The junction box is typically adhered to the backsheet using an adhesive. Failures of the junction box are predominantly associated with improper installation and can be catastrophic, leading to electrical arcing and fire [25].

2.3 Electrical Parameters

The primary metrics used to characterise the performance of a device are the maximum power point, P_{MPP}, short-circuit current, I_{SC}, the open-circuit voltage, V_{OC}, and the fill factor, FF, which is defined as (1).

$$FF = \frac{V_{MPP}.I_{MPP}}{V_{OC}.I_{SC}} \tag{1}$$

Where V_{MPP} and I_{MPP} are the voltage and current at P_{MPP}. The overall performance of a photovoltaic device can be observed as the conversion efficiency, η, which is the ratio of maximum electrical power output, P_{MPP}, to the power of the incident irradiance, P_i, as illustrated in (2).

$$\eta = \frac{V_{OC}.I_{SC}.FF}{P_i} = \frac{P_{MPP}}{P_i} \tag{2}$$

These parameters can be used to quantify the performance of a device and can be used to determine degradation modes and diagnose the physical mechanisms. For example, in the case of solder bond fatigue, degradation of the solder layer causes a loss in conductivity between the cell and the ribbon which amounts to an overall increase in series resistance, which can be observed through a decreasing V_{MPP} and FF.

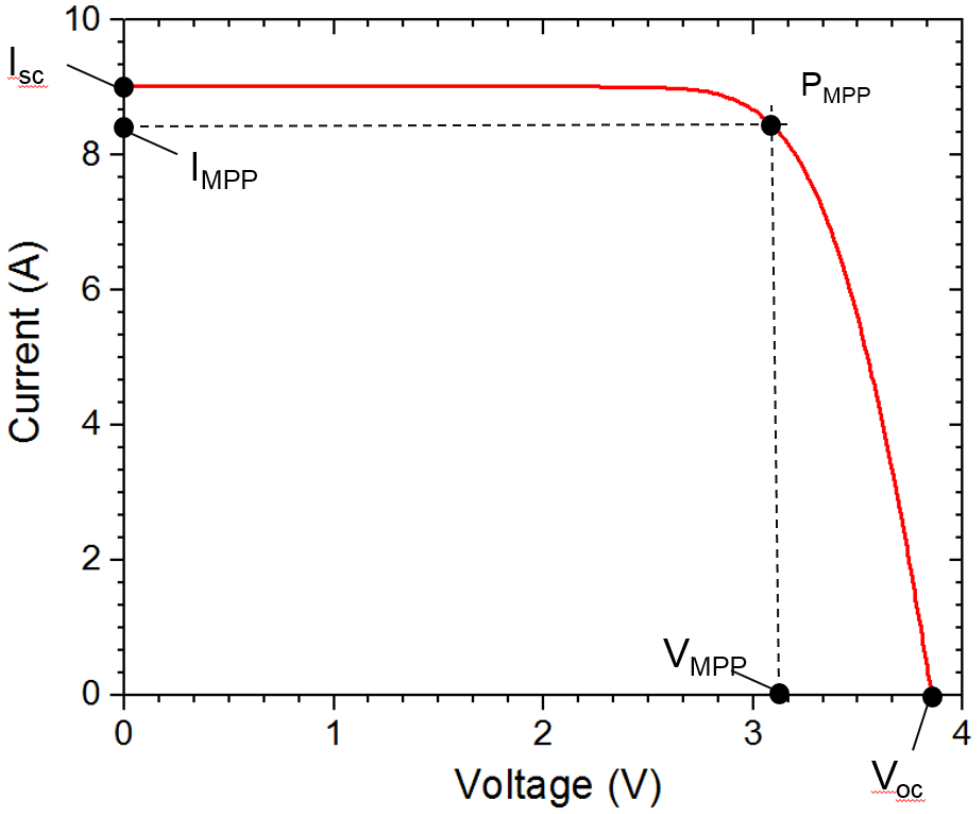

Figure 3: IV curve fora 6-cell mini-module

Devices are typically measured under Standard Test Conditions (STC) of 25°C ambient temperature, 1000W/m² irradiance power under the AM1.5 spectrum, illustrated in Figure 4.

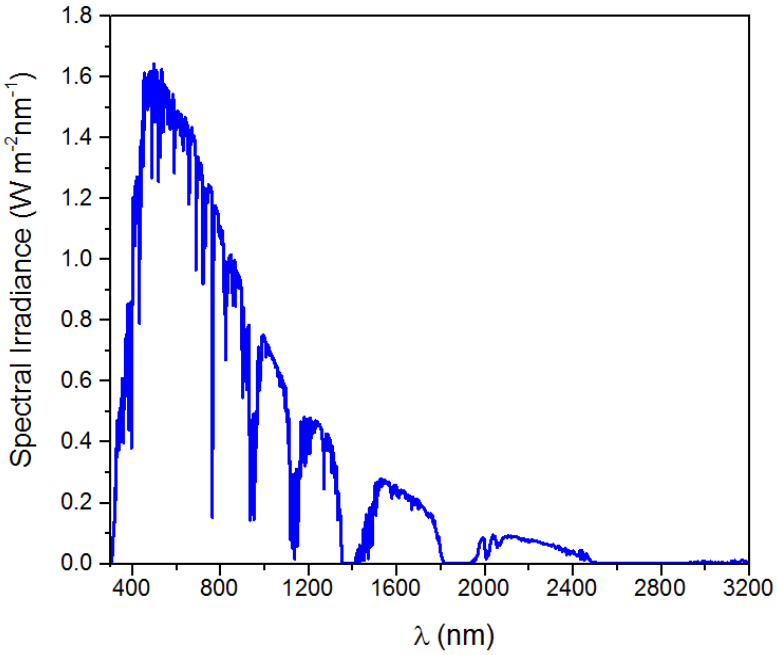

Figure 4: AM1.5G Spectrum

Whilst STC is not entirely representative of real outdoor conditions, it provides some means of benchmark standardisation

Chapter 3

Module Degradation and Testing

3.1 Introduction

Whilst PV modules are recognised as being highly reliable they are, of course, not altogether immune to degradation and failure. Modules exposed to outdoor environments are subject to unavoidable thermomechanical stresses which trigger certain physical mechanisms detrimental to the overall performance of the device.

3.2 Observed Failure Modes

Identification of field failure mechanisms has been an ongoing topic of research since the block procurement program by the Jet Propulsion Lab in the 1970's and 80's [26] [27]. Ribbon and solder bond fatigue, cell cracks, encapsulant delamination and hot spots are the most commonly observed failure mechanisms associated with thermomechanical stress [28] which, unsurprisingly, is particularly true for hot climates [29][30][31].

Solder Bond Fatigue

Solder bond degradation is amongst the highest causes of module degradation and is the primary focus of this work [32][33]. This type of degradation mechanism is, of course, not unique to PV modules, and has been the focus of an extensive research area within the microelectronics packaging industry. Fatigue failures are attributed to

thermomechanical stresses in the soldered connections, brought about by differences in the coefficient of thermal expansion (CTE) between the solder and ribbon/cell. The mismatch in CTE causes strains in the solder bond which, over time, contributes to the mechanical deformation of the bond leading to the initiation and propagation of cracks and voids. A metallurgic study of solder bonds conducted by King et al [34] found that during normal operation, the bonds become more brittle, with a segregation of the metals (tin and lead) leading to an increased likelihood of crack development. This structural change in the solder bonds leads to a loss of electrical conductivity, characterised by an increasing series resistance, leading to a reduction in performance, until an eventual complete disconnection between ribbon and cell occurs.

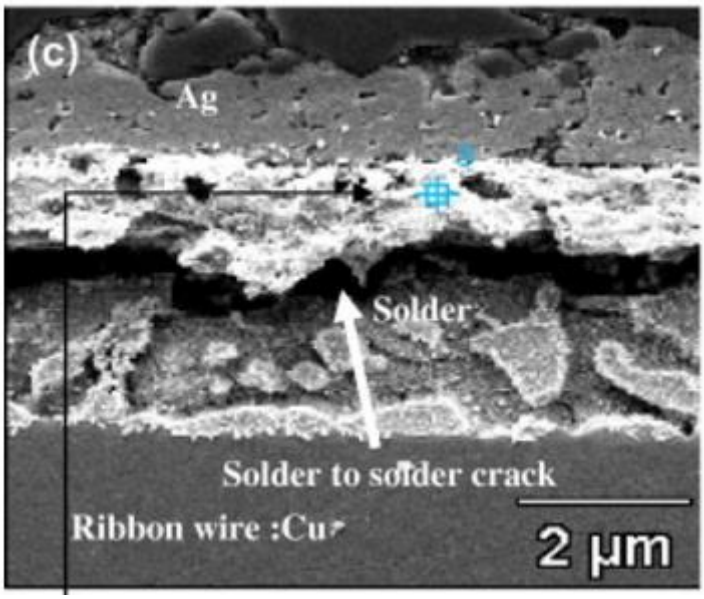

Figure 5: Cross-sectional scanning electron microscope (SEM) image showing a crack formation in a solder bond belonging to a 25-year old field-aged module [35]

In addition to the increased series resistance, interconnect degradation leads to excessive heating of the module, hot spot generation, burning of the back sheet and arcing of the solder joint [32][36]. During thermal changes, expansion and contraction of the assembly causes a displacement of the cells. This displacement results in mechanical loading of the ribbons contributing to fatiguing mechanisms and eventual breakage [37].

Hot Spots

Hot spots are a localised region within a PV module which exhibit temperatures significantly higher than the average operating temperature of the module. They present a clear risk of irreversible damage for PV modules including backsheet damage, glass breakage, loss of electrical insulation and even fire. An investigation into the damage posed by hot spots by Munoz et al [38] showed hot spots which reached temperatures upwards of 175°C, sufficient to cause melting of most commercial encapsulants. Hot spots occur because of reduced short-circuit current in the affected cell which causes the cell to be reverse biased and act as a dissipating load for the other cells in the string [39]. The reduction in current generation could be due to partial shading, cell damage or interconnect failure [40].

Cell Cracks

Cell cracks and breakages are another common failure mechanism often seen in the field. Cracks in PV cells are often initiated prior to arriving at the installation site [41]. Soldering [10] and lamination [42] during fabrication, as well as mechanical loads during transportation [43][44][45] are known to subject mechanical stress to the cells and initiate micro-cracks, which can then be propagated in the field due to thermomechanical and snow/wind loads [42][46]. The potential loss of power due to cracks is highly dependent on the orientation of the crack. Often times cracks can have little to no impact on the overall performance of the device, however, a single crack

may propagate and eventually cause electrical isolation of some of the cell area, which can significantly reduce the power output [47]. Kajari-Schröder et al [48] demonstrated the potential for cell area disconnect according to the cracks location on the device. It was shown that cracks parallel to the bus bars were most at risk of causing a separation and that the potential separation was in the region of 20-40% of the total cell area, furthermore, such cracks were found to be the most frequent [49]. Whilst the criticality of crack orientation and distribution is quite well understood, the rate of crack propagation in real environments, where thermomechanical strains vary, is not.

Encapsulant Degradation

Degradation of the encapsulation system of a PV module has both a direct impact on the reduction in module performance and an indirect impact through the initiation of secondary degradation mechanisms. Thermal cycling is reportedly responsible for most adhesion failures in modules [50]. Thermal stresses from expansion and volumetric changes due to interfacial strains leads to delamination. The delamination can occur at any of the interfaces such as glass/encapsulant, cell/encapsulant or backsheet/encapsulant. Delamination causes light transmission losses and reduces the efficiency of the moisture barrier, increasing the potential for corrosion of metal elements [51]. In addition to this, areas which have suffered from delamination also experience reduced heat dissipation, further contributing to thermal fatigue and the generation of hot spots [28]. McIntosh et al [52] demonstrated that following damp-heat conditions of 85°C / 85 % relative humidity, the light transmission of EVA is reduced and that it is likely due to a scattering of incident light or an increase in the light absorption coefficient due to the absorption of moisture. Changes in the mechanical properties of EVA are also possible due to moisture absorption. Reduction in molecular mobility and consequential plasticisation effects can occur, which lowers

the glass transition temperature and reduces elastic modulus of the EVA [53]. Changes in mechanical properties, such as elastic modulus, could reduce the effectiveness of EVA's protection against mechanical loads for cells and metal bonds, leading to increased strains and rate of fatigue. Another concern relating to the moisture absorption of EVA is the breakdown of hydrolytic bonds within the polymer, resulting in the production of acetic acid. The generation of acetic acid further contributes to corrosion of the metallisation [54] and can also catalyse discolouration of the EVA [16]. Discolouration is a widely acknowledged and commonly reported in field-aged modules. Discoloured EVA exhibits a change in colour from clear to yellow-brown which has the potential to reduce optical transmittance in a significant way. Pern et al demonstrated that a variety of factors can influence the discolouration of EVA including the depletion rate of the UV absorber and stabiliser, as well as the intensity of UV exposure and the permeability of the backsheet [55][56].

Back sheet Degradation

Exposure to elevated temperatures can cause a degradation of the backsheet depending on the type of material. PET is amongst the most commonly used core materials for a multi-layered backsheet and is known to be susceptible to degradation by hydrolysis from water vapour [57]. Hydrolysis is the addition of water vapour to a molecule which results in the separation of the molecule into smaller molecules, reducing the tensile strength of the material. This process is accelerated at elevated temperatures, and so the dominant stress factors contributing to the degradation of PET are water vapour and temperature [58]. UV exposure is also known to contribute significantly to the discoloration, cracking and embrittlement of polymeric backsheets which also reduces the tensile strength [59][60]. It is unclear if or how the loss of mechanical strength of the backsheet affects the thermomechanical behaviour of the module and the associated degradation mechanisms.

3.3 Accelerated Testing

Qualifying PV modules for their use in the field requires that their susceptibility to degradation mechanisms are evaluated. This way some guarantee can be made that the modules will not fail early i.e. within 5 years of operation. Developing appropriate tests presents a difficult challenge. The requirements of the test are to reproduce the degradation mechanisms seen in the field at an accelerated rate which means subjecting modules to harsh environmental conditions, but not so harsh as to introduce unrealistic failure modes.

Development of accelerated testing standards has been a lengthy process which began in the 1970's with JPLs block procurement program. Accelerated test protocols have undergone multiple iterations before eventually arriving at the standards which are widely used today. The International Electrotechnical Committee Standard 61215 (IEC61215) lays down the requirements for the design qualification and type-approval of PV modules suitable for long-term operation in general open-air environments [1]. Accelerated testing procedures are mandated by the standard, which requires manufacturers to expose their modules to extreme conditions to qualify their resistance to known failure mechanisms.

Thermal Cycling

Thermal cycling was one of the first tests developed in the earliest accelerated ageing programs and has remained since as one of the most important tests. The thermal cycling 200 (TC200) accelerated test aims to reproduce thermomechanical degradation mechanisms resulting from thermal stresses during normal operating conditions. The primary function is to challenge the structural integrity of the solder bonds, interconnects, cells and laminate. The module is subjected to cycling temperature limits of -40°C ± 2°C and +85°C ± 2°C with minimum dwell times of 10 minutes at each

extreme and a maximum ramping rate of 0.028 K/s per the profile in Figure 6. The cycling profile can be seen in Figure 6. A current injection within ± 2% of peak power current (Impp) is also applied at temperatures above 25°C to simulate the effects of irradiance exposure during the day.

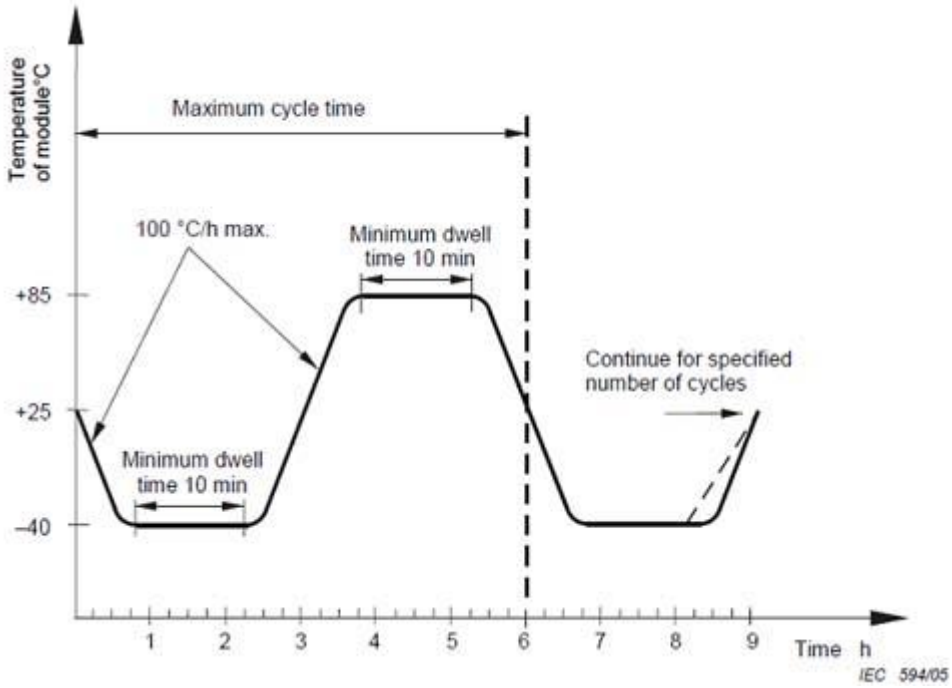

Figure 6: IEC61215 Thermal Cycling 200 Temperature Profile

Figure 7 presents the IV curves for a 6-cell mini-module following 1200 thermal cycles with measurements conducted at 400 cycle interims. Total power loss following 1200 cycles is 30%. Loss in power can be attributed to an increasing series resistance due to a degradation of the solder interconnects, as shown in Figure 8.

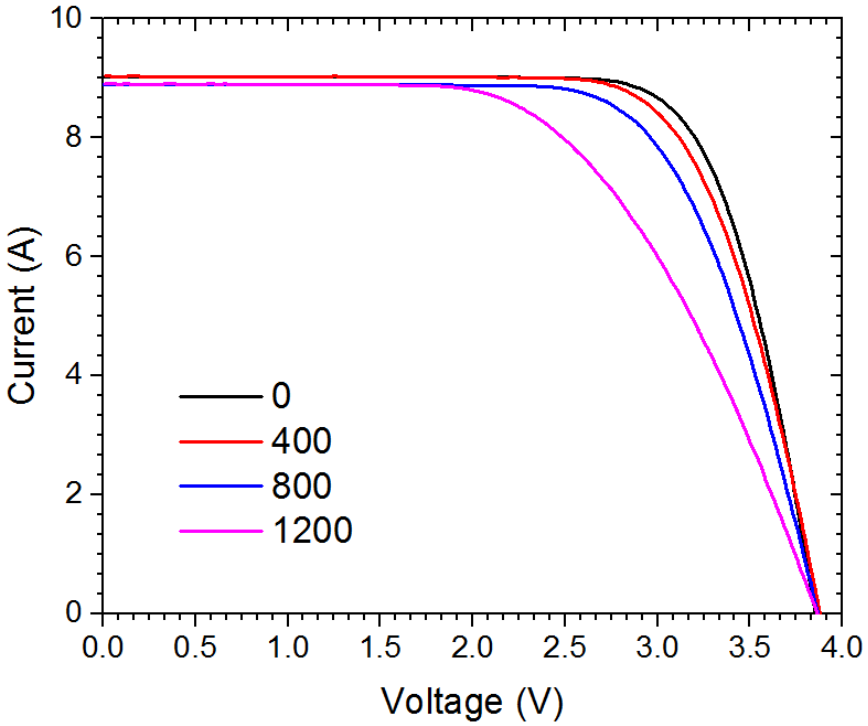

Figure 7: IV Curve for a module following 1200 thermal cycles

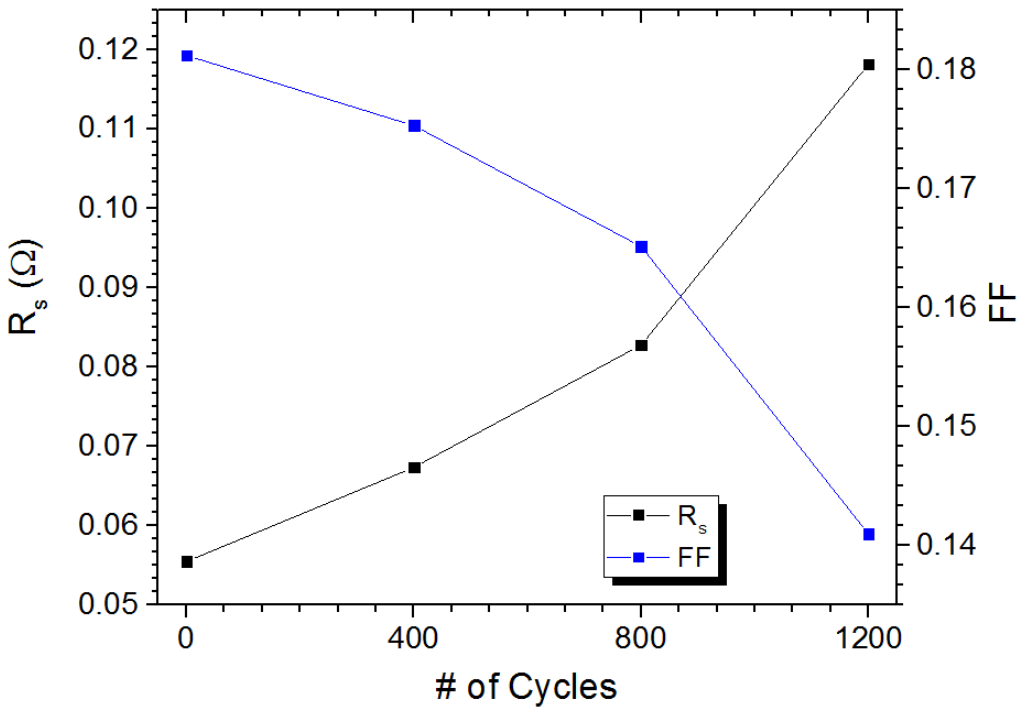

Figure 8: Change in series resistance and fill factor following 1200 thermal cycles

Electroluminescence (EL) imaging is a useful tool which is used to characterise and observe degradation mechanisms in aged PV devices. In EL, current is injected into a cell (or module) and light is emitted as a result of recombination of carriers. Light output increases with local voltage, so that regions with poor contacting show up as dark areas. This is useful for identifying solder bond failure, as the loss of conductivity can be observed as dark areas around the degraded contact. Figure 9 shows an EL image for the mini-modules before and after 1200 thermal cycles. The degradation of the solder bonds, which was inferred from the IV curves, can now be seen. The loss of structural integrity of the solder results in a reduced conductivity, thus showing up as dark areas.

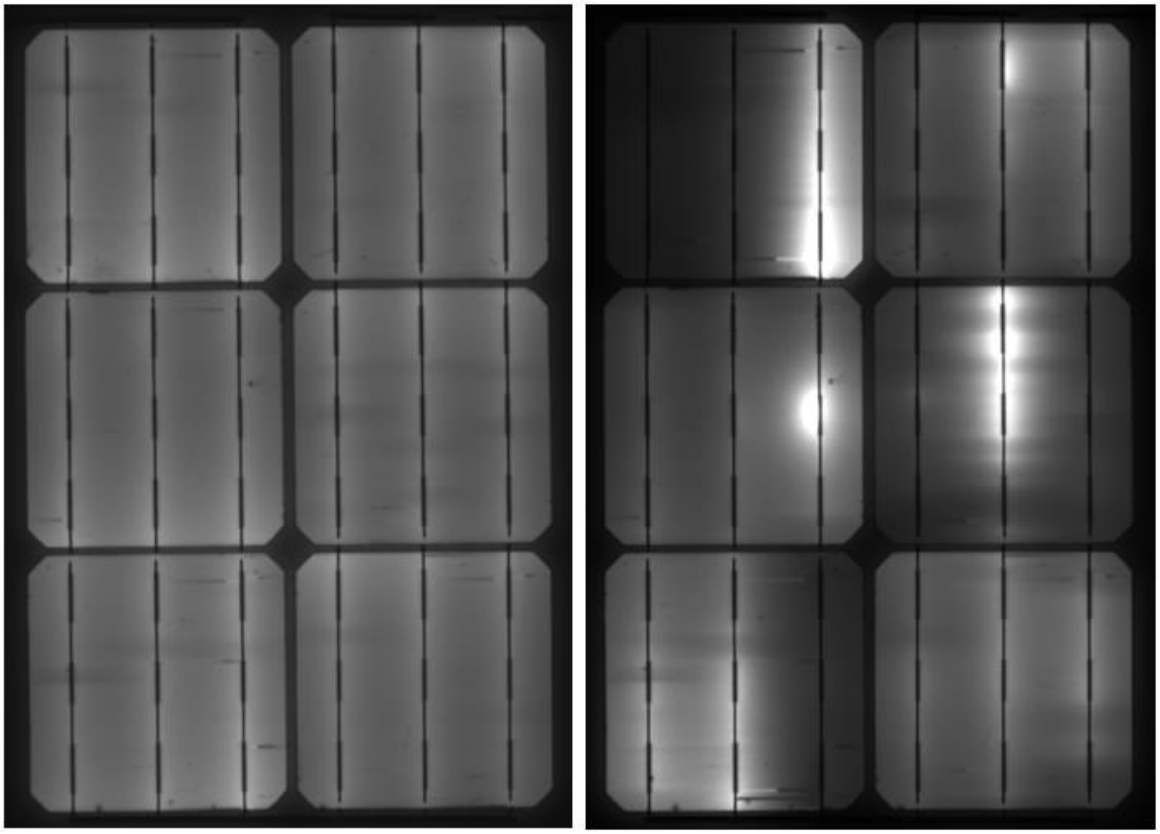

(a) (b)

Figure 9: Electroluminescence image of a 6-cell mini-module (a) post-lamination and (b) after 1200 standard thermal cycles.

Accelerated Certification Shortcomings

Currently, all module designs that reach the market are certified to IEC61215 standards and are typically given a 25-year warranty based on the certification. Since the establishment of the IEC61215, module warranty returns have reduced significantly indicating that the tests have been successful in identifying and eliminating module designs and material types that suffered from early failures [61]. These days, most modules can pass all the criteria outlined in the IEC61215 standard with ease and consumers are asking for greater assurances from manufacturers. As such, manufacturers are extending their testing criteria far beyond the requirements of IEC61215 [2][62][63][64].

It has been shown that linearised assumptions for module degradation rates (R_d) results in a higher calculated LCOE when compared with using a non-linear R_d [65].When R_d begins to increase as a function of time, a module is considered to be in the wear-out phase. During this phase, failure modes may be the result of a combination of multiple fatiguing mechanisms. A modules R_d may follow a linear trajectory for the majority of its life, until fatiguing mechanisms give way to failure and the introduction of a more severe failure mechanism, completely changing the degradation profile. An example of this might be the generation of a hot spot which follows a solder bond breakage after 20 years of fatigue damage. The introduction of the hot spot dominates the degradation of the module in a much more severe way, completely deviating from what might have been an otherwise linear R_d.

Whilst the IEC61215 testing procedures are useful from a design and reliability perspective, a strong correlation between the tests and real world degradation rates remains to be determined. The IEC61215 tests were designed to specifically reproduce known failure mechanisms at the time, and as such, does not identify and quantify long-term wear-out mechanisms. Any indication of actual degradation rates cannot

be inferred from the mandated test protocols. For this reason, research trends are shifting from reliability to durability testing such that service life estimations and actual degradation rates in outdoor environments can be ascertained. As part of the durability research efforts, there is a greater focus on climate-specific durability. Extensive reviews by Jordan et al [66][67] show that the rate of degradation of modules is higher in hotter climates due to the additional thermomechanical stresses subjected to the modules. Increasing stakeholder confidence is key to supporting the continued growth of the industry. More accurate determinations of LCOE are fundamental to this. An increased understanding of the degradation potential of modules, particularly under different environmental conditions, is an important aspect to increasing the accuracy of LCOE calculations and thus increasing stakeholder confidence.

3.4 Conclusions

Thermomechanical degradation mechanisms share a significant portion of the causes of PV module failure and wear-out. Degradation of the solder bonds between the cells and ribbons is amongst the highest. Whilst solder bond degradation can be tested for using accelerated ageing, there is no established link between the results of accelerated ageing and the outdoors. The tests do not provide any information about the rate of degradation which could be expected in the field. Additionally, the tests do not address the variability of climates or the variability of module design and its effect on degradation. This thesis addresses these issues by quantifying the degradation potential of solder bonds in different climates and also evaluating the impact of different materials, namely for the encapsulation layer.

Chapter 4

Continuum Mechanics and Thermal Modelling

4.1 Introduction

Continuum mechanics deals with the analysis of the mechanical behaviour of materials by modelling them as continuous bodies, ignoring the fact that the materials are actually made up of discrete particles separated by vacant space. This branch of physics covers solid and fluid mechanics, as well as the areas in between such as polymer mechanics. This chapter briefly introduces some of the concepts of continuum mechanics, which are applied in this work using the finite-element method, to analyse the thermomechanical behaviour and degradation mechanisms of PV modules. Additionally, modelling of the operating temperatures of modules is discussed.

4.2 Solid Mechanics

When subject to external and internal forces, such as temperature changes, solid materials exhibit deformation and motion which gives rise to stresses and strains. The following section provides a concise introduction to the theory of solid mechanics which will be used throughout this work.

Stress, Strain and Material Properties

The most elementary means of defining stress and strain is achieved through the uniaxial deformation example given in Figure 10. A cylinder of initial length, L_0, and cross-sectional area, A_0, is uniaxially loaded with a force, F. The bottom of the cylinder is fixed in place whilst the top is displaced a distance, u. The stress and strain can then be represented as (1) and (2), respectively.

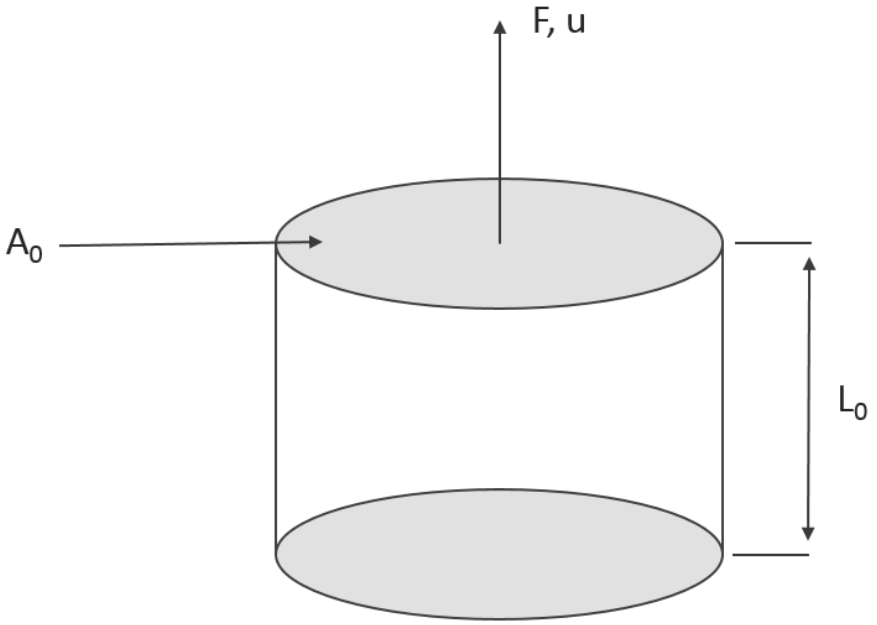

Figure 10: Classical representation of tensile stress and strain for small-strain uniaxial loading

$$\sigma = \frac{F}{A_0} \tag{1}$$

$$\varepsilon = \frac{u}{L_0} \tag{2}$$

Young's modulus, E, is a material property describing the linearity of the stress-strain relationship and can be defined as stress divided by strain. For a uniaxial

stress and strain condition, Hooke's law defines the relationship in an elastic material as (3).

$$\sigma = E\varepsilon \tag{3}$$

In most cases, a multiaxial loading representation, as shown in Figure 11, is more relevant as mechanical bodies often experience more than one type of stress at the same time. This is known as *combined stress*. Here the stresses and strains are characterised by nine components which can be arranged into symmetric 3x3 matrices as in (4) and (5). This is known as the *Cauchy stress tensor* and defines the state of stress at a given point. The stress and strain of each point can be represented by normal and shear stresses, those are stresses perpendicular to the surface and stresses which are parallel to the surface, respectively. The first subscript of a stress or strain quantity represents the *normal* direction of the face and the second subscript represents the stress quantity. So for (4) and (5), components on the diagonal are normal stresses and non-diagonal are shear stresses.

$$\sigma_{ij} = \begin{bmatrix} \sigma_{xx} & \sigma_{xy} & \sigma_{xz} \\ \sigma_{yx} & \sigma_{yy} & \sigma_{yz} \\ \sigma_{zx} & \sigma_{zy} & \sigma_{zz} \end{bmatrix} = \begin{bmatrix} \sigma_{11} & \sigma_{12} & \sigma_{13} \\ \sigma_{21} & \sigma_{22} & \sigma_{23} \\ \sigma_{31} & \sigma_{32} & \sigma_{33} \end{bmatrix} \tag{4}$$

$$\varepsilon_{ij} = \begin{bmatrix} \varepsilon_{xx} & \varepsilon_{xy} & \varepsilon_{xz} \\ \varepsilon_{yx} & \varepsilon_{yy} & \varepsilon_{yz} \\ \varepsilon_{zx} & \varepsilon_{zy} & \varepsilon_{zz} \end{bmatrix} = \begin{bmatrix} \varepsilon_{11} & \varepsilon_{12} & \varepsilon_{13} \\ \varepsilon_{21} & \varepsilon_{22} & \varepsilon_{23} \\ \varepsilon_{31} & \varepsilon_{32} & \varepsilon_{33} \end{bmatrix} \tag{5}$$

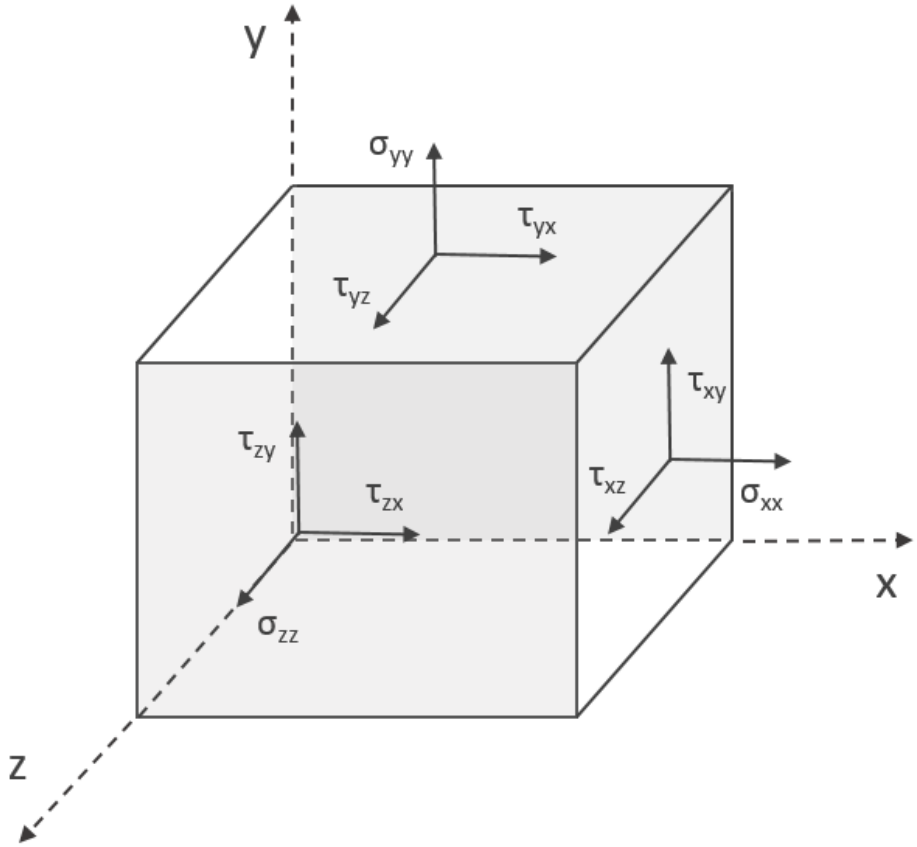

Figure 11: Graphical representation of the components of combined stress in multiaxial loading conditions

For a 3-dimensional state of stress and strain in an isotropic material, the generalised Hooke's law may be represented as (6-8).

$$\varepsilon_{xx} = \frac{1}{E}\left[\sigma_{xx} - v\left(\sigma_{yy} + \sigma_{zz}\right)\right], \gamma_{xy} = \frac{\tau_{xy}}{G} \tag{6}$$

$$\varepsilon_{yy} = \frac{1}{E}\left[\sigma_{yy} - v(\sigma_{xx} + \sigma_{zz})\right], \gamma_{yz} = \frac{\tau_{yz}}{G} \tag{7}$$

$$\varepsilon_{zz} = \frac{1}{E}\left[\sigma_{zz} - v\left(\sigma_{xx} + \sigma_{yy}\right)\right], \gamma_{xz} = \frac{\tau_{xz}}{G} \tag{8}$$

Where v is Poisson's ratio, defined as the ratio of strain transverse to the load direction, ε_y, to the strain in the load direction, ε_x.

Shear stress, τ, is stress which is parallel to the surface of a material. The shear modulus, G, is a material property which defines the relationship between the shear stress and the shear strain, γ, as given by (9).

$$G = \frac{\tau}{\gamma} \tag{9}$$

Principal Stresses and Strains

For every stress tensor, there exists a set of normal vectors, *n*, called *principal directions*. The corresponding stress vectors to the normal vectors are perpendicular to the plane where there are no normal shear stresses. The three stresses parallel to the principal directions are known as *principal stresses.* The relationship between the stress vector, $T^{(n)}$, to *n* can be given as (10).

$$T^{(n)} = \lambda n = \sigma_n . n \tag{10}$$

Where λ is the value of the corresponding normal stress. There exists three perpendicular solutions n_1, n_2, n_3 for which there are three corresponding principal stresses, σ_1, σ_2, σ_3 where $\sigma_1 > \sigma_2 > \sigma_3$. Since (10) is an Eigenvector problem, it may be solved as (11).

$$\det(\sigma_n - \lambda I) = \lambda^3 - I_1\lambda^2 + I_2\lambda - I_3 = 0 \tag{11}$$

Where the tensor invariants I_1, I_2, I_3 can be given as (12-14).

$$I_1 = \mathrm{tr}(\sigma) = \sigma_{11} + \sigma_{22} + \sigma_{33} = \sigma_1 + \sigma_2 + \sigma_3 \tag{12}$$

$$I_2 = \det\begin{bmatrix}\sigma_{11} & \sigma_{12} \\ \sigma_{12} & \sigma_{22}\end{bmatrix} + \det\begin{bmatrix}\sigma_{22} & \sigma_{23} \\ \sigma_{23} & \sigma_{33}\end{bmatrix} + \det\begin{bmatrix}\sigma_{11} & \sigma_{13} \\ \sigma_{13} & \sigma_{33}\end{bmatrix}$$

$$= \sigma_{11}\sigma_{22} + \sigma_{22}\sigma_{33} + \sigma_{11}\sigma_{33} = \sigma_1\sigma_2 + \sigma_2\sigma_3 + \sigma_1\sigma_3 \tag{13}$$

$$I_3 = \det(\sigma) = \sigma_1\sigma_2\sigma_3 \tag{14}$$

Von Mises Stress

The Von Mises stress criterion, also referred to as the equivalent tensile stress, is a scalar value of stress calculated from the Cauchy stress tensor. Von Mises stress is a common approach used to determine the yielding of materials, which occurs when the Von Mises stress reaches a value known as the yield strength. For multiaxial loading conditions, the Von Mises stress, σ_v, may be expressed as (15).

$$\sigma_v = \sqrt{\frac{(\sigma_{11}-\sigma_{22})^2+(\sigma_{22}-\sigma_{33})^2+(\sigma_{33}-\sigma_{11})^2+6(\sigma_{12}^2+\sigma_{23}^2+\sigma_{31}^2)}{2}} \qquad (15)$$

Creep

When subject to mechanical stresses below the yield strength, solid materials have a tendency to slowly move or permanently deform. The rate of deformation is dependent on the properties of the material, temperature and exposure time. With sufficient time and stress magnitude, deformation can become so great that a component is no longer able to perform its function. Such can be the case with solder bonds in PV modules, where creep deformation is a significant contributor to the degradation and failure of the bonds. Figure 12 demonstrates the 3 stages of creep when a material is subjected to a constant stress over an extended period of time. The initial stage, known as primary or transient creep, follows the initial loading period. In this stage strain rate is relatively high, but gradually decreases with time and strain, typically due to a process known as *work hardening* whereby dislocation of the crystal structure of the material from plastic deformation increases ductility. As work hardening and annealing are balanced, the strain-rate becomes constant. This is the secondary stage of creep. Eventually, deformation of the material becomes such that voids and cracks appear, rapidly reducing the materials strength and entering the tertiary stage of creep, where strain-rate accelerates until fracture occurs.

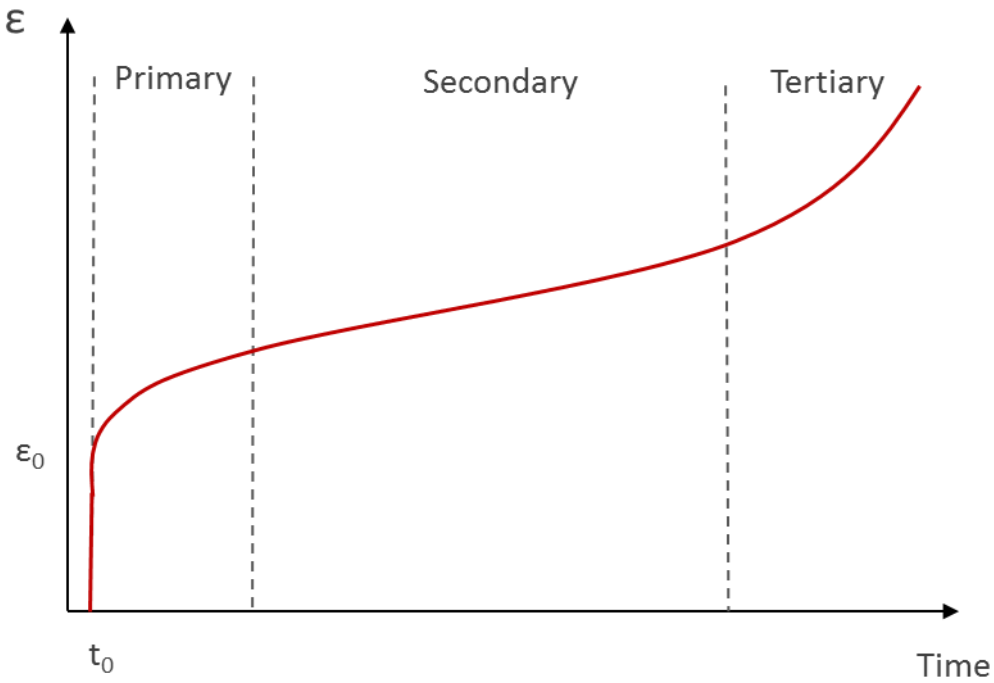

Figure 12: Graph demonstrating creep strain of a material subjected to constant stress over an extended period of time

Thermal Expansion

Materials expand and contract when they are heated and cooled, respectively. The parameter which describes this behaviour is the coefficient of thermal expansion (CTE). In an isotropic material, CTE can be defined as the change in length of a body per degree of temperature change (15).

$$\alpha_L = \frac{1}{L}\frac{\Delta L}{\Delta T} \tag{15}$$

Mismatching thermal expansion properties between materials in a PV module is the primary cause of thermomechanical stress. As a PV module undergoes temperature change, each layer expands or contracts at different rates. Since the layers are bound together, they are unable to expand or contract freely, inducing strains.

4.3 Polymer Mechanics

Polymers are a class of material often referred to as *amorphous solids.* In chemistry terms, they are very large hydrocarbon and hydrocarbon derivative molecules which are made when many monomers are strung together into chains of varying length, see Figure 13. The physical properties of a polymeric material such as melting point, tensile strength, viscosity etc. are strongly dependent on the size and shape of their polymer chains.

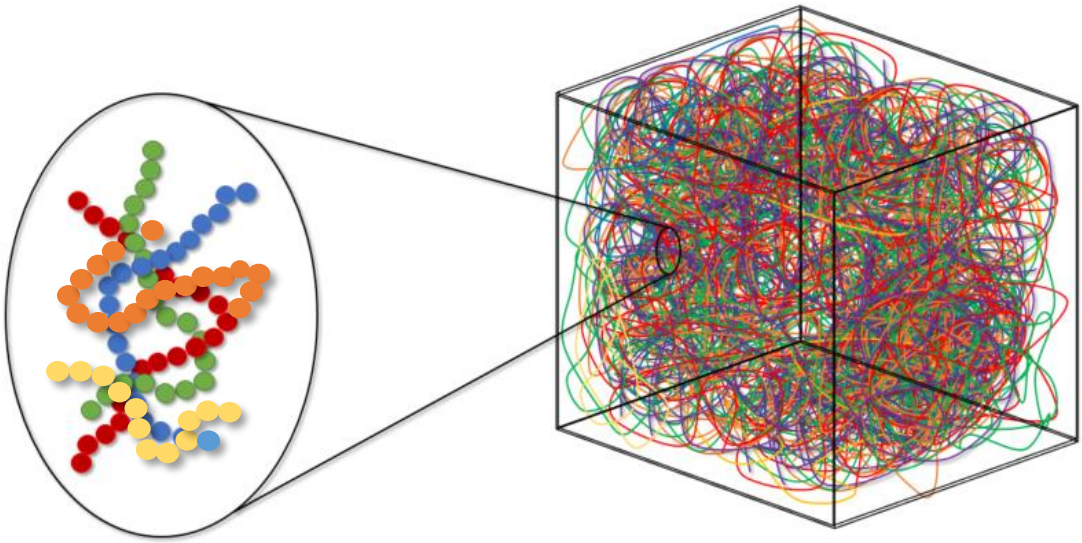

Figure 13: Graphical representation of the chemical chains which make up polymeric material

Polymers can include many engineering materials such as thermoplastics, adhesives and rubbers. Such materials demonstrate unique mechanical behaviours which makes them useful for specific engineering applications. In the case of photovoltaics, polymer materials such as EVA are used for encapsulation of the cells and interconnects. Polymers have a dynamic mechanical response which is dependent on temperature and time. For this reason, to appropriately model the strains generated during normal

operation of PV modules, it is important to consider the specific mechanical behaviour of polymer encapsulants.

Viscoelasticity

The ability of a material to return to its original form following deformation is known as elasticity. This property is a result of the stretching of polymer chains with an applied force. In engineering, the amount of elasticity of a material is determined by two parameters. They are the *modulus* and the *elastic limit*. The modulus is a measure of the amount of force per unit area required to produce a certain amount of deformation. The elastic limit is the maximum stress a material can withstand before permanent deformation occurs. In each case the standard unit is Pascal (Pa).

Viscosity is the measure of a materials resistance to deformation by shear or tensile stress. Whilst it is more often attributed to fluid materials, viscosity is also a property of solid materials. For example, glass can be considered a liquid with a very high viscosity.

When subjected to a sinusoidal stress load, a purely elastic material will demonstrate an immediate strain response, as shown in Figure 14, where as a purely viscous material will have a delayed response with a phase shift, δ, of 90° as shown in Figure 15. Viscoelastic materials will also demonstrate a delayed response where δ is somewhere between 0 and 90°, as in Figure 16.

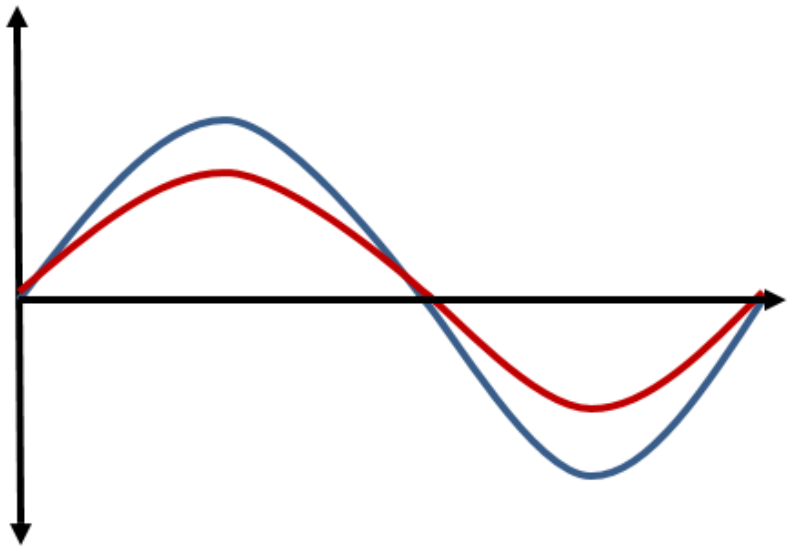

Figure 14: Graphical representation of a purely elastic material subjected to an oscillatory stress (blue line) demonstrating an immediate strain response (red line)

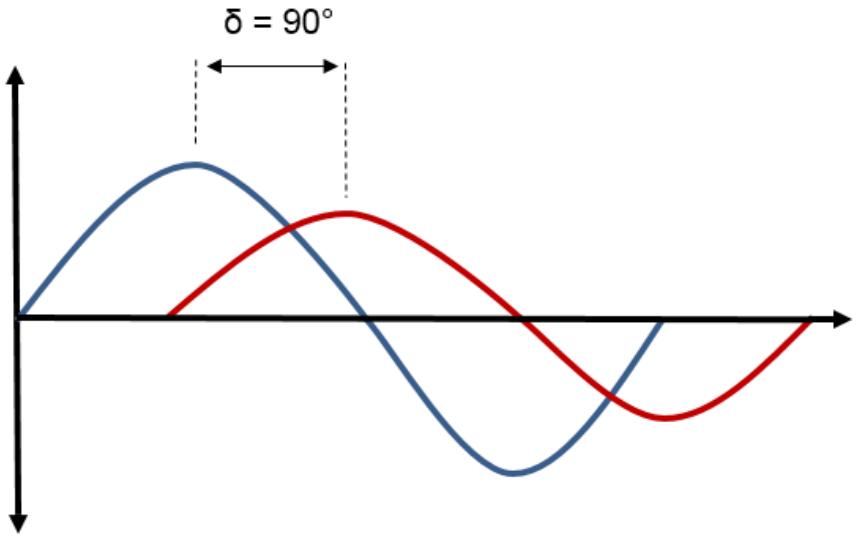

Figure 15: Graphical representation of a purely viscous material subjected to an oscillatory stress (blue line), a delayed strain response (red line) with a phase shift (δ) occurs as a result of the materials resistance to deformation

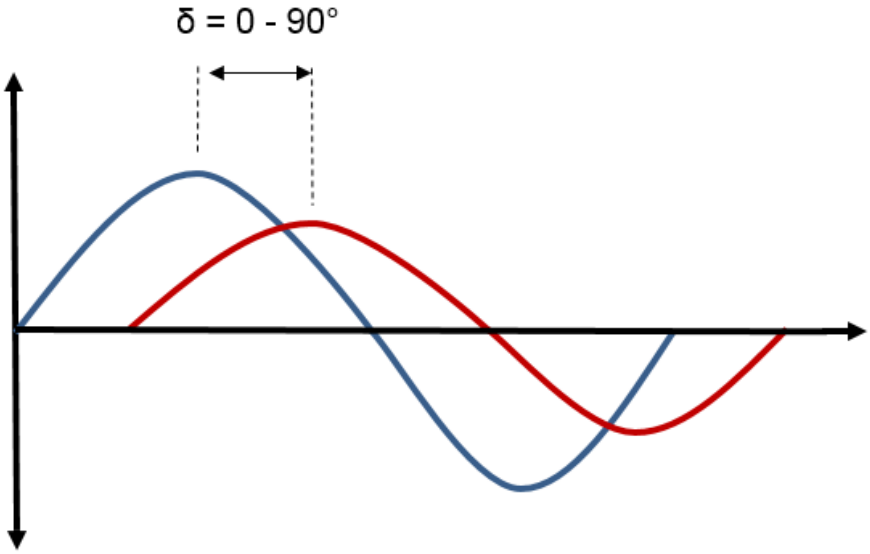

Figure 16: Graphical representation of a viscoelastic material subject to an oscillatory stress (blue line), the strain response (red line) is delayed with a phase lag in the region of 0 to 90°

Many materials may react like elastic solids when subjected to a sudden stress, but flow like liquids under smaller stresses. These materials can be said to possess both elastic and viscous properties, known as *viscoelasticity*. When a viscoelastic material is subject to an external load, a loss of energy occurs. As such, hysteresis can be observed in the stress-strain curve as shown in Figure 17.

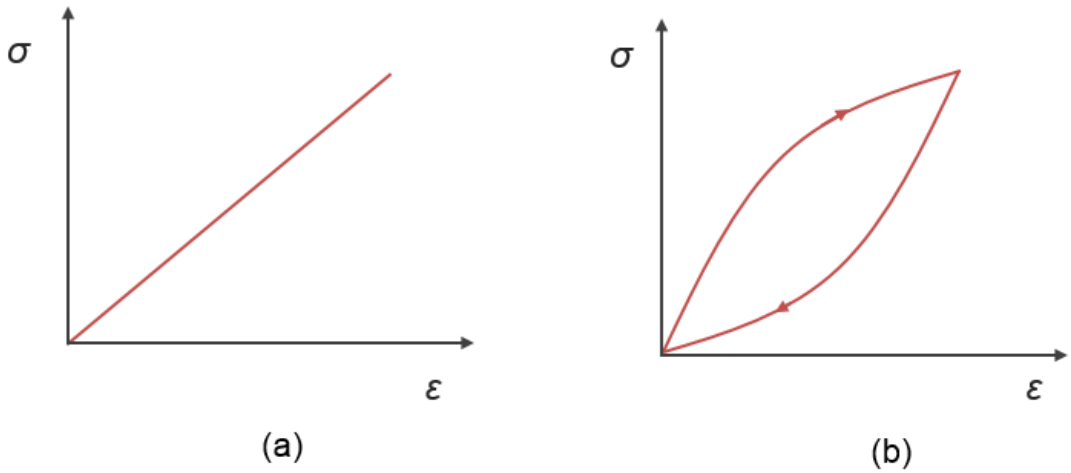

Figure 17: Stress-strain curves for (a) purely elastic material and (b) a viscoelastic material

Modelling Viscoelastic Behaviour

The viscoelastic properties of a material are typically studied using dynamic mechanical analysis (DMA). The basic principle involves the application of a small oscillatory stress (1) and measuring the resulting strain (2). For purely elastic materials, the strain response is immediate, whereas in purely viscous materials, a phase lag of 90° occurs. Viscoelastic materials, which possess both elastic and viscous portions, fall somewhere in between these two extremes.

$$\sigma = \sigma_0 \sin(\omega t + \delta) \quad (1)$$

$$\varepsilon = \varepsilon_O \sin(\omega t) \quad (2)$$

Where $\omega = 2\pi f$, with f being the frequency of the stress oscillation, t is time and δ is the phase lag between stress and strain.

The relationship between the oscillating stress and strain can be expressed as the complex dynamic modulus (3).

$$G = G' + iG'' \tag{3}$$

The storage modulus, G′, measures the stored energy which represents the elastic portion. The loss modulus, G′′, measures the energy dissipated as heat which represents the viscous portion. Each can be expressed as (4) and (5), respectively.

$$G' = \frac{\sigma_0}{\varepsilon_0}\cos\delta \tag{4}$$

$$G'' = \frac{\sigma_0}{\varepsilon_0}\sin\delta \tag{5}$$

The phase angle, δ, is given by (6).

$$tan\delta = \frac{G''}{G'} \tag{6}$$

Linear Viscoelastic Models

A purely elastic material can be represented as a linear elastic spring of stiffness E, as in Figure 18, the constitutive equation for which is given in (7).

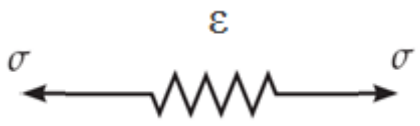

Figure 18: Graphical representation of a purely linear elastic material

$$\varepsilon = \frac{1}{E}\sigma \tag{7}$$

A purely viscous material can be represented as a linear viscous dash-pot, which is a piston-cylinder arrangement filled with a viscous fluid, as shown in Figure 19. A strain is achieved by dragging the piston through the fluid such that the dash-pot responds with a strain-rate proportional to stress (8), where η is the viscosity of the material.

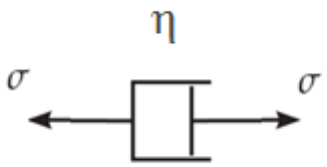

Figure 19: Graphical representation of a purely linear viscous material

$$\varepsilon = \frac{1}{\eta}\sigma \tag{8}$$

The linear viscoelastic model proposed by Maxwell, and shown in Figure 20, considers a spring and dash-pot connected in series such that both elastic and viscous parts are accounted for.

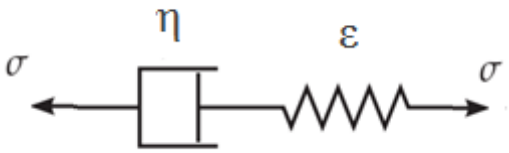

Figure 20: Simple linear viscoelastic model proposed by Maxwell

Maxwell's model is a simple model which might be suitable for a material exhibiting a single relaxation time. However, due to the multiple different lengths of polymer branch chains in a more complex material, a single spring-dashpot combination may not be sufficient to accurately model the materials relaxation behaviour. Long molecular branch chains take longer to relax than shorter ones. More complex models

can be constructed using multiple string-dashpot combinations, hereby referred to as Maxwell elements. The generalised Maxwell model (Figure 21) consists of N different Maxwell elements connected in parallel, where each element has its own parameter values. The number of elements required is dependent on the complexity of the material itself, and the accuracy required of the model.

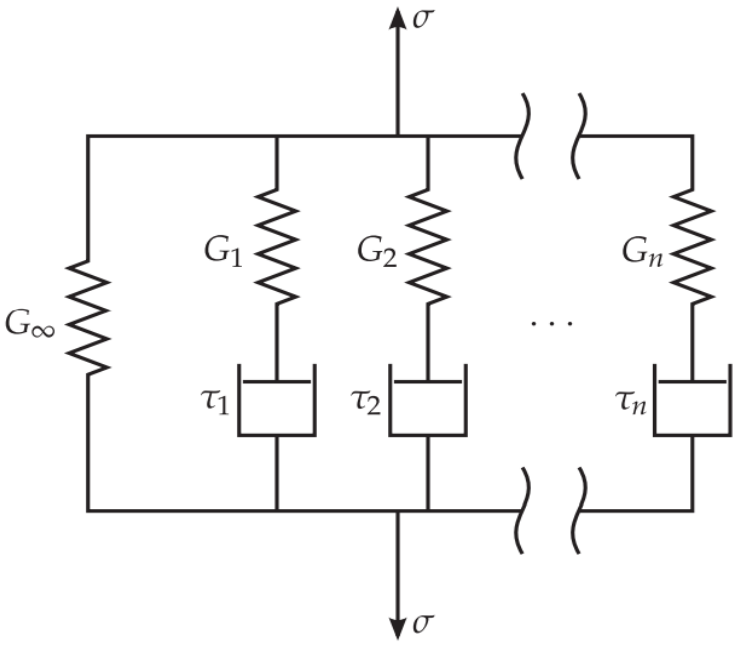

Figure 21: Generalised Maxwell Model for complex viscoelastic materials

For a model with N elements of elastic modulus G_n and viscosity τ_n, relaxation time can be given as (9) and the dynamic complex modulus of the material, as described by the generalised Maxwell model, can be written as (10).

$$\tau_k = \frac{\eta_k}{E_k} \tag{9}$$

$$G^*(\omega) = G_0 + \sum_{k=1}^{N} G_k \frac{i\omega\tau_k}{1+ i\omega\tau_k} \tag{10}$$

Where G_0 is the relaxed (or instantaneous) modulus, m is the number of Maxwell elements, G_k and τ_k are relaxation strength and relaxation time of the k^{th} Maxwell

element, respectively. The values necessary to model a material may be determined through DMA, which is explained further in the following subsection. These parameters are expressed as a Prony series and can be used as a direct input to for finite-element software packages to define the viscoelastic behaviour of a material.

4.4 Solder Deformation

As previously discussed in chapter 3, the degradation of solder bonds is of great concern in the PV industry. For an improved prediction of module lifetime and durability the question is how long will the solder bonds last and more recently, how long will they last under certain conditions.

Deformation Kinetics

Cyclic inelastic strains caused by large differences in CTE between the components of a module results in crack nucleation and growth, leading to damage and fatigue failure. Inelastic deformation is both time and temperature dependent and in order to fully appreciate the mechanisms of fatigue it is important to understand the deformation kinetics of the solder bonds. The properties of a solder bond are governed by its microstructure, which changes considerably during its lifetime. Homologous temperature is the temperature of a material expressed as a fraction of its melting point. Since solder alloys typically operate at high homologous temperatures, their deformation is dominated by mechanisms such as creep, coarsening and recrystallisation. Thermomechanical cycling at high homologous temperatures induces microstructural coarsening which is known to produce crack nucleation [68][69] particularly in the areas where coarsening is most severe. For this reason, it is important to take into account the microstructural evolution of the solder alloy when determining fatigue damage.

Anand's Viscoplastic Model

In this work, a unified viscoplastic constitutive law, known as Anand's model [70] has been implemented to calculate the inelastic deformation behaviour of the solder bonds within PV modules. The primary feature for this model is that a single scalar value is used to quantify the isotropic resistance to plastic flow, as defined by the structural characteristics of the material e.g. grain size, dislocation density etc. This value is denoted as *s* and is referred to as the deformation resistance. Naturally, the value of s evolves with temperature and time. The model consists of two coupled differential equations which relate the inelastic strain rate to the rate of deformation resistance. The strain rate equation for the Anand model can be written as (12), where the evolution of s is given by (13) and (14).

$$\dot{\varepsilon}_{\mathrm{p}} = Aexp\left(-\frac{Q}{RT}\right)\left[sinh\left(\zeta\frac{\sigma}{S}\right)\right]^{1/m} \tag{12}$$

Where $\dot{\varepsilon}_{\mathrm{p}}$ is the inelastic strain rate, A the pre-exponential factor, Q the activation energy, m the strain rate sensitivity, ζ the stress multiplier, R the gas constant and T the absolute temperature.

$$\dot{s} = \left\{h_0\left|1-\frac{s}{s^*}\right|^a . sinh\left(1-\frac{s}{s^*}\right)\right\}.\dot{\varepsilon}_p \quad ; \qquad \text{a>1} \tag{13}$$

$$s^* = \hat{s}\left[\frac{\dot{\varepsilon}_p}{A}exp\left(\frac{Q}{RT}\right)\right]^n \tag{14}$$

Where h_0 is the hardening constant, a the strain rate sensitivity of hardening, s^* the saturation value of *s*, $\hat{s}$ the coefficient and *n* the strain rate sensitivity for the saturation value of deformation resistance. The material parameters required for calculating viscoplastic deformation are *A*, *Q*, ζ, *m*, h_0, $\hat{s}$, *n*, *a* and s_0. Where s_0 is the initial deformation resistance value.

4.5 Thermal Modelling of PV Modules

An unwanted side effect from photovoltaic conversion is the generation of heat. Typical PV cells available on the market have a power conversion efficiency of approximately 15-20%. The remainder of the incident sunlight can be converted into heat. This unwanted thermal energy is detrimental to the module both in terms of electrical output [71] and health of the module.

Nominal Operating Cell Temperature

Knowledge of the expected operating temperature of a PV cell is required for determination of power output. Nominal operating cell temperature (NOCT), outlined by IEC61215 [1], is the temperature reached in a cell under a set of specific conditions outlined below:

- 800 W/m^2 irradiance on the cell surface
- 20°C ambient air temperature
- 1m/s wind velocity
- Open-rack mounting configuration

Heat Transfer Processes

Aside from the internal mechanisms accounting for heat generation, module temperatures are also affected by the external environment. Standard heat transfer processes such as conduction, convection and radiation must be taken into account. Conductive heat losses occur because of the thermal difference between the module and its surrounding environment. Such losses are dependent on the thermal properties of the materials used in the module.

Convective heat transfer occurs as a result of the transportation of heat away from the surface of the module, mostly as a result of wind blowing across the surface. The degree of heat lost is dependent on the surface area and temperature difference

between the transporting medium and module. The final mechanism is radiative heat to the surrounding environment. The amount of heat radiated depends on the emissivity and temperature of the module.

Thermal Modelling of PV Modules

The thermal behaviour of a module is dependent on a number of different factors including properties of the module, meteorological conditions, orientation and location. As such, operating temperatures of modules is not always a readily-available parameter and yet is an important factor for the design and sizing of systems. For this reason, a lot of work has been done on estimating module temperature using information which is more readily available i.e. meteorological data and module characteristics. An expansive array of models have been proposed [72]. The models can be categorised as either implicit or explicit. Implicit models consider the energy balance of the module and thus takes into account the heat transfer mechanisms described previously. This type of model requires that the module achieves a steady-state condition so that the instantaneous operating temperature can be determined. One such model is proposed by Mattei et al [73], which is based on a simple energy balance solution. The model (15) uses p+qW = U_{pv} as the heat exchange coefficient dependent on wind speed, where W is wind speed and p and q are empirical coefficients. Additionally, C_α is the cell absorption coefficient, τ is the glass transmittance, η_r is the module efficiency under benchmark conditions and γ is the absolute value of the variation coefficient of power with module temperature.

$$T_m = \frac{U_{PV}T_{amb}+G[(C_\alpha\tau)-\eta_r-\gamma\eta_r T_r]}{U_{PV}-\gamma\eta_r G} \quad (15)$$

Servant [74] also proposed a simplified model for heat exchange between the PV module and its environment (16). Where d, e and f are empirical parameters which may be fit to experimental data.

$$T_m = T_{amb} + dG(1 + eT_{amb})(1 - fW) \quad (16)$$

The limitation to such models is that a steady-state condition is difficult to achieve under normal operating conditions, which are constantly changing. Explicit models calculate operating temperatures using known parameters. The NOCT model determines a ratio between the nominal temperature and the temperature of the module as (17).

$$T_m = T_{amb} + \frac{G}{800}(NOCT - 20) \quad (17)$$

The NOCT model is quite often used to empirically determine NOCT using experimental measurements of module temperature and the other input parameters, T_{amb} and G [75]. However, its shortcomings are that it is defined under very specific conditions which, especially for some climates, are impossible to meet. A modification of NOCT is proposed by Koehl et al [76] called the Realistic Operational Module Temperature (ROMT). ROMT is more representative of operating temperatures in outdoor conditions and takes the form shown in (18) where U_0 and U_1 are empirical parameters derived by Faiman [77], which describe the effects of irradiance and wind, respectively.

$$ROMT = \frac{820}{U_0 + U_1} \quad (18)$$

The Ross model [78] shown in (19) is one of the more simplistic models which proposes that the difference between module temperature and ambient temperature is directly proportional to irradiance. A single coefficient, k, known as the Ross coefficient, is used to describe the influence of module technology, material properties, assembly and environmental conditions.

$$T_m = T_{amb} + kG \quad (19)$$

Where T_m is module temperature, T_{amb} is ambient temperature and G is incident irradiance. One of the major shortcomings of the Ross model is its inability to account for wind speed. King et al [79] remedied this by proposing a ratio between the module temperature, wind speed and incident irradiance as in (20).

$$T_m = T_{amb} + Ge^{(m+nW)} \tag{20}$$

Where m is an empirical coefficient describing the impact of irradiance which establishes an upper limit for module temperature neglecting wind speed and n is an empirical coefficient describing the cooling effects of wind speed.

Chapter 5

Evaluation of Climate-Specific Thermal Stresses

5.1 Introduction

A better understanding of the climate-specific thermomechanical stresses experienced by modules in outdoor environments first requires that the causes for such stresses are examined. The operating temperatures of modules are the driving force behind the thermomechanical stresses and to assume that they are the same between different climate types would be a huge oversight. Different climates exhibit different temperature highs, different rates of temperature change and different temperature fluctuation frequencies. This chapter contains a comprehensive evaluation of module temperatures in nine locations across five different climate types. The relevant thermal profile characteristics are discussed and compared between each climate type in terms of their potential impact on modules.

5.2 Estimating Module Temperatures

In order to obtain a level comparison of thermal exposure, it is necessary to have measured data from modules of the same design and materials, installed in the same configuration across the different locations. Such data is unavailable and so a modelling approach is employed.

Fuentes Model

The model described by Fuentes et al [80] considers the absorptivity, emissivity and thermal capacitance of PV modules to appropriately characterise transient behaviour. This is an important consideration when dealing with high resolution data and for evaluating thermal ramping rates. The model is derived from an energy balance solution. If a PV module is modelled as a single uniform material (Figure 22) then module temperature, Tc, is a function of the incident irradiance, S, the convective heat losses to ambient temperature, Ta, and radiative losses to the sky and ground, Ts and Tg, respectively. Such that the balance can be given as (21).

$$hc\,.\,(T_c - T_a) + \varepsilon.\sigma.\,(T_c^4 - T_s^4) + \varepsilon.\sigma.\left(T_c^4 - T_g^4\right) - \alpha.S + m.c.\frac{dTc}{dt} = 0 \qquad (21)$$

Where hc is the overall convective coefficient, α and ε the emissivity and absorptivity of the module, respectively, m is the mass of the module, σ is Boltzmanns' constant and c the overall specific heat capacity.

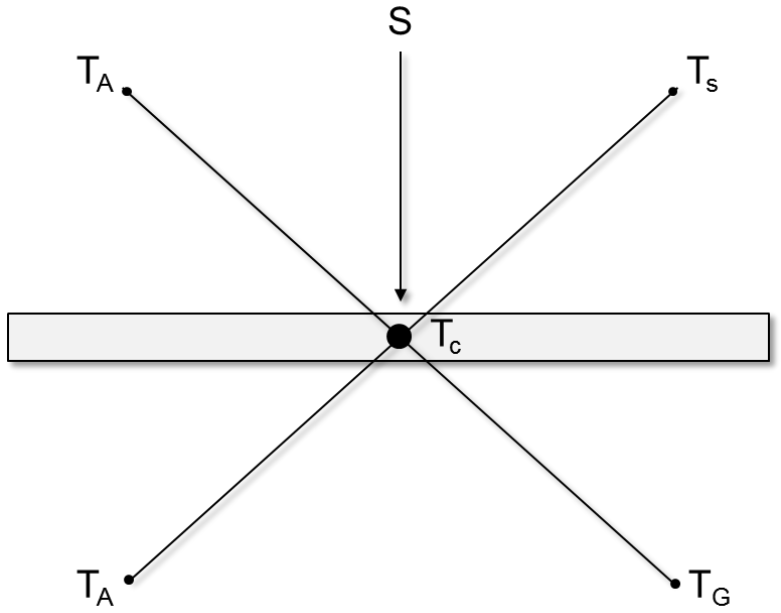

Figure 22: Simplified graphical representation of the thermal model as an energy balance solution

Equation (21) can be linearised through expansion of the radiation terms. The heat balance equation can then be simplified by defining a radiation coefficient, hr as (22) and (23).

$$hr_s = \varepsilon.\sigma.(T_c^2 + T_s^2).(T_c + T_s) \tag{22}$$

$$hr_g = \varepsilon.\sigma.\left(T_c^2 + T_g^2\right).(T_c + T_g) \tag{23}$$

Irradiance is modelled as a continuous function (24), rather than a step function, which is more realistic and further reduces potential errors in the T_c calculation.

$$S = S_0 + \Delta S\,.\frac{t}{\Delta t} \tag{24}$$

The energy balance equation can then be written as (25).

$$hc\,.(T_c - T_a) + hr_s\,.(T_c - T_s) + hr_g\,.\left(T_c + T_g\right) - \alpha\,.\left(S_o.\Delta S.\frac{t}{\Delta t}\right) + m.c.\frac{dTc}{dt} = 0 \tag{25}$$

Integrating (6) gives an explicit expression for module temperature (26).

$$T_c = \frac{hc\,.T_a + hr_s.T_s + hr_g.\left(T_g + \alpha\,.S_o + \alpha\,.\frac{\Delta S}{L}\right).(1 - e^L) + \alpha\,.\Delta S}{hc + hr_s + hr_g} + T_{c0}\,.e^L \tag{26}$$

T_{c0} is the module temperature at the start of the time step and is equivalent to T_c from the previous time step. 1/L is the thermal capacitance of the module where L is defined as (27).

$$L = \left(hc + hr_s + hr_g\right).\frac{\Delta t}{(m.c)} \tag{27}$$

Values for each parameter in (26) are either given or can be determined from input data. Radiative coefficients to the sky and ground (or roof), hr_s and hr_g, can be determined from sky temperature, T_s. Sky temperature is dependent on many factors including ambient temperature, humidity, cloud cover and elevation. This model builds on an approach from Swinbank [81] that averages out the effects of humidity

and elevation, however, Swinbanks approach is not suitable to cloudy days. On wholly cloudy days, sky temperature approaches ambient temperature, and so it is assumed that average sky temperature would be somewhere between ambient and Swinbacks estimation. Therefore, Swinbanks original equation is modified to adjust for the average clearness index of any given day.

The overall convective coefficient, hc, is the sum of both top and bottom convective coefficients. While the top convective coefficient, hc_t, is relatively simple to determine, the convective coefficient for the rear surface, hc_g, must be approximated from hc_t and installed nominal operating cell temperature (INOCT). INOCT is an alteration of the standard NOCT conditions (described in chapter 4), which approximates the effect of the mounting configuration on rear surface heat loss. The method for determining INOCT from NOCT conditions outlined by Fuentes is presented in Table I.

Table I: Determination of INOCT from NOCT and mounting configuration

Mounting Configuration	INOCT (°C)		
Rack Mount	NOCT – 3		
Direct Mount	NOCT + 18		
Standoff/Integral	NOCT + X	W (inches)	X
		1	11
		3	2
		6	-1
		Where W is standoff height	

Absorptivity, α, and emissivity, ε, of the module are both important when considering the thermal energy balance. In this model, absorptivity is defined as the fraction of in-plane irradiance converted into thermal energy and can be represented as (28), where r is reflectivity and η is module efficiency.

$$\boldsymbol{\alpha = (1 - r) \,.\, (1 - \eta)} \tag{28}$$

The thermal mass of the module is also required to simulate thermal lag and transient effects. In Fuentes' publication, the average thermal mass, emissivity and reflectivity for modules from 4 manufacturers was given as 11 KJ/m^2, 0.84 and 0.1, respectively. In this work, these properties are determined for modules which are available on-site.

Plane-of-Array Irradiance Translation

Irradiance data from the BSRN comes in the form of direct normal and diffuse in the horizontal plane. Therefore, a translation of this data is necessary to obtain the total irradiance incident on the surface of the modules. The method outlined by Liu and Jordan (Eq. (29)-(32)) is employed [82] .The method is simple, but is used here since it does not rely on location-specific, empirically-determined parameters which may influence comparison of the thermal effects under investigation.

$$G_k = G_{b,k} + G_{d,k} + G_{a,k} \tag{29}$$

$$G_{b,k} = (G_{b,h} \times Cos(\theta_z)) \times (\frac{Cos(\theta)}{Sin(h)}) \tag{30}$$

$$G_{d,k} = (0.5 \times G_{d,h}) \times (1 + Cos(\alpha)) \tag{31}$$

$$G_{a,k} = 0.5 \times \left(G_{d,h} \times \rho\right) \times (1 - Cos(\alpha)) \tag{32}$$

Where G_k, $G_{b,k}$, $G_{d,k}$, $G_{a,k}$ are the total, beam, diffuse and ground-reflected irradiance in the plane-of-array, respectively. $G_{b,h}$ is the direct irradiance in the horizontal plane, θ_z is the solar zenith angle, θ is the angle of incidence, $G_{d,h}$ is the diffuse irradiance in the horizontal plane, h is the solar elevation angle, α is the array tilt angle. ϱ is the ground reflectance and is assumed to be 20%. For each location, the year-round optimum array tilt is determined as a function of latitude.

Thermal Model Optimisation

In order to gain a level of confidence in the results, the model is optimised for open-rack mounted modules with a glass/EVA/c-Si/EVA/Tedlar© structure which are

installed on-site at Loughborough University. The module-specific parameters, emissivity, absorptivity and thermal mass are unknown for these modules and are determined through fitting. Using 1-minute resolution meteorological data also collected on-site, module temperatures are estimated and compared with measured module temperatures. The Nelder-Mead (or Downhill Simplex) method [83] is used to fit the model to direct measurements from the rear-side of the installed modules, such that the thermal characteristic property values can be extracted. The advantage of using this particular fitting method is that limits can be applied to the fitted coefficients, so that the best fit that lies within realistic values can be determined. Fitting the model to one year of data (Figure 23) produced a root-mean squared deviation of 2.19°C.

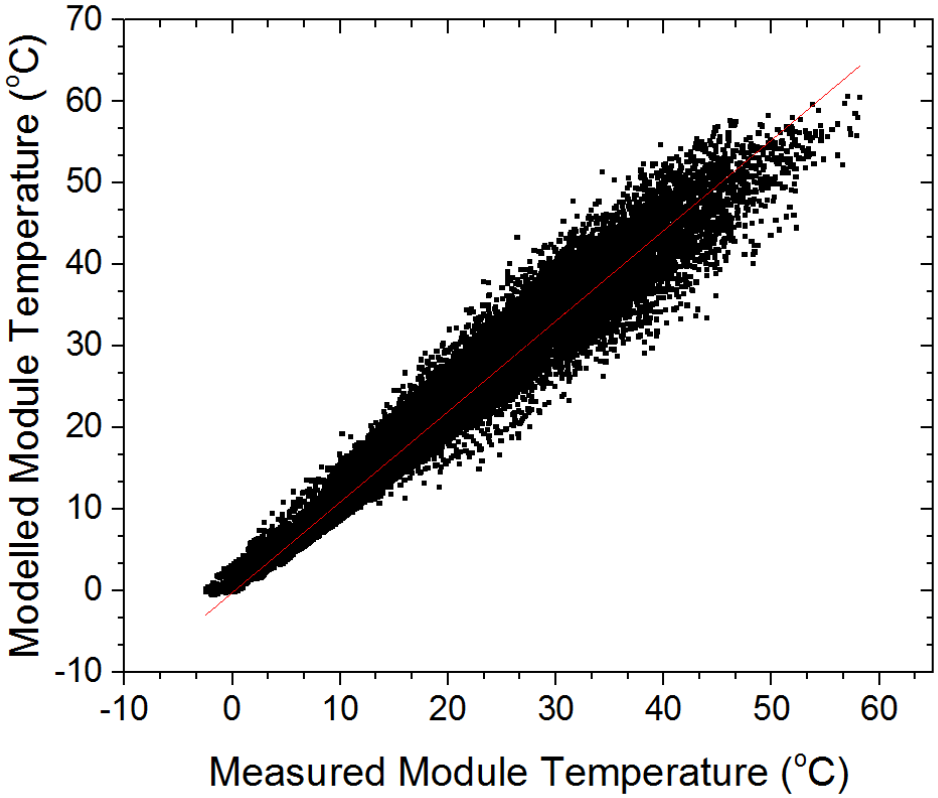

Figure 23: Comparison of one year of measured and modelled module operating temperatures in Loughborough, UK.

5.3 Weather Data

Weather data is obtained from the Baseline Surface Radiation Network (BSRN). The BSRN is a project under the World Climate Research Programme (WCRP), a collaborative effort which archives radiation measurements along with surface and upper-air meteorological observations in 58 locations across various climate zones [84]. Measurements are obtained with high time resolutions (1 to 3 minutes) using instruments of the highest available quality.

Site Selection

Nine sites are selected from the network for this study. Down-time for maintenance or equipment faults is unavoidable and as such some gaps in the data are present. Site selection was primarily determined by the availability of data. It was found that 2011 had the greatest availability for most sites, with a completeness of >98%. Each site was grouped into their respective climate classification and the sites with the fewest gaps in data were selected. Climate classification is based on the system presented by the All-Indian Survey [85]. Whilst other classification systems are available, the one outlined by the All-India Survey was specifically used for a study on PV systems in India. Table II and III, outline the classification for each climate group and the location and category for each site being studied, respectively.

Table II: Climate zone classification as per All-India Survey with the addition of a warm & humid climate

Climate Type	Mean Monthly Temperature High (°C)	Mean Monthly Relative Humidity (%)
Hot & Humid	>30	>55
Hot & Dry	>30	<55
Warm & Humid	25 – 30	>75
Temperate	25 – 30	<75
Cold	<25	All Values

Table III: Outline of the sites selected for study

Station	Short Name	Climate	Latitude	Array Tilt (°)
Darwin, Australia	DAR	Hot & Humid	-12.425	10.8
Momote, Papua New Guinea	MAN	Hot & Humid	-2.058	1.79
Gobabeb, Namibia	GOB	Hot & Dry	-23.5614	20.5
Solar Village, Saudi Arabia	SOV	Hot & Dry	24.29	21.13
Cabauw, Netherlands	CAB	Warm & Humid	51.971	42.57
CENER, Spain	CNR	Warm & Humid	42.816	35.64
Southern Great Plains, OK, USA	E13	Temperate	36.605	30.92
Carpentras, France	CAR	Temperate	44.038	36.57
Regina, Canada	REG	Cold	50.205	41.26

Figure 24: Locations and climate group of each station

5.4 Evaluation of Thermal Effects

For each location outlined in Table III, one-year of module operating temperature data is synthesised. Figure 25 presents a box plot of module temperatures observed for the year for each location. The maximum and minimum seen across all sites is 81.3°C and -33.6°C, respectively. This includes night time hours, which brings down the average temperatures. For other mounting and packaging configurations, maximum temperatures can increase by as much as 20K [86]. The highest average temperatures are observed in the Hot and Humid climates, where minimum temperatures are also highest amongst the sites. Hot and Dry climates demonstrate the highest maximum temperatures. Lowest temperatures are observed, as expected, in the cold climate with a minimum temperature extreme of -33°C.

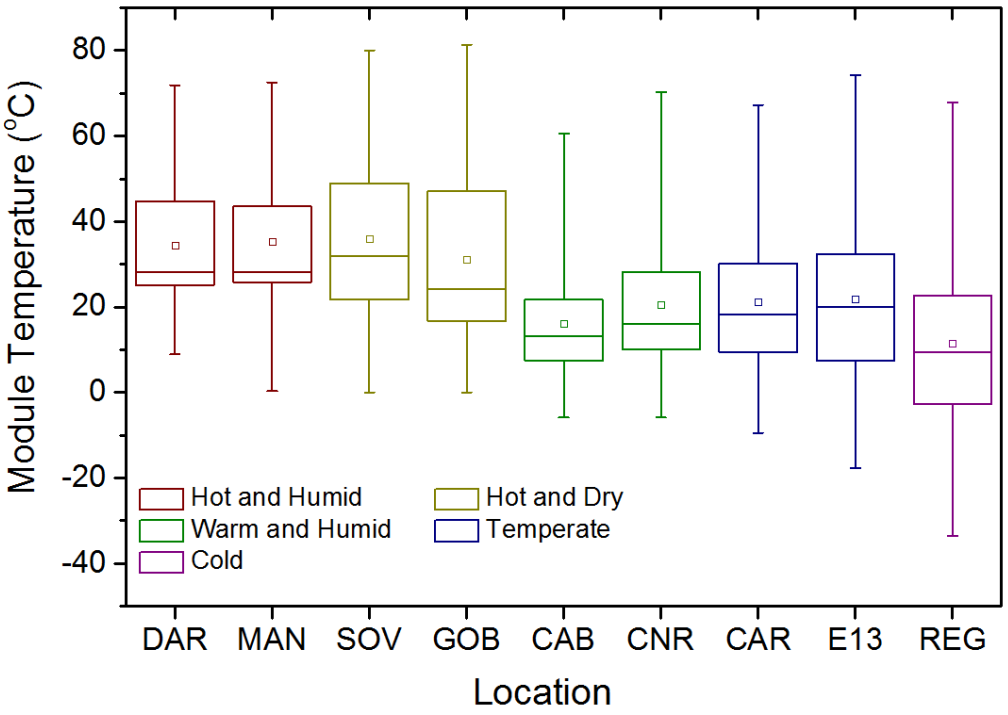

Figure 25: Box plot for 1 year of operating temperatures in each location. Whiskers represent maximum and minimum observed temperatures, □ represents mean temperature

Whilst temperature highs and lows have been presented, it is useful to look at the total exposure time at different temperatures for each site. High operating temperatures of greater than 70°C are often reported as being highly detrimental to PV modules. While such temperatures occur in most of the locations studied, it can be seen in Figure 26 that they are relatively infrequent. Similarly, temperatures of -20°C and below are rare. The glass transition temperature of EVA is an important consideration. When this transition occurs, typically around -30°C, EVA becomes much more brittle and loses much of its protective qualities. The IEC61215 TC200 test, outlined previously in chapter 2, repeatedly exposes modules to temperatures below the glass transition region. However, it can be seen from Figure 26 that such temperatures are rarely, if ever experienced by modules in real environments. This raises the question of the relevance of exposing modules to such conditions for certification testing and what effects could be being introduced unnecessarily.

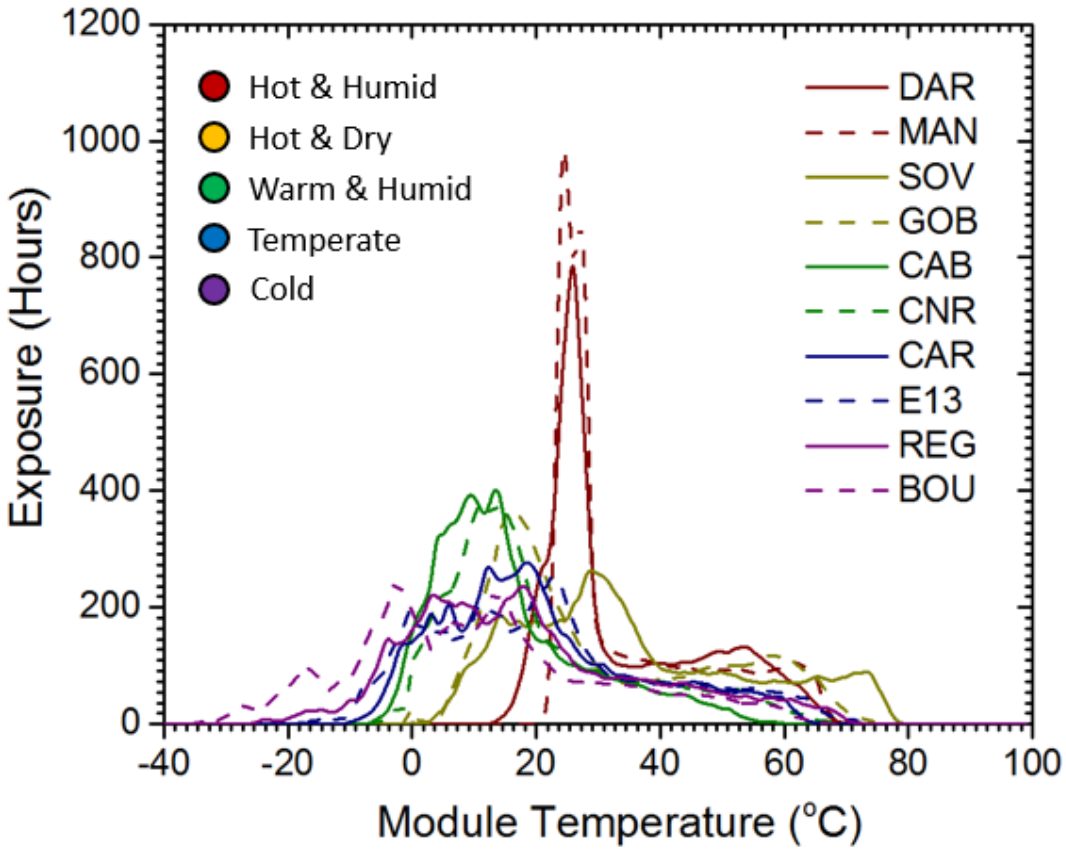

Figure 26: Total exposure time for module operating temperatures in each location

Temperature Travelled

Total temperature travelled is defined as the sum of the absolute changes in temperature at each time step. It is often used to normalise and compare climates in terms of thermal exposure. Figure 27 shows the total temperature travelled for each location for one year of data. The hot and humid climates, DAR and MAN, experience the highest total temperature travelled. This is likely due to the combination of high temperatures and the increased frequency of temperature fluctuation which might be expected of a tropical environment where intermittent cloud cover (and incident irradiance) is common. The locations with the lowest total temperature travelled are the hot and dry climates, SOV and GOB, despite having higher average temperatures. In this case, it would be expected that fewer temperature fluctuations occur since dry

climates experience more clear skies. While technically falling under the temperate climate specification, CAR sees much less total temperature travelled. In order to better understand the differences in total temperature travelled, an analysis is conducted on the frequency of temperature fluctuations in each location.

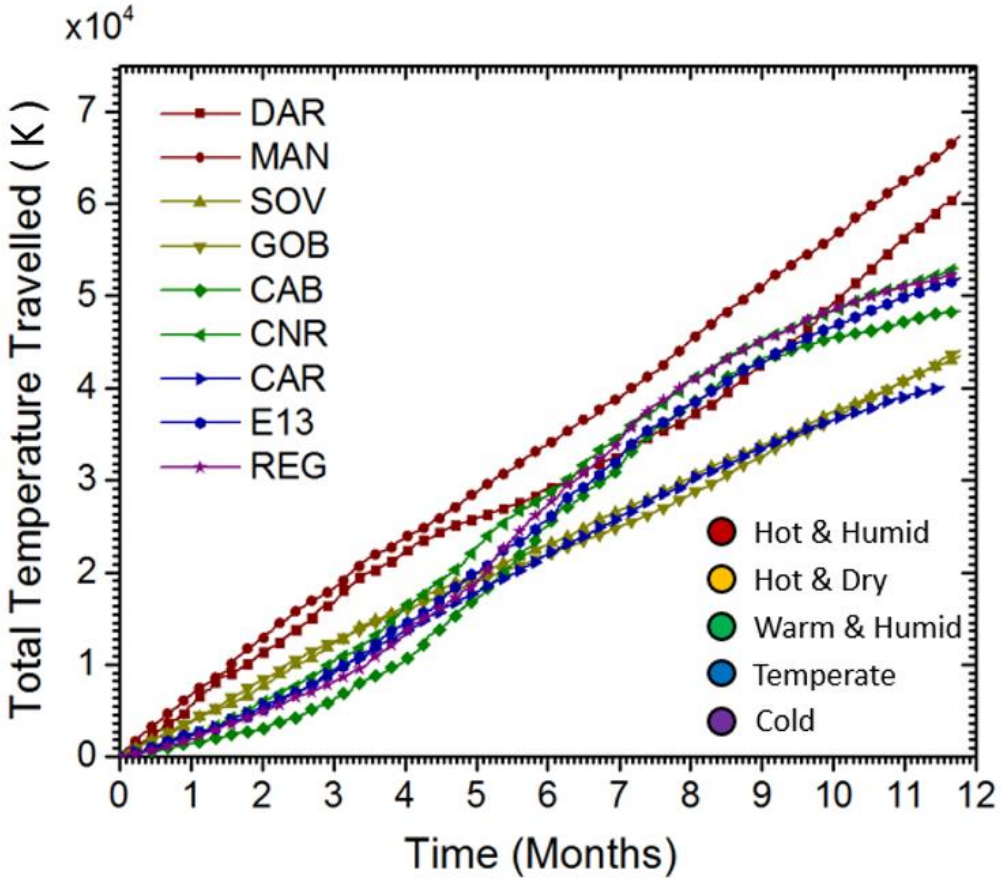

Figure 27: Total Temperature travelled for one year at each location

Temperature Ramping Events

PV module damage potential on days with intermittent cloud cover can be significantly higher than on clear-sky days and is largely determined by the number of temperature fluctuations, a result of moving clouds and subsequent changes in irradiance exposure [87][88]. Intra-day temperature fluctuations are largely dominated by cloud movement and the subsequent variation in irradiance. Given the random nature of intermittent cloud cover, the module temperature time-series at

high-resolutions can become quite noisey. A simplification of the time-series is conducted in order to appropriately quantify the fluctuations. The simplification reduces the time-series into distinct occurrences of rising and falling temperatures, hereby known as "ramping events". In order to realise this simplification, a method based on the Rainflow-counting algorithm is employed. The algorithm is a tool commonly used to analyse complex stress-loading spectra [89] and works by identifying moving-trends in a time-series. In this work, a new ramping event is identified when a reversal is detected, that is, when a change in temperature of more than 1°C in the opposite direction of the existing ramp is detected. A graphical representation of the rainflow-counting algorithm is show in Figure 28.

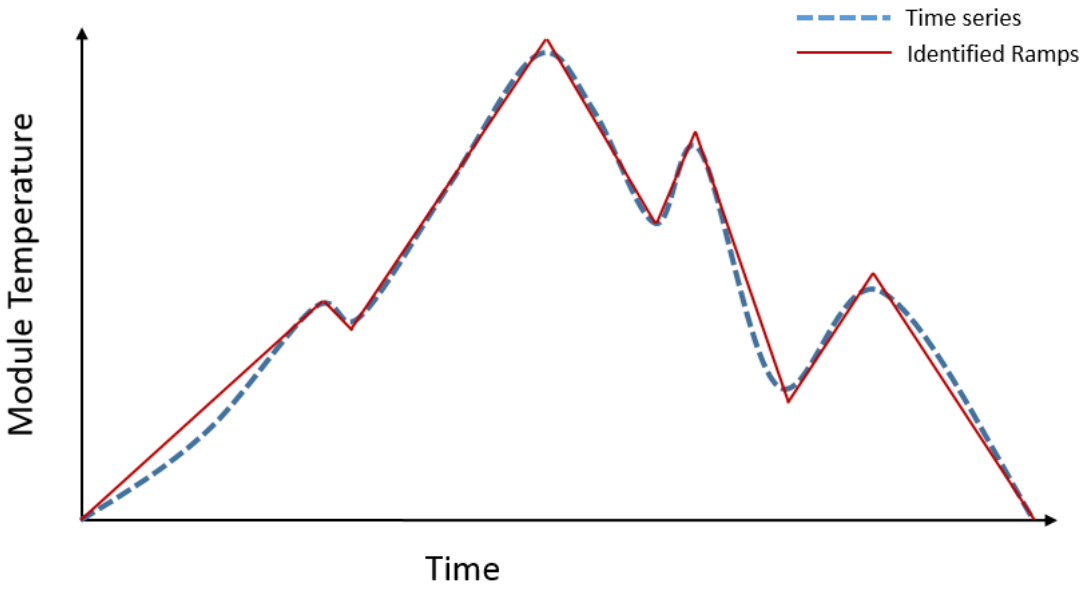

Figure 28: Graphical representation of the identification of ramping events for a module temperature time series using rain-flow counting

Ramping Event Range

The ramping event range is the magnitude of the total change in temperature during the course of a ramping event. Observations in the size of ramping events provides an insight into the types of changes in temperature being experienced by modules in different climatic regions. A prevalence of shorter ranges (< 20K) will be indicative of modules experiencing more frequent short-term fluctuations in temperature. Conversely, if larger ranges are dominant, this would be an indication that the modules are not subject to intermittent cloud cover, and that the diurnal temperature cycle is most prevalent with some infrequent cloud cover. The mean daily maximum ramp event range per station is presented in Figure 29. As would be expected, the Hot and Dry climates demonstrate the highest mean since these climates would experience more consistent clear days which, when combined with high ambient temperatures, facilitates large changes in temperature during sunrise and sunset.

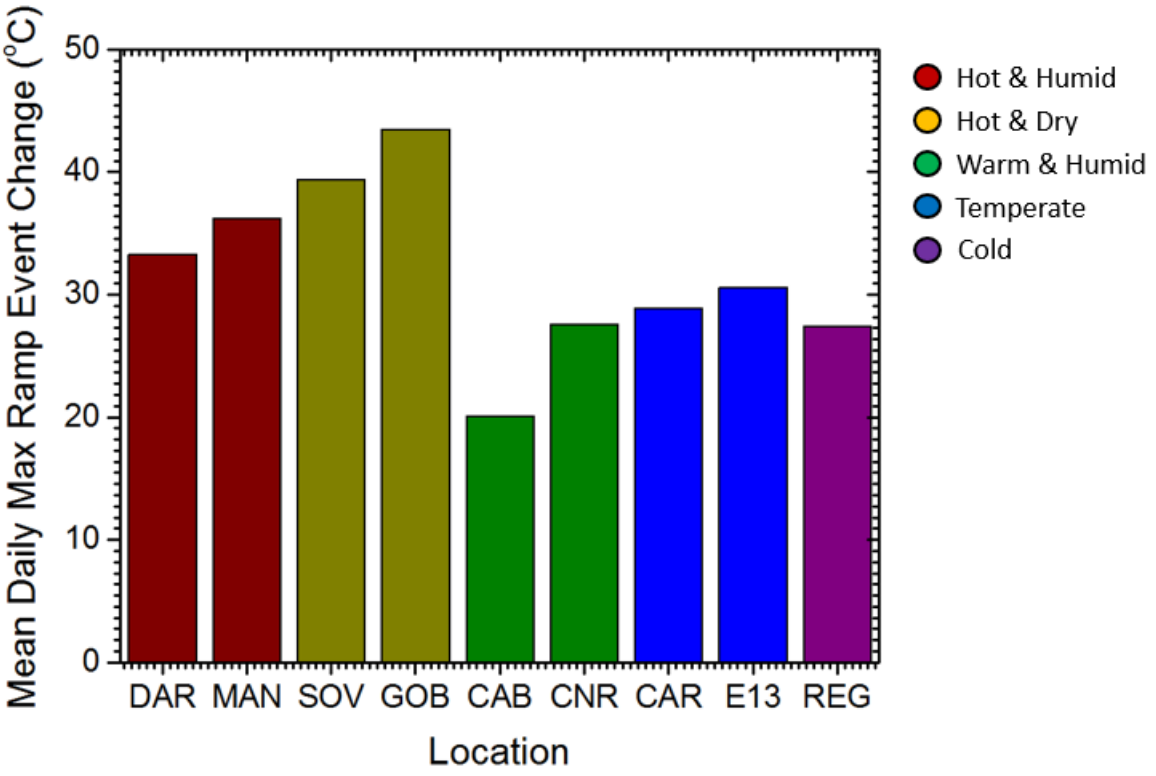

Figure 29: Mean daily maximum ramping event range for each site over one year

Figure 30 presents the cumulative distribution of ramping events in terms of ramping event range for each location. It is shown that the hot and humid climates have the highest number of temperature ramping events for one year, followed by warm and humid, and temperate. The hot and dry climates exhibit the fewest ramping events. For the climates with highest cumulative count, ramp magnitudes of 20K or less make up approximately 90% of all events. This is indicative of the smaller, intra-day fluctuations in temperature which arise as a result of cloud movement and partial shading. By contrast, it can be seen that the hot & dry climates experience a more even distribution, with 70% of ramping events at lower temperatures. The longer ramping events seen in these locations could be explained by the undisrupted ramps during sunrise and sunset. Clearer sky conditions means there are fewer disruptions in the large ramping periods. Whilst the other locations all experience sunrise and sunset

ramping events, they are less significant due to fewer clear sky conditions and lower ambient temperatures.

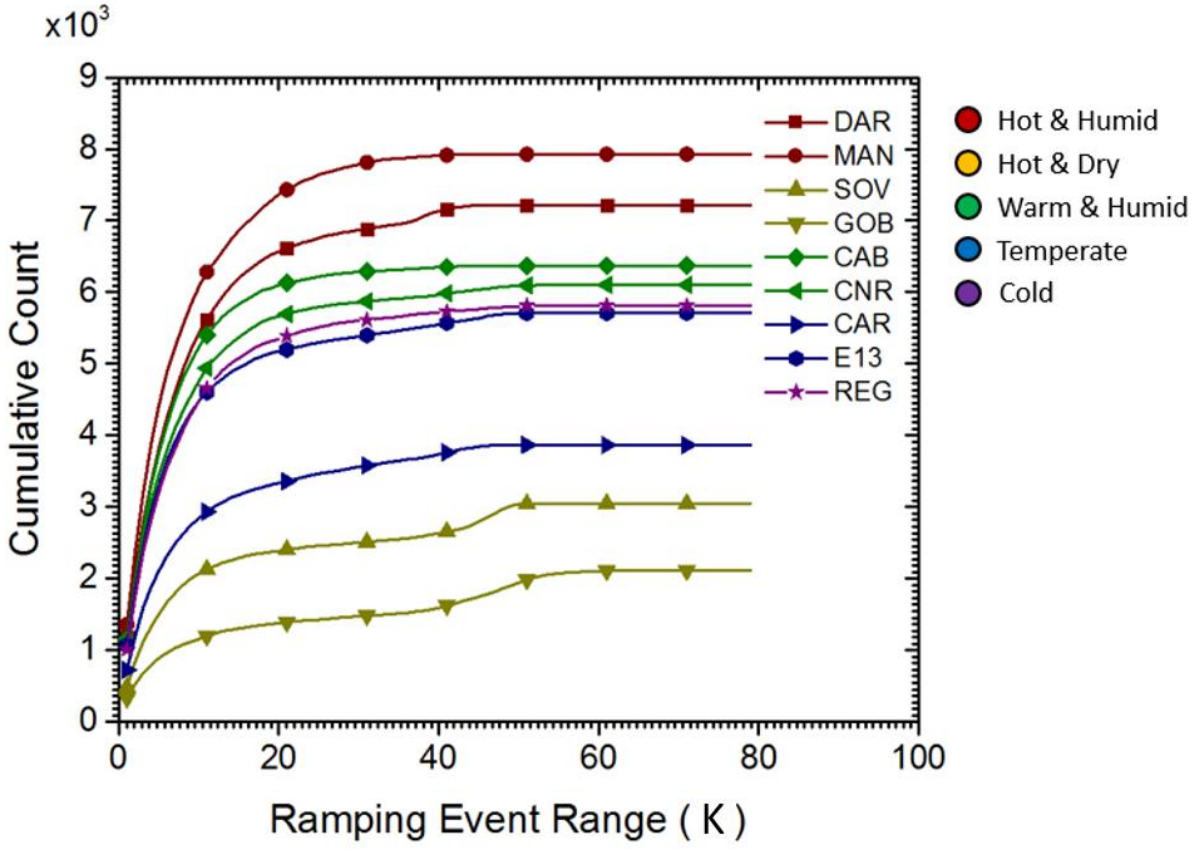

Figure 30: Cumulative count of ramping event range per site

Figure 31 presents an absolute distribution of ramping events per ramp event range, where the inset focuses on ramping event ranges greater than 30K. The hot and dry climates are shown to have a higher proportion of long range ramping events than the other locations, which reflects the sudden increase in cumulative count shown in Figure 30. In the case of DAR (Hot & Humid), there is a distinct dry period in the year during which there are more clear sky days. As a result, sunrise and sunset ramping events see less disruption by cloud cover accounting for the observed peak at 30-40°C.

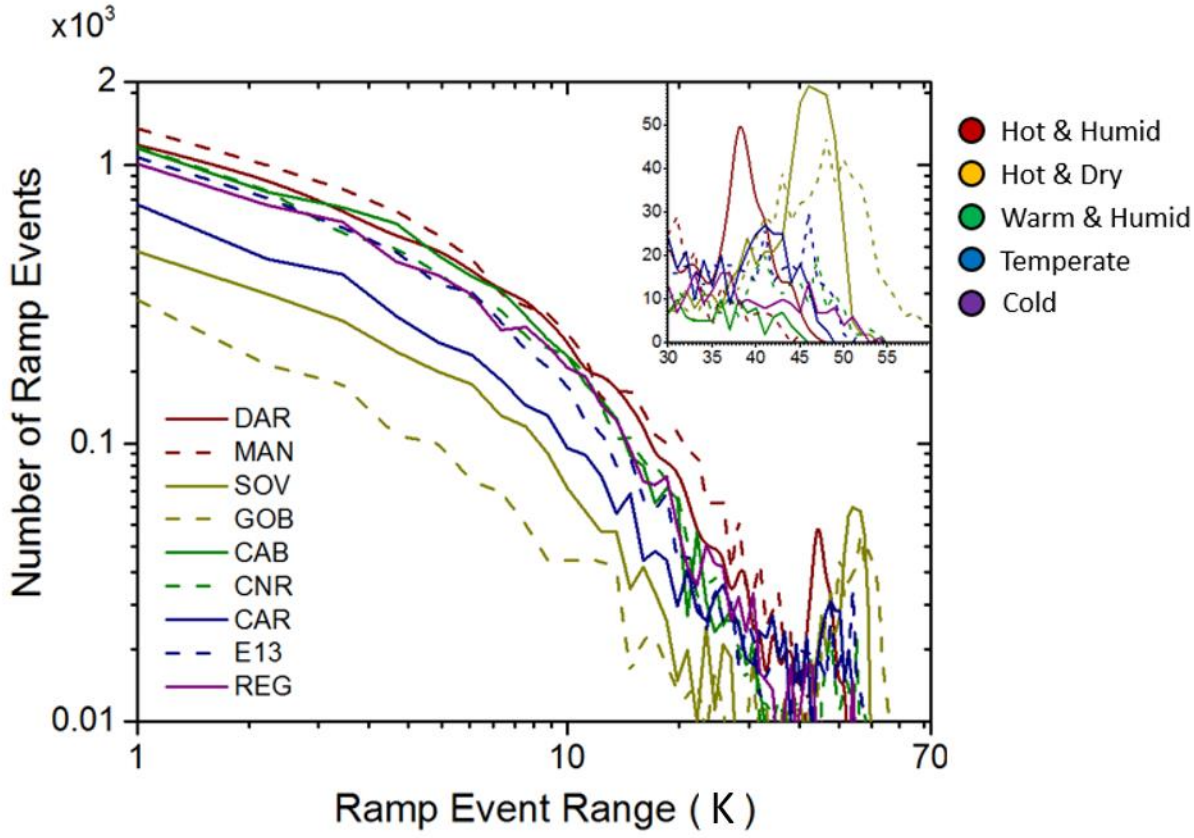

Figure 31: Distribution of ramping event sizes for each site

Absolute Temperatures

The total exposure at each temperature has been discussed in the previous section, however this does not reveal the whole story. It is important to consider at what temperatures the majority of ramping events are occurring. Many thermal effects dictating the amount of stress generated within a module are dependent on absolute temperatures. For example, EVA exhibits a temperature-dependent storage modulus: at higher temperatures EVA becomes softer, which eases some of the compressive stresses being applied to cells so that temperature changes occurring in this range may contribute differently to thermal fatigue than at lower temperatures. Another example is creep-strain effects for solder bonds which become more severe at elevated temperatures. Figure 32 demonstrates the frequency of occurrence of ramping events

in terms of their start and end point temperatures, such that the absolute temperatures in which ramping events are occurring can be observed. Hot and Humid sites (Figure 32(a) and (b)) exhibit a narrow range of absolute temperatures, with two distinguishable regions. The first, significant proportion of the ramping events occur at higher temperatures of 50 to 70°C. These ramps can be attributed to mid-day temperatures. Additionally, there are many ramping events in the range of 20-30°C which are likely due to minor ramping events occurring at night. For the Hot and Dry climates (Figure 32 (c) and (d)) a more distributed range of absolute temperatures is observed. Sunrise and sunset ramps are more clearly demonstrated here as the events starting at lower temperatures and ending higher, and vice versa. These ramping events are more distinguishable since the clearer skies and higher ambient temperatures result in more pronounced morning and evening ramps. The other climates (Figure 32 (e-j)) show more ramping events occurring within and below the crystal melt phase of EVA (<30°C). Such ramping events could result in more dramatic cell displacement, thus increasing the strain-load on solder bonds and, subsequently, long-term fatiguing potential. In all cases heating and cooling ramps are shown to be not entirely symmetric, this is due to the properties of the modules being modelled, which cool down slower than they heat up.

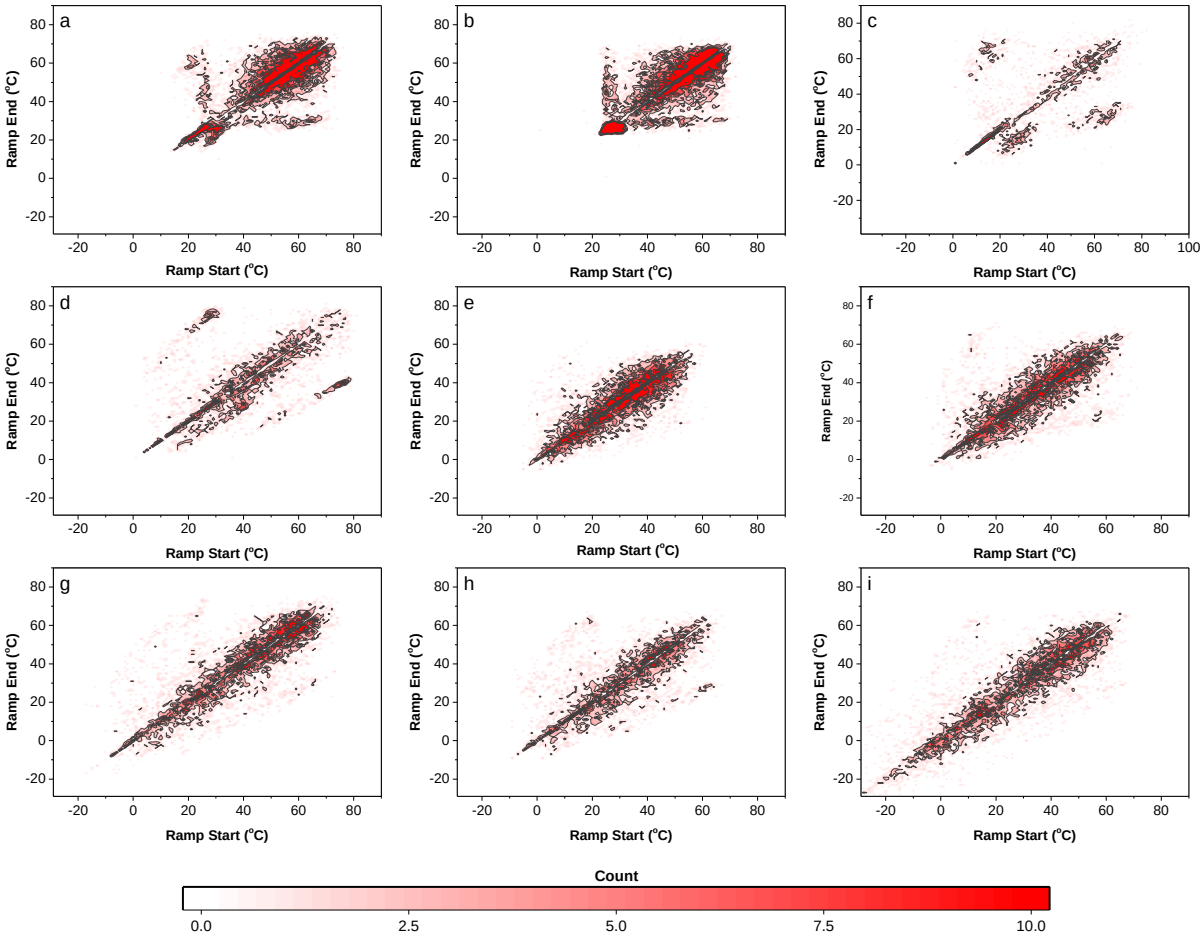

Figure 32: Ramping absolutes for (a) DAR (b) MAN (c) SOV (d) GOB (e) CAB (f) CNR (g) E13 (h) CAR (i) REG

Ramp Rates

The influence of the rate of temperature change (or ramp rate) on the reliability of solder joints is well documented within the electronic packaging industry, with higher ramp rates resulting in more serious damage at the solder/substrate interface [90] [91]. Ramp rates at each location have therefore been evaluated and are measured simply as the change in temperature over the duration of a ramping event. The maximum and average rate of change of module temperature for each site are outlined in Table IV. The highest maximum ramping rates occur within the hot and dry climates. However, the highest average ramping rates are in the hot and humid climates. This

is likely due to the rapid rise of module temperature at sunrise in the hot and dry climates of GOB and SOV, with few occurrences of intra-day ramping events. The hot and humid climates experience significantly more intra-day fluctuations contributing to a higher average ramping rate. CAB, CNR, E13 and REG all display similar average ramping rates, a reflection of their frequent intra-day ramping events. CAR exhibits a lower average ramp rate which is similar to the hot and dry climates, however has a lower observed maximum ramp rate. Whilst the sunrise ramping event is the dominant feature for CAR, the lower ambient temperature and irradiance results in a slower ramp rate.

Table IV: Maximum and Average ramping rates, K/s

Station	Max	Average
MAN	0.043278	0.007361
DAR	0.042333	0.009056
GOB	0.080944	0.005222
SOV	0.053333	0.005361
CAB	0.037528	0.006667
CNR	0.035889	0.006667
E13	0.049417	0.007056
CAR	0.032861	0.004861
REG	0.045528	0.007

Whilst the maximum observed ramp rates appear to be high, they are shown in Figure 33 to be relatively rare. The cumulative duration of ramp rates above 0.036 K/s is approximately 10 minutes for all sites

Out of a possible 8760 Hours in the year this figure appears extremely low, however, the damage potential at high ramping rates is not clearly understood and while it may seem insignificant relative to the rest of the year, these single events could generate sufficient stress to initiate cracks in solder bonds or cells.

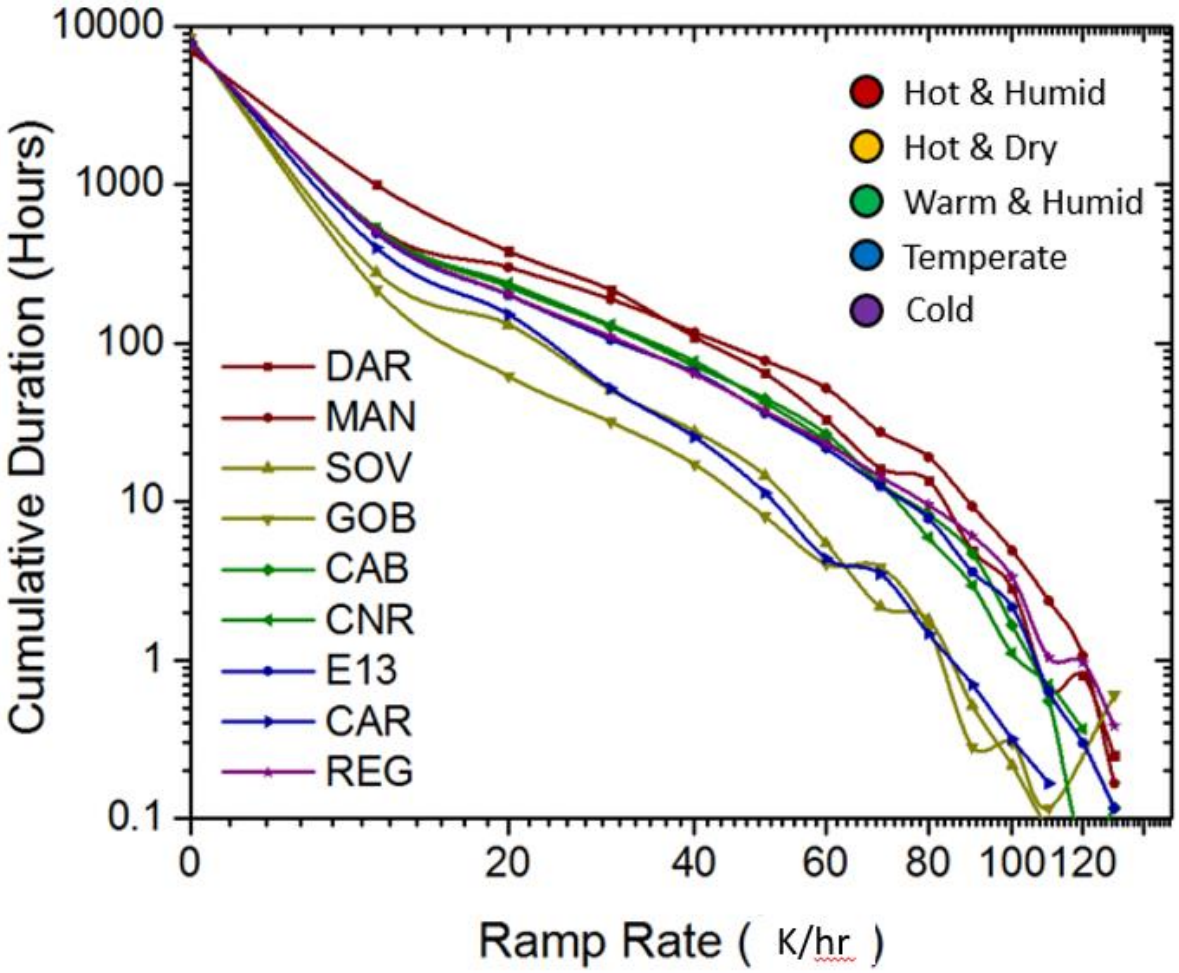

Figure 33: Cumulative time spent in hours for ramp rates between 0 and 0.33 K/s

Clearness Indices

Sky clearness, cloudiness and the consequential degree of irradiance exposure are determining factors which influence operating temperatures and the thermal behaviour of PV modules. The intermittency of cloud cover is responsible for fluctuations in the amount of irradiance incident on a module surface, which, subsequently results in fluctuations in module temperatures. Woyte et al showed that the daily mean instantaneous clearness index, $\overline{K}$, correlated with fluctuations in instantaneous clearness indices such that the most significant number of fluctuations

are expected to occur during days where $\overline{K}$ = 0.5 to 0.7, which are indicative of days with intermittent cloud cover [92]. In addition, days which are predominantly clear-sky ($\overline{K}$ = 0.8 – 0.9) or overcast ($\overline{K}$ = 0.1-0.3) experience more stable irradiance exposure. Instantaneous clearness indices, K_t, are evaluated for each site according to Eq. (7).

$$K_t = \frac{G_t}{I_o E_o cos\theta_i} \tag{7}$$

Where G_t is the total irradiance incident on the surface, Io = 1367 W/m^2, the solar constant, Eo is the correction factor accounting for the eccentricity in the Earths orbit, θ_ι is the angle of incidence. The mean number of ramping events for values of $\overline{K}$ are plotted in Figure 34**.** As anticipated, days with mean instantaneous clearness indices of 0.5-0.7 demonstrate, on average, the most number of ramping events. Whilst days with more stable conditions i.e. clear-sky and overcast, exhibit far fewer ramping events.

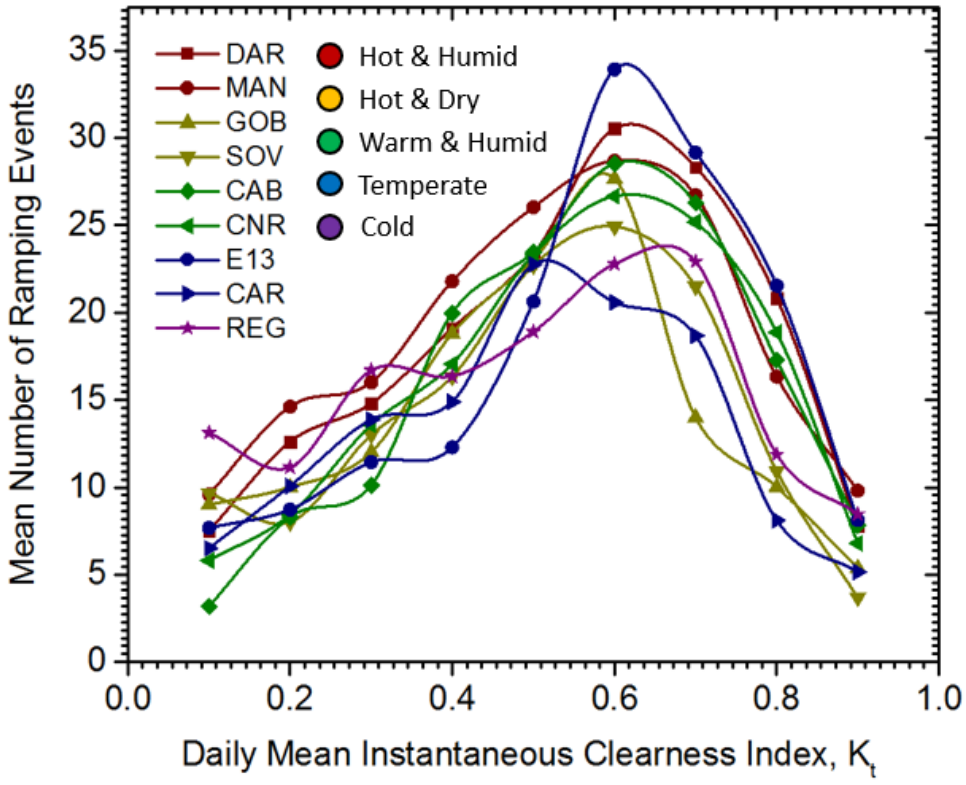

Figure 34: Mean Number of Ramping Events for values of daily mean instantaneous clearness index, $\overline{K}$

With this in mind, we consider the frequency distribution of $\overline{K}$ for each site. Figure 35 shows that the hot and dry climates (GOB, SOV) demonstrate consistently high values of $\overline{K}$, indicating frequent clear sky days with little to no cloud movement. As such, short-term fluctuations in module operating temperatures are expected to be less frequent, with the sunrise and sunset ramping events being the most predominant feature. This reflects well with the results presented in Figure 30 where there are only 25% of the total observed ramping events compared with Hot and Humid climates. Additionally, a larger proportion of the ramping events are made up of larger ramping events indicative of sunrise and sunset events. A closer look at both these sites reveals that SOV experiences more days where $\overline{K}$ = 0.8, whilst GOB sees more frequent days where $\overline{K}$ = 0.9. This would account for the increased total number of ramping events seen in SOV, since $\overline{K}$=0.8 experience more ramping events on average. Contrary to the

Hot and Dry sites, the Hot and Humid (DAR, MAN) sites exhibit a higher frequency of days where $\overline{K}$ is in the range of 0.5 – 0.7. This is again reflected well in the results above, with these sites demonstrating a higher proportion of ramping events with short-range temperature changes, which is to be expected from days with intermittent cloud coverage. Values of $\overline{K}$ for MAN lie almost exclusively within the range of 0.4 to 0.8. The effect of which is clear in Figure 30, with MAN exhibiting the highest total number of ramping events, which are almost entirely made up of short-range temperature changes (< 30K). By comparison, DAR is subject to slightly more days with higher mean values of $\overline{K}$, which accounts for the sudden step in ramping events with greater temperature ranges. The Warm and Humid climates show very similar distributions of $\overline{K}$. With the exception that CNR has a slightly higher frequency of clear sky days, and CAB has a slightly more overcast days. In addition, CAB has around 5% more days where $\overline{K}$ = 0.5. All of this is reflected well in Figure 30, where CAB has slightly more smaller range ramping events and CNR closes the gap in total number of events with an increase in ramping events at higher range.

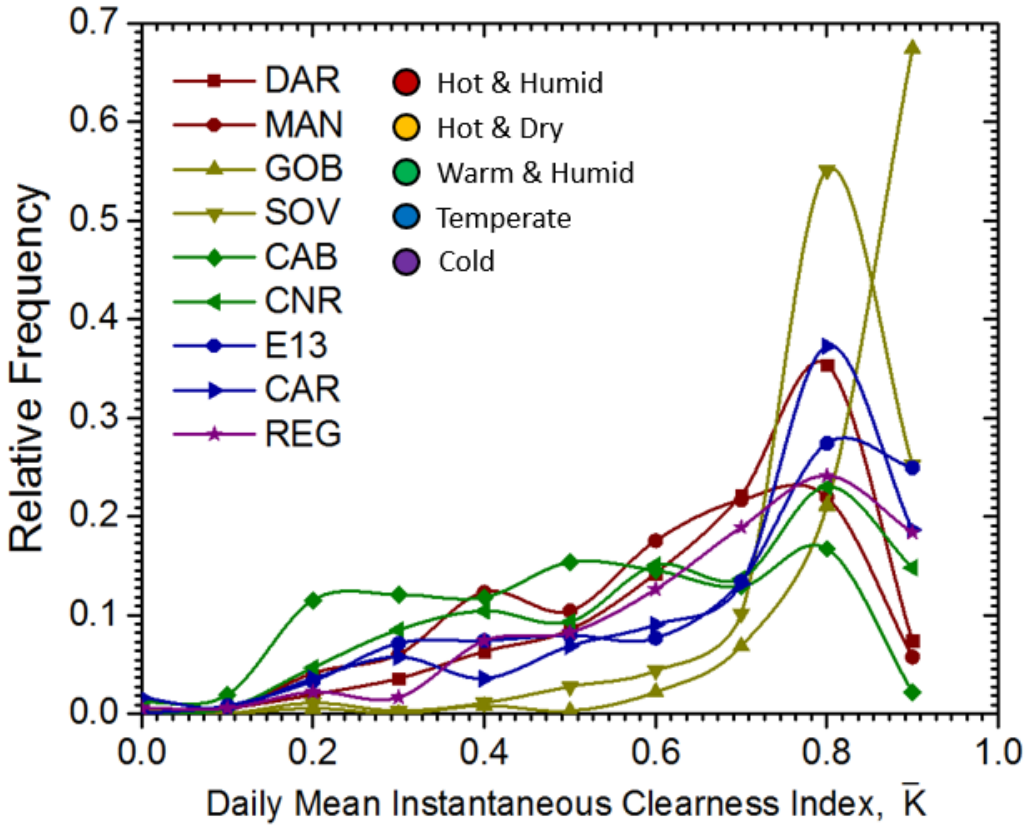

Figure 35: Relative Frequency of Daily Mean Instantaneous Clearness Index, $\bar{K}$

5.5 Conclusions

The dynamic thermal exposure of flat-plate silicon PV modules within different climatic conditions has been evaluated in this work. Module operating temperatures are shown to vary significantly between climates. Hot and Dry climates are regularly reported as having the highest rates of degradation for field-deployed modules than other climates, with solder bond degradation being a commonly observed failure mechanism. However, this does not necessarily mean that solder bond degradation is highest in these areas, and that other climates which experience the same temperatures are primarily suffering from different mechanisms, though the solder bond degradation could be as high if not higher. It is believed that cloudy days, or days with more fluctuations in module temperature, experience greater accumulation

of damage at the solder bonds and interconnects. For this reason, a thorough evaluation of module temperature fluctuations was carried out in this work. It was found that hot and humid climates experienced the highest frequency of temperature fluctuations whilst hot and dry climates experienced far fewer. Temperate and cold climates also experience a high number of temperature fluctuations, though somewhat less so than the hot and humid climates. Observations of the exposure to absolute temperatures reveals that the hot and humid climates are consistently exposed to high temperatures rarely ever falling below 20°C, whilst the other climates often cover a wider range of temperatures and fall to much lower temperatures. The influence that this has on the components should be investigated further. Encapsulants typically demonstrate temperature-sensitive material properties, usually becoming softer and less mechanically stable at higher temperatures and conversely becoming more brittle at low temperatures. The effect this has on the module in terms of thermomechanical behaviour is not well understood and should be considered in the future. Additionally, creep strain of solder is known to be higher at elevated temperatures which might suggest that the creep fatigue mechanisms are greater in the hot and humid environments where modules heavily exposed to high temperatures.

Whilst categorising the climate types by mean monthly temperature and humidity proved to be largely correct, the sites of the same category demonstrating the same thermal profiles, some improvements could be made. Site E13 fits into the Temperate climate according to the classification criteria, however, its profile had greater similarities with the Warm and Humid climate type. A study of clearness indices found that there existed a correlation between daily mean instantaneous clearness index and number of ramping events. Sites which experienced a greater number of clear skies (clearness index of 0.8-0.9) also experienced fewer ramping events,

compared with sites that had more cloudy days (0.5 - 0.7). E13 was found to be similar to the Warm and Humid sites in terms of relative frequency of clear sky days and total number of ramping events. For these reasons, it may be more appropriate to use mean monthly maximum temperature and daily mean instantaneous index to classify climates in terms of thermal exposure and thermomechanical degradation potential.

Chapter 6

Thermomechanical Behaviour of Photovoltaic Modules

6.1 Introduction

A better understanding of the influence that thermal exposure has on the degradation mechanisms for PV modules requires an observation of the stresses and strains experienced by the module components. Due to the complex nature of PV module assemblies, measurements of the mechanical stresses during normal operation presents a difficult challenge. FEM is employed in this work to develop a better understanding of the mechanical stresses and strains experienced by PV modules under varying thermal conditions and to calculate solder bond degradation over time, a critical issue in the reliability and durability of PV modules.

6.2 Finite-Element Model

The finite-element method (FEM) is a popular numerical technique used to solve complex mechanical problems. There are a wide range of software packages available such as Comsol Multiphysics, Ansys, Abaqus, Nastran and more. Whilst each package has their own strengths and weaknesses the general means of operation is the same. Each software requires the input of a geometric model, material properties and loading (or boundary) conditions which could include temperature, external forces, magnetic fields etc. FEM packages simplify the challenge of continuum problems by

hiding the underlying mathematical procedures whilst still being transparent in their operation.

The basic principle behind FEM is to apply discretisation methods to approximate the partial differential equations (PDEs) which are used to express the laws of physics for space and time-dependent problems. In FEM, a continuous body is divided into multiple simplified components or geometries called *finite elements*, the total assembly of which is called a *mesh*. Elements come in a variety of shapes with some of the more common ones shown in Figure 36.

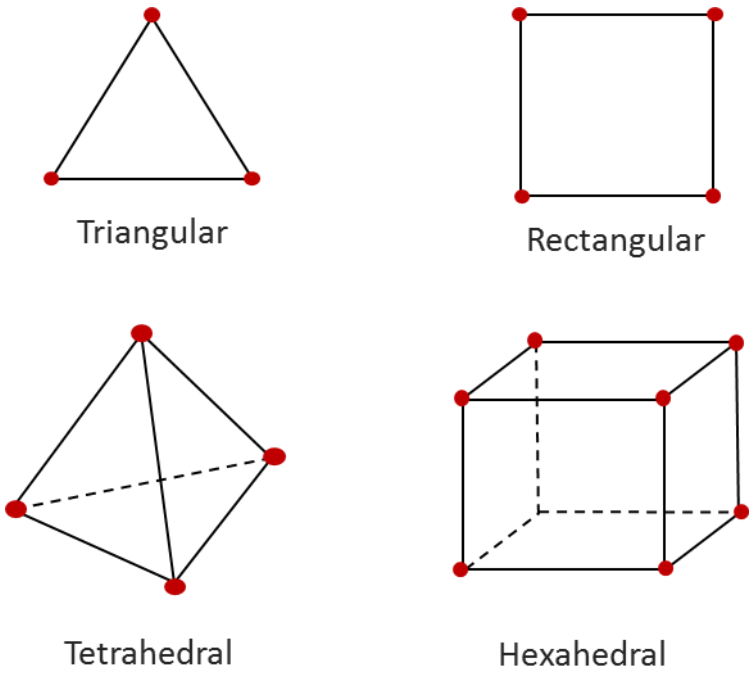

Figure 36: Common element geometries for 2D and 3D meshes with nodes indicated in red

At the corner of each element exist points called *nodes*, though some elements will also have nodes along the midsides. The nodes are points where the elements are connected. When approximating the displacement of a body under a load condition, the problem of finding the displacement of an infinite number of points in the body is replaced with the problem of finding the displacement of a finite number of points, i.e. the nodes. For a two-dimensional model, the displacement of each node consists

of two components, one parallel to a reference x-axis and one parallel to a reference y-axis. These components are referred to as *degrees of freedom* (DOF). Therefore, for a mesh made up of n nodes, the total DOF would be $2n$, compared with an infinite DOF which would exist in the non-discretised version of the model. The computational requirements for an analysis is heavily dependent on the DOF and keeping this low whilst also maintaining a reasonable level of accuracy is one of the primary challenges of FEM.

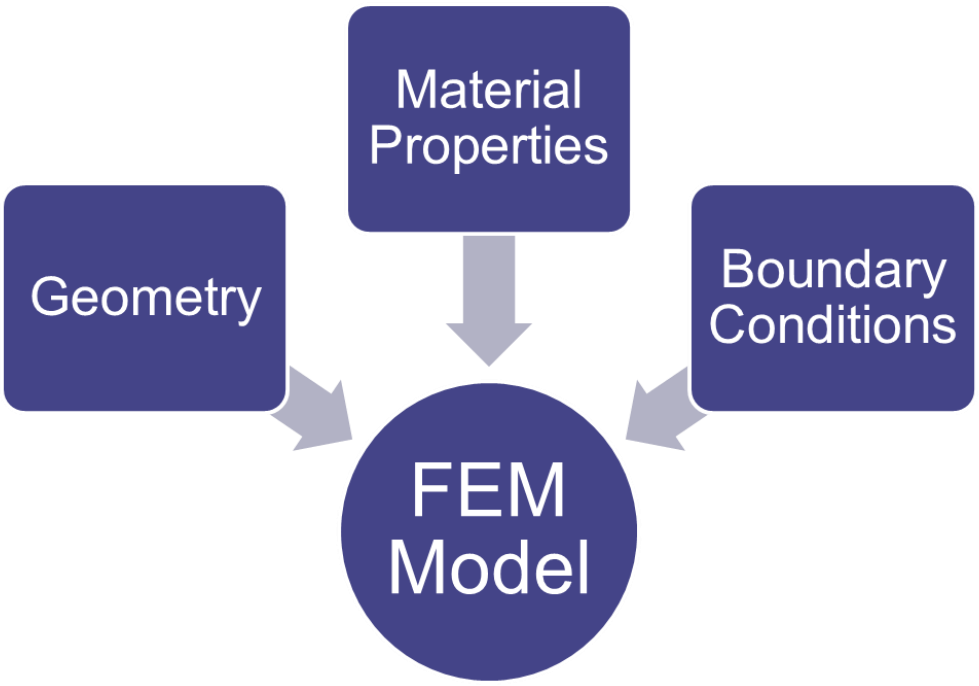

Figure 37: Simplified workflow for an FEM model

In this work, COMSOL Multiphysics was the selected software package. COMSOL boasts a seamless interface between physics fields allowing for true multiphysics interactions while other packages generally require physical loading conditions to be simulated sequentially. For example, in Ansys, heat transfer must be simulated first, then the thermomechanical response after. In addition, COMSOL maintains complete transparency for the partial differential equations used and has greater flexibility by allowing governing equations to be modified or even created anew. For this reason,

COMSOL is a popular choice in academia where the implementation of new methods might be necessary, compared with industry which would prefer to use existing models.

A 2D cross-sectional finite-element model has been developed reflecting mini-modules which are fabricated on-site at Loughborough University. The modules are made up of six monocrystalline silicon cells connected in series via solder-coated copper-based ribbon tabs. The assembly is encapsulated within ethylene vinyl-acetate (EVA) binding together a float glass front cover and polymeric backsheet.

Geometry

A top-down schematic is given in Figure 38 whilst a screen capture of the model is show in Figure 39. Eitner et al [93] previously demonstrated the change of gap size between cells during thermal cycling. It is assumed that, even with the inclusion of a ribbon kink, this changing gap size will have some influence on the strains applied to the ribbon and solder bonds and as such the interconnection between cells is included in the model. In determining the length of the ribbon interconnect, simulations are first conducted to determine the total change in gap size. The ribbon link is then designed accordingly. The dimensions for each component are summarised in Table V. The thicknesses of each material, except the EVA, were measured before lamination at room temperature using a micrometer. In the case of the EVA, thickness measurements were conducted on free-standing sheets following optimal curing conditions.

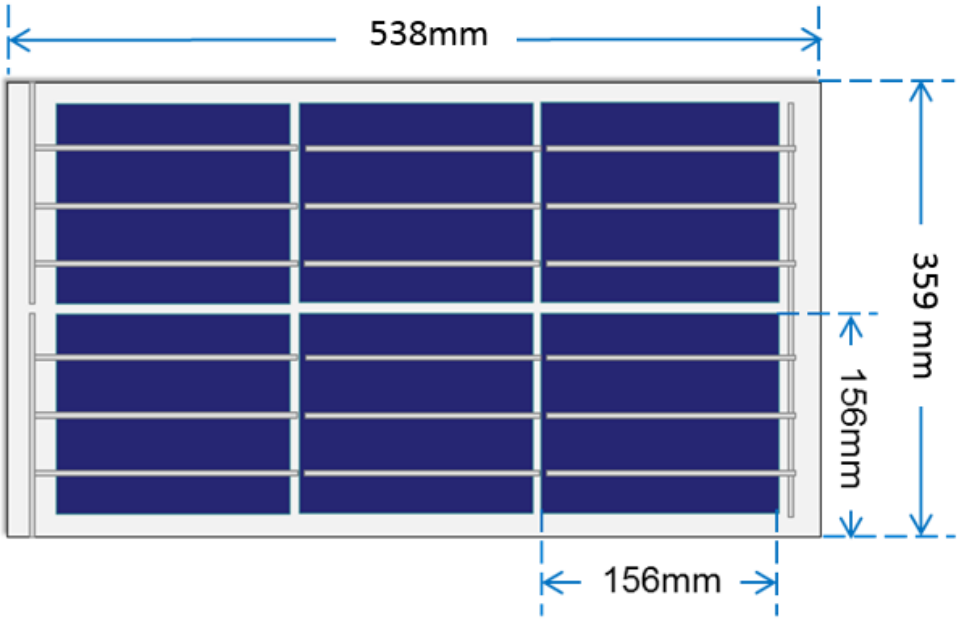

Figure 38: Top-down schematic of mini modules fabricated on-site

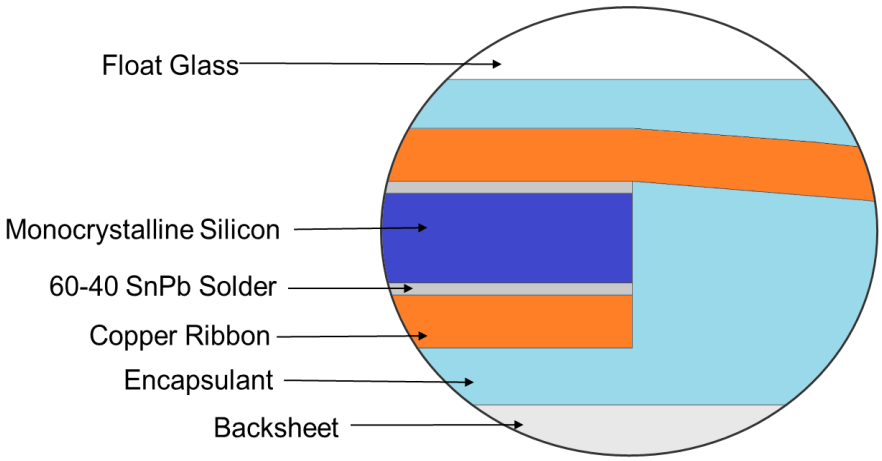

Figure 39: Screen capture of the 2D FEM model focused on the edge of a cell, the interconnecting ribbon between two cells is visible

Table V: Dimensions of each component used in the model, mm

Component	Length	Width	Height
Cell	156	156	0.22
Glass	538	359	2.9
Encapsulant	538	359	0.62
Backsheet	538	359	0.41
Ribbons	156-390	1.5	0.13
Solder	156	1.5	0.02

The cells used feature a single solder tabbing tab across the length of the front surface and 3 discretised solder tabbing on the rear surface. It is later shown in Figure 58 that the front surface solder is subject to the highest rate of deformation and is the only bond to be used to calculate viscoplastic deformation to reduce the computational requirements. Further reductions in computational requirements can be achieved by modelling the rear surface solder bond as a single layer rather than the discretised pads.

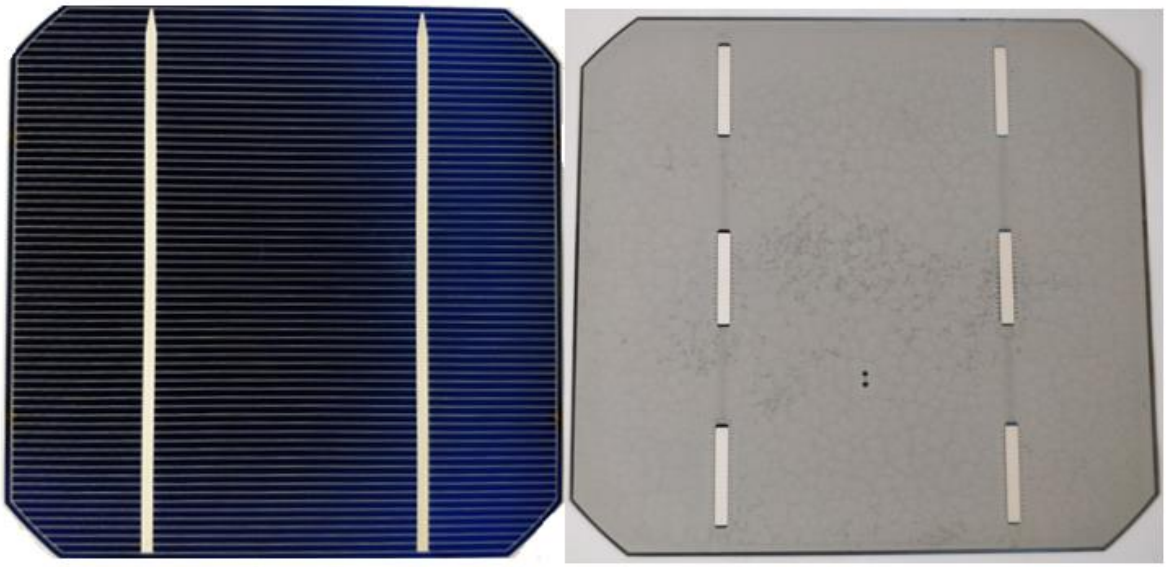

Figure 40: Front side and rear side of Silicon cells after which the model is developed

Material Properties

Appropriate simulation of deformation and subsequent stress in the assembly require accurate characterisation of the materials in use. These values have either been determined experimentally, or otherwise furnished from manufacturer datasheets. For this model, the coefficient of thermal expansion (CTE), density, Young's modulus and Poisson's ratio are the properties required to simulate the thermal expansion, displacement and stress.

Float Glass

The standard front cover for PV modules consists of a sheet of float glass. Its name refers to the float process by which it is produced. Float glass has a very high viscosity and can be considered purely elastic below the glass transition temperature of 550^{o}C [94]. Stress-strain curves for glass show linear elastic material behaviour until fracture. The mechanical property values are well-documented and are thus furnished from the literature for this work [95][94]. Density is 2500 Kg/m^{3}, Young's modulus 73 GPa, coefficient of thermal expansion is 8x10^{-6} 1/K and Poissons ratio of 0.4.

Ethylene Vinyl Acetate

The material used in this work is a fast-curing EVA. Whilst some of the material properties are provided by the manufacturer datasheet, this is quite limited in that the temperature dependencies of Young's modulus and CTE are not provided and are considered to be important factors when considering the displacement of cells during thermal changes [96]. The temperature-dependency of these values is therefore determined experimentally. Using a TA Instrument Dynamic Hybrid rheometer, the storage modulus, G, is measured during a temperature ramp from -40 to 150°C at 0.83 K/s with an oscillation frequency of 1Hz. The results of which can be seen in Figure 41.

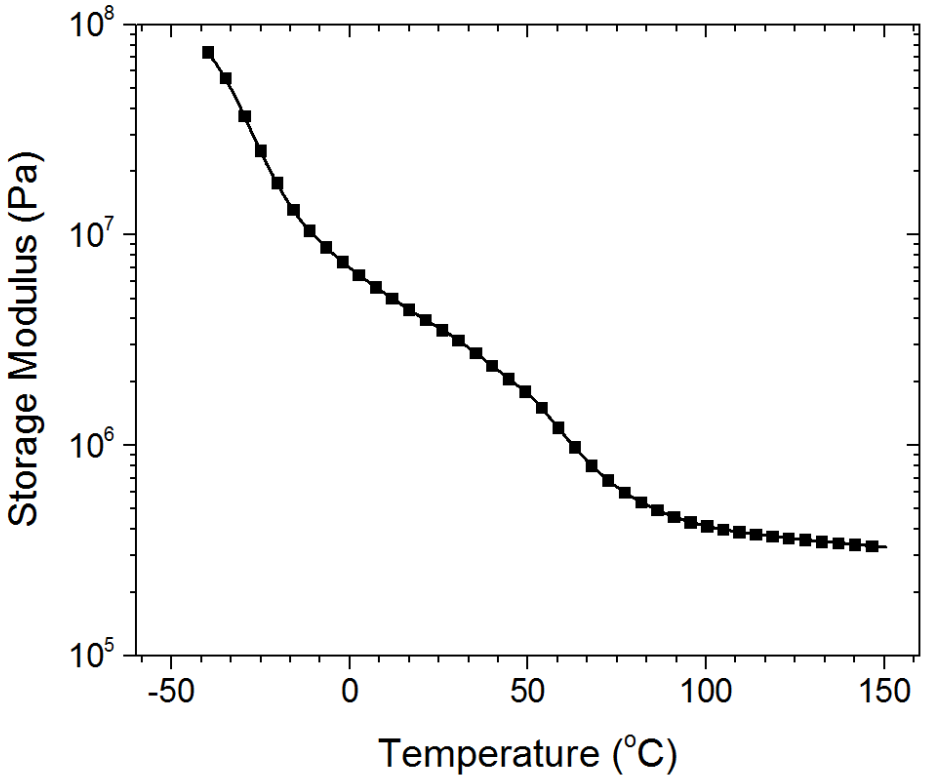

Figure 41: Temperature-dependent storage modulus of EVA measured at 1Hz

Monocrystalline Silicon

Monocrystalline silicon (c-Si) wafers are very brittle with very low ductility and are best described as linearly elastic. In this work, the cells are modelled as a single homogenous body. Metallisation and interconnection grooves are assumed to have a negligible effect on thermomechanical behaviour and are therefore omitted in the interest of reducing the complexity of the model. Due to the crystallographic structure of Silicon, the material properties can be described as anisotropic, where Young's modulus is dependent on the loading direction. For c-Si wafers with surface normal in <100>-direction and edges along the <010> and <001>-directions, the stiffness matrix, C, is given as (1).

$$C = \begin{bmatrix} C_{11} & C_{12} & C_{12} & 0 & 0 & 0 \\ C_{12} & C_{11} & C_{12} & 0 & 0 & 0 \\ C_{12} & C_{12} & C_{11} & 0 & 0 & 0 \\ 0 & 0 & 0 & C_{44} & 0 & 0 \\ 0 & 0 & 0 & 0 & C_{44} & 0 \\ 0 & 0 & 0 & 0 & 0 & C_{44} \end{bmatrix} \quad (1)$$

The values of C_{11}, C_{12} and C_{44} are given as 166, 64 and 80GPa, respectively [97]. Young's modulus for each loading direction E<100>, E<110> and E<111> is given in Table VI.

Table VI: Young's modulus for loading directions

Direction	Equation	Value (GPa)
E<100>	$C_{11} - 2\frac{C_{12}}{C_{11}+C_{12}}C_{12}$	130
E<110>	$4\frac{(C_{11}^2 + C_{12}C_{11} - 2C_{12}^2)C_{44}}{2C_{44}C_{11} + C_{11}^2 + C_{12}C_{11} - 2C_{12}^2}$	170
E<111>	$3\frac{C_{44}(C_{11}+2C_{12})}{C_{11}+2C_{12}+C_{44}}$	189

As in most materials with cubic symmetry, the CTE of c-Si is isotropic. However, the CTE of c-Si is temperature-dependent. Figure 42 shows the CTE with temperature. The density is 2.3 g/cm^3.

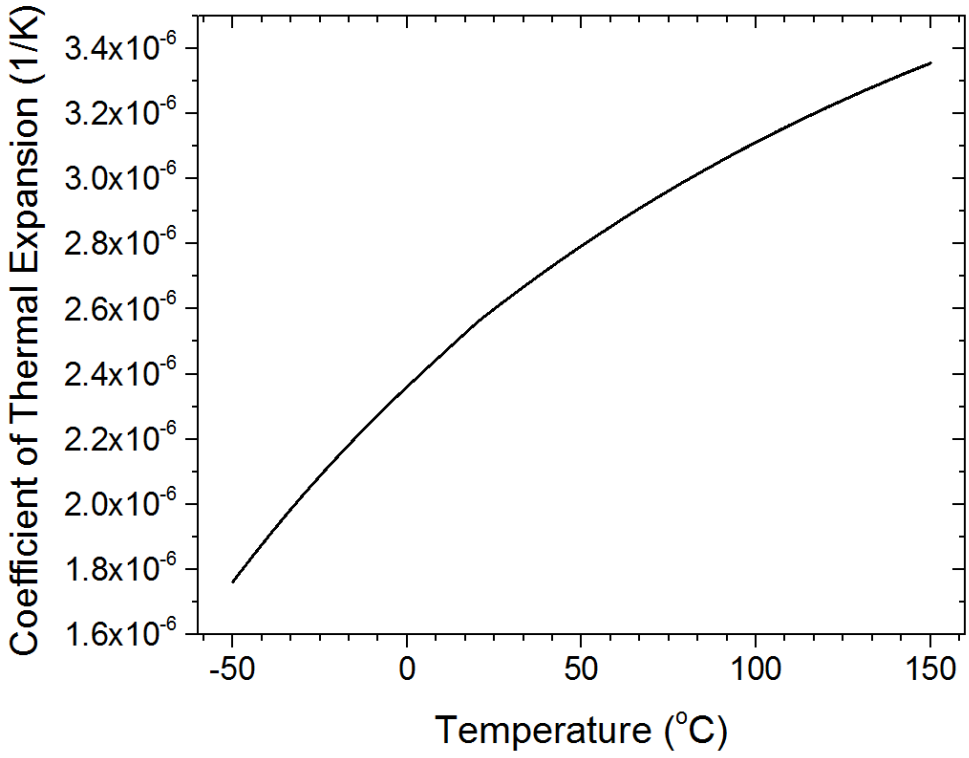

Figure 42: Temperature-dependent coefficient of thermal expansion for monocrystalline silicon [98]

Flat Ribbon Wire

Flat ribbon wires used for PV modules are made up of a copper alloy core with thicknesses in the range of 0.1-0.15mm which is coated in a 0.02mm thick solder alloy. In this work, the mechanical properties of the entire ribbon are implemented, as opposed to modelling the copper and solder coating separately. Material data was furnished from the manufacturer. The temperature-dependent Young's modulus and CTE are presented in Figure 43 and Figure 44, respectively, where the density is 8500 kg/m^3 and Poissons ratio is 0.4.

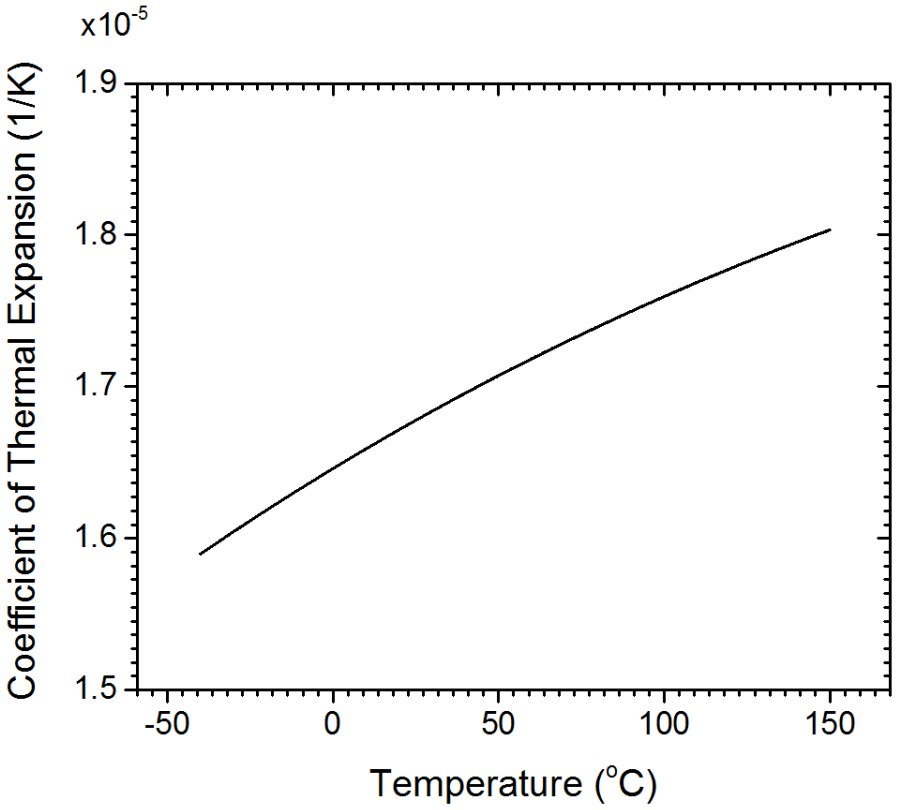

Figure 43: Temperature-dependent coefficient of thermal expansion for copper

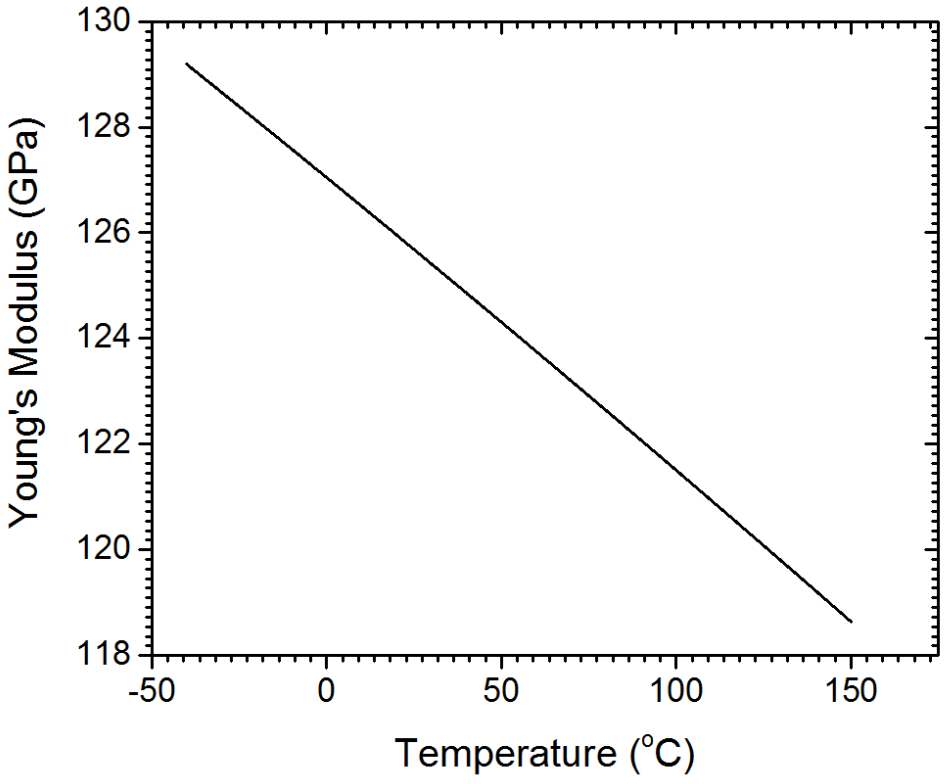

Figure 44: Temperature-dependent Young's Modulus for Copper

60Sn40Pb Solder Alloy

Whilst there are a plethora of available solder alloys, eutectic 60Sn40Pb is probably the most commonly used in the microelectronics industry. The alloy has a melting point temperature of approximately 188°C, meaning it has a high homologous temperature so, even at room temperature, 60Sn40Pb solder will undergo some degree of creep deformation, which becomes even more severe at the elevated temperatures experienced during normal operating conditions. Density, Young's modulus and CTE are well-defined material properties.

In this work, the inelastic deformation of the solder bonds during normal operating conditions is one of the primary investigations and is modelled using Anand's viscoplastic model described earlier in chapter 4. The model requires some input parameters to accurately define the behaviour of the material being modelled. These parameters have previously been determined for 60Sn40Pb by Wang et al [99] and are given in Table VII.

Table VII: Anand Viscoplastic model parameters for eutectic 60Sn40Pb solder alloy.

Parameter	Value
A	1.49×10^7
Q (j/mol)	90046
ζ	11
M	0.241
h_0	2640
$\hat{s}$ (MPa)	80.42
n	2.31
a	1.34
S_0	56.3

Backsheet

The backsheet used in this study is a common configuration of Tedlar® PVF/PET/ Tedlar® PVF. The behaviour of the backsheet can be quite complex given its multi-

layered nature. Simulating each layer and their interactions increases the DOF and computational requirements to an unreasonable level and so the backsheet is instead treated as a single layer. Material properties are furnished from the manufacturer datasheet with a density of 2.5 g/cm^3, coefficient of thermal expansion 5.04x10^{-6} 1/K, Poissons ratio of 0.29 and temperature-dependent Young's modulus shown in Figure 45.

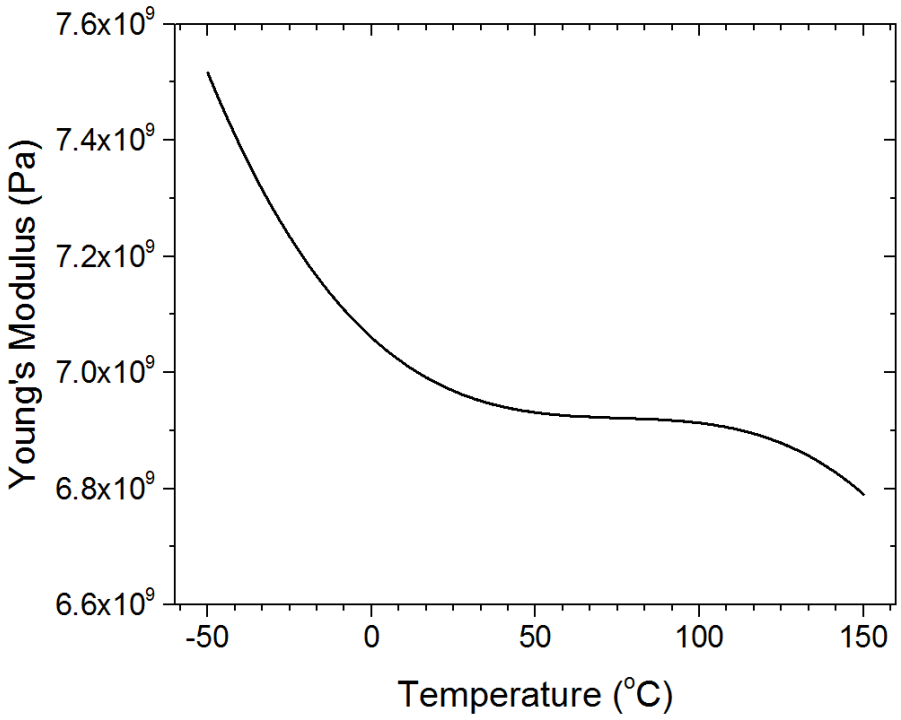

Figure 45: Temperature-dependent Young's modulus for Tedlar® PVF/PET/ Tedlar® PVF backsheet.

Mesh Optimisation

By definition, finite-element simulations can only ever serve as an approximation to a true solution of a problem as a result of a computers inability to calculate infinitesimally small problems. Aside from use of appropriate material property values and load conditions, the other major choice made by the user is the density of the mesh and the number of degrees of freedom. Mesh optimisation is conducted in

order to provide a level of confidence in the simulation results whilst also maintaining a reasonable computation time. The thermal cycling profile (TC200) is applied to the model and simulations are conducted with decreasing mesh size. Solder bond damage accumulation is used to compare the accuracy of the simulations. It is found that an initialisation period occurs during the first 10 cycles, and that by the 10^{th} cycle the damage accumulation on the solder bonds settles into a steady rate. As such, 10 cycles are simulated at each mesh size. The finest possible setting is used as a benchmark, as it is the most accurate solution possible, but requires significant computation time. Figure 46 shows the normalised solder damage generated by each successive cycle for every mesh size. Damage accumulation on the 10^{th} cycle at the finest mesh size is 17kPa with $1.3x10^6$ degrees of freedom. For the meshes generated by COMSOLs algorithms, the fine setting settled within 1% of the finest setting by the 10^{th} cycle with $8.5x10^5$ degrees of freedom, whilst the normal setting came within 5% of the finest model by the 10^{th} cycle with $6.7x10^5$ degrees of freedom. Despite being a significant reduction in degrees of freedom, the computational requirements were still unreasonable, taking more than 5 hours to complete 10 cycles at the normal setting. Whilst further reductions could be made by increasing the mesh size, the deviation from the finest size became too high. A custom mesh is developed which focuses a finer mesh size on the solder bonds and cell, while having a coarser mesh on the glass, encapsulant and backsheet. This enabled a significant reduction of degrees of freedom to $2x10^5$, which considerably reduced computational demand whilst also settling to within 2% of the finest mesh setting.

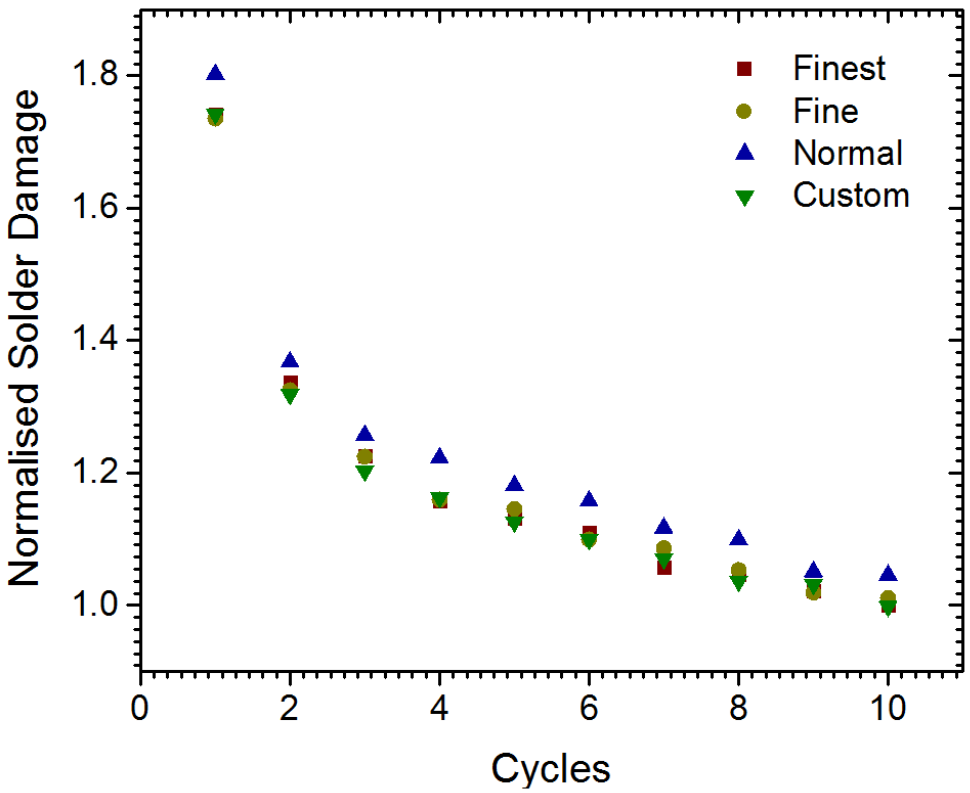

Figure 46: Normalised solder damage per cycle for 3 default mesh size settings and the custom made mesh

A mesh quality analysis was conducted during the development of the custom mesh to ensure reasonable quality of the mesh elements, particularly around the solder bonds. Mesh element quality is evaluated based on skewness, which is a measure based on the equiangular skew of each element such that elements with angles much larger or smaller than expected of an ideal element are penalised depending on the size of the angle. Element quality is described on a scale of 0 to 1, where 1 is the best possible quality indicating an optimal element and 0 represents a degenerated element. Generally, mesh element quality of less than 0.1 is considered poor. In this work, an average mesh element quality of 0.5 was sought. Figure 47 presents a screen capture of the quality of the final mesh around the edge of the inner cell. An average element quality of 0.8 was achieved, whilst element quality around the solder bonds was consistently above 0.7.

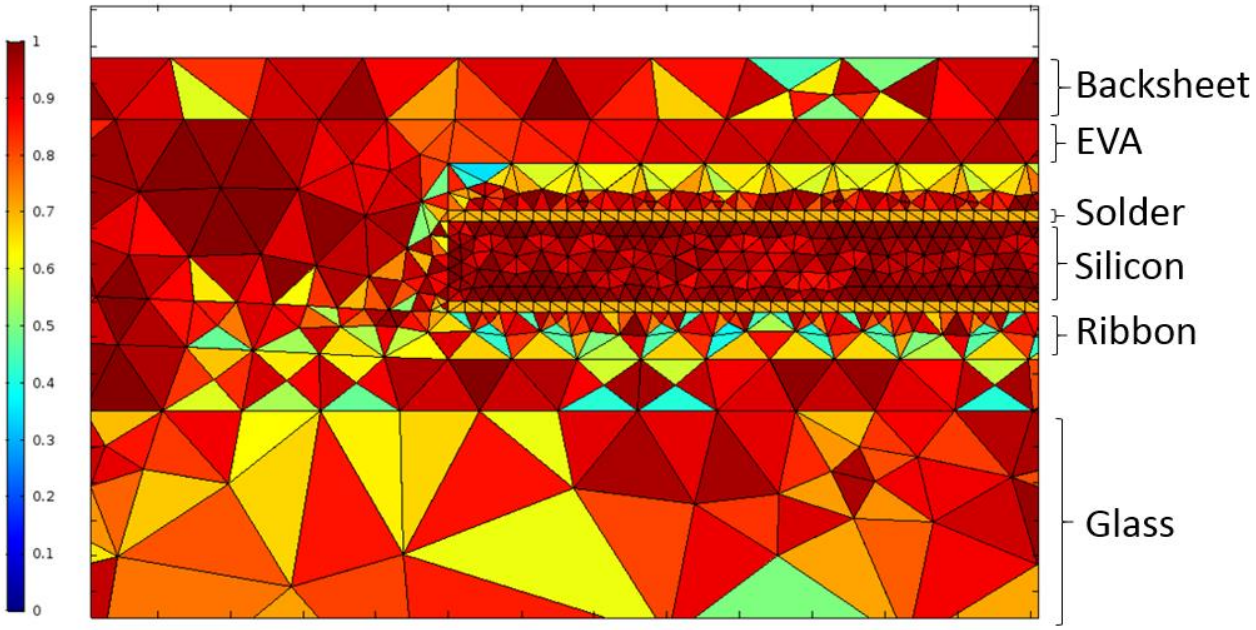

Figure 47: Mesh element quality plot for the edge of the inner cell

The custom mesh produced a single element thickness along the solder layer. Since solder deformation is the primary focus of this study, an additional refinement is conducted on this layer to provide an increased level of confidence in the displacement of the element nodes and the calculated shear stresses. A high density mesh is generated on the solder layer, as shown in Figure 48, which is 8 elements thick. A single thermal ramp from -40 to 85°C with ramp rate of 2K/min is conducted to compare the shear stresses of the high density mesh with the custom mesh. A comparison of the simulated shear stress for each mesh density is shown in Figure 49. It is shown that results are nearly identical with a mean bias error of 0.012. As such, successive simulations are conducted with the single-element thick layer.

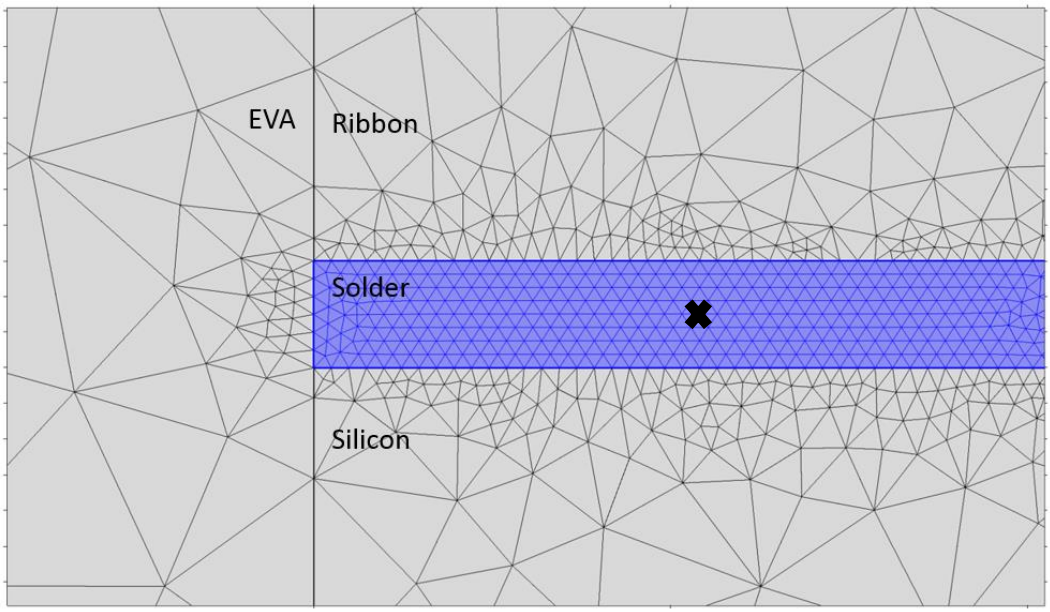

Figure 48: Screen capture of the model with high-density meshing on the solder layer. Cross symbol marks location of point analysis.

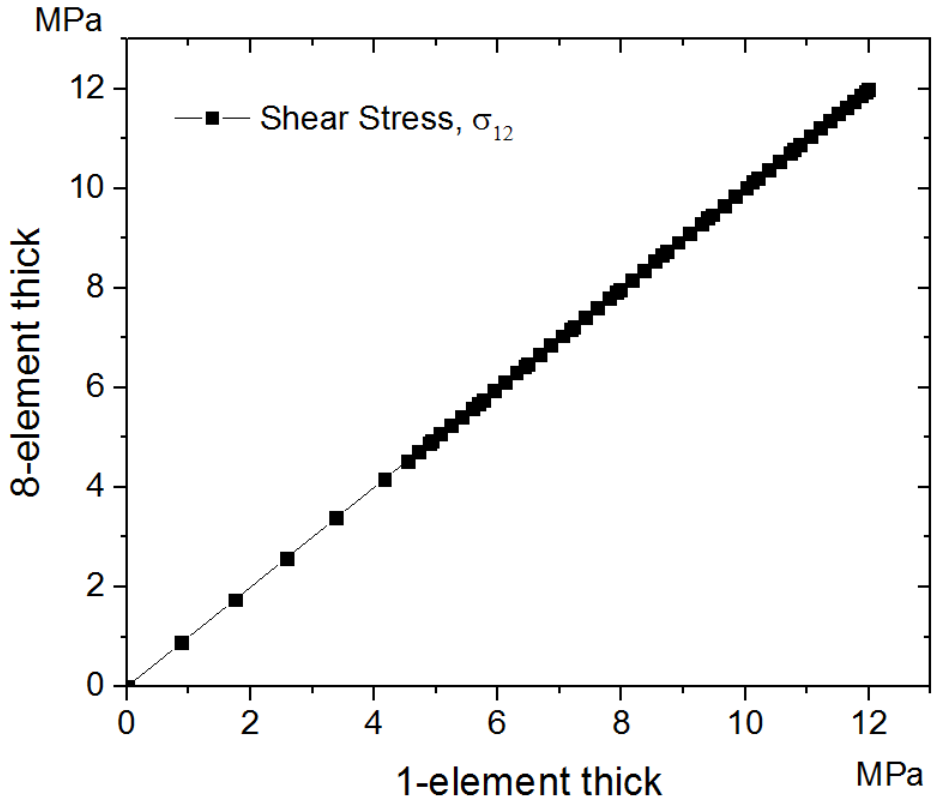

Figure 49: Comparison of shear stresses for 1-element thick model and 8-element thick model.

6.3 Thermomechanical Behaviour of PV Modules

The temperature profile for the IEC61215 thermal cycling 200 test is used to simulate the mechanical behaviour of the entire assembly and understand the effect of temperature on each component. For simplicity, module temperature is assumed to be homogenous throughout the entire assembly, in addition to this, the assembly is assumed to be relaxed at the start of the cycle (25°C).

Glass and Backsheet

The Von Mises stresses on the glass and backsheet at the high and low temperature dwells (85°C and -40°C) are presented in Figure 50 and Figure 51, respectively. The colour bar is representative of the Von Mises stress, whilst the arrows are indicative of the principal stresses where red, green and blue are the first, second and third principal stress, respectively. Arrowheads facing inwards represent compressive stress whilst arrowheads facing outwards represent extensional stress. Arrow length is proportional to the principal stress value. At the 85°C dwell (Figure 50) it can be seen that the highest stress occurs in the backsheet at around 50MPa. The lowest stress occurs on the outer surface of the glass, while the inner surface experiences slightly higher stress. The difference between the outer and inner surfaces are likely explained by the inner surfaces adhesion to the encapsulant, where the outer surface is free and therefore less restricted during thermal expansion. The principal stress indicates that the backsheet is under high compression, which is explained by the mismatch in thermal expansion coefficients. The backsheet has a much higher thermal expansion coefficient, approximately 15x higher than glass. As temperature increases the backsheets ability to expand is constrained by its adhesion to the other components which produces the compressive stresses seen and is also responsible for the high Von Mises stress. As a result of the large expansion of the backsheet, the module assembly bends as seen in Figure 52. Due to the nature of the bending, compressive stresses are

generated on the outer surface of the glass, whilst extensional stresses appear on the inner surface. The inner surface extensional stresses are also exaggerated by the expansion of the encapsulant.

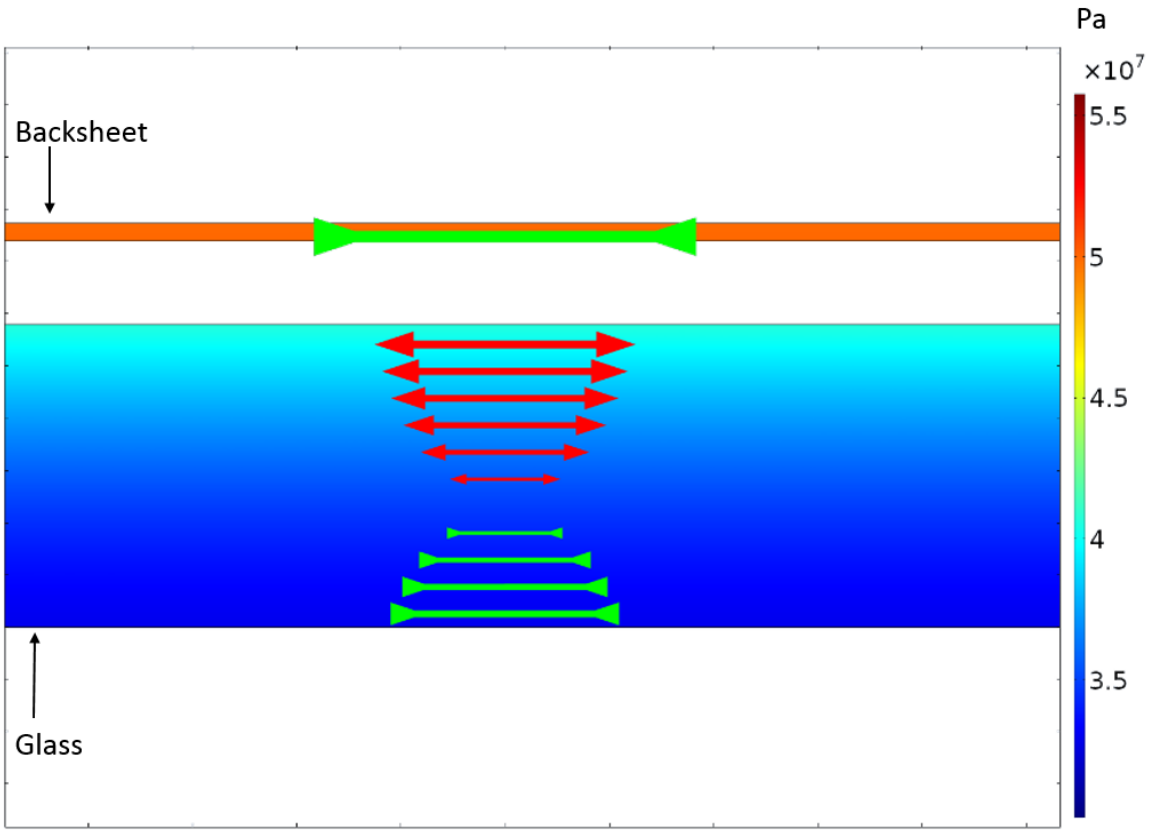

Figure 50: Cross-sectional screen capture of the backsheet and glass at the centre of the module at the onset of the high temperature dwell (85°C). The colour bar represents the Von Mises stresses and the arrows indicate the Eigenvectors for the principal stresses.

At the onset of the low temperature dwell (-40°C) the opposite occurs. In this case, the backsheet is contracting at a greater magnitude than the glass, but again is restricted by its adhesion so extensional stresses are generated. At -40°C the contraction of the backsheet pulls on the glass causing the module assembly to bend in the opposite direction to the 85°C condition, as shown in Figure 52. In this case, the inner surface of the glass experiences compressive stresses, as illustrated by the principal stress arrows in Figure 51, and the outer surface experiences extensional stress due to the

direction of the bending. Again, the stresses at the inner surface of the glass are higher due to the contraction of the encapsulant, which has a higher coefficient of thermal expansion than the glass and therefore generates additional stress.

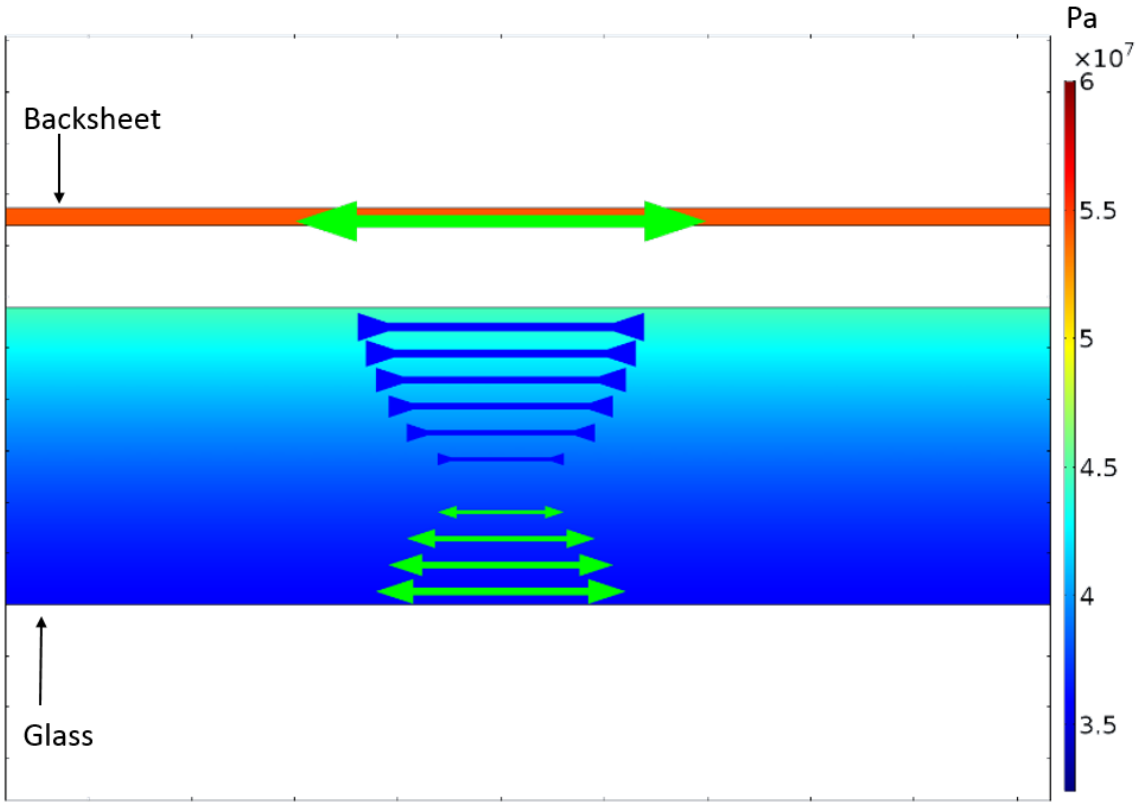

Figure 51: Cross-sectional screen capture of the backsheet and glass at the centre of the module at the onset of the high temperature dwell (-40°C). The colour bar represents the Von Mises stresses and the arrows indicate the Eigenvectors for the principal stresses.

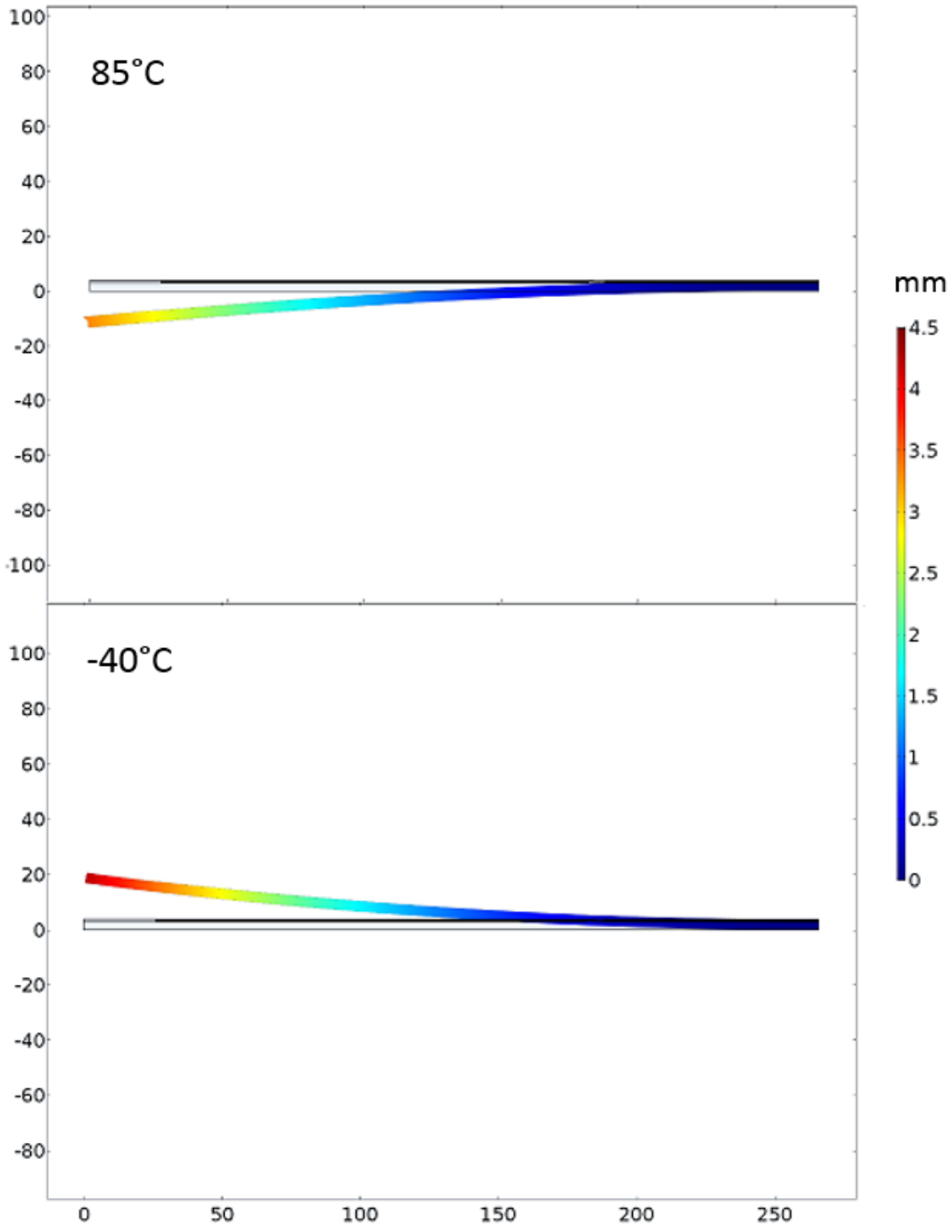

Figure 52: Total displacement in mm of the module assembly at 85°C and -40°C from the centre of the module to the left edge. The black outline represents the module in a relaxed state. Deformation graphic has been exaggerated to be more obvious.

EVA and Cells

Figure 53 shows the third principal stresses in the gap between the cells at the -40°C dwell. Strain within this region is between 4-7%, except at the corners of the cells where high strains of 11-14% occur. As expected, the strains are compressive, as indicated by the principal stress direction arrows.

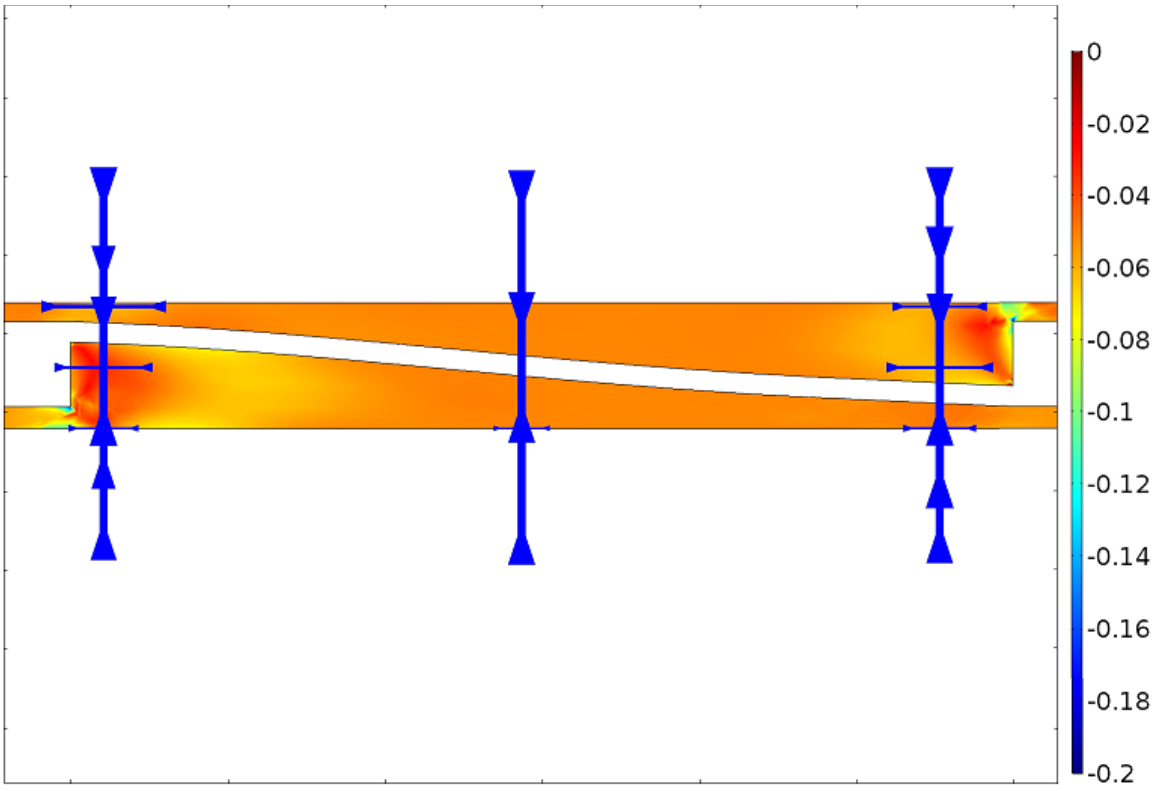

Figure 53: Third principal strains on the EVA in the gap between the cells at -40, colour bar indicates the third principal stress magnitude and arrows indicate the direction of the strain in the x and y directions

The silicon cells have the lowest thermal expansion coefficient of all the components in the module and therefore contract much less than the encapsulant, glass and backsheet. However, the contraction of the other components forces the cells to contract more leading to compressive mechanical stress of up to 130MPa as shown in Figure 54.

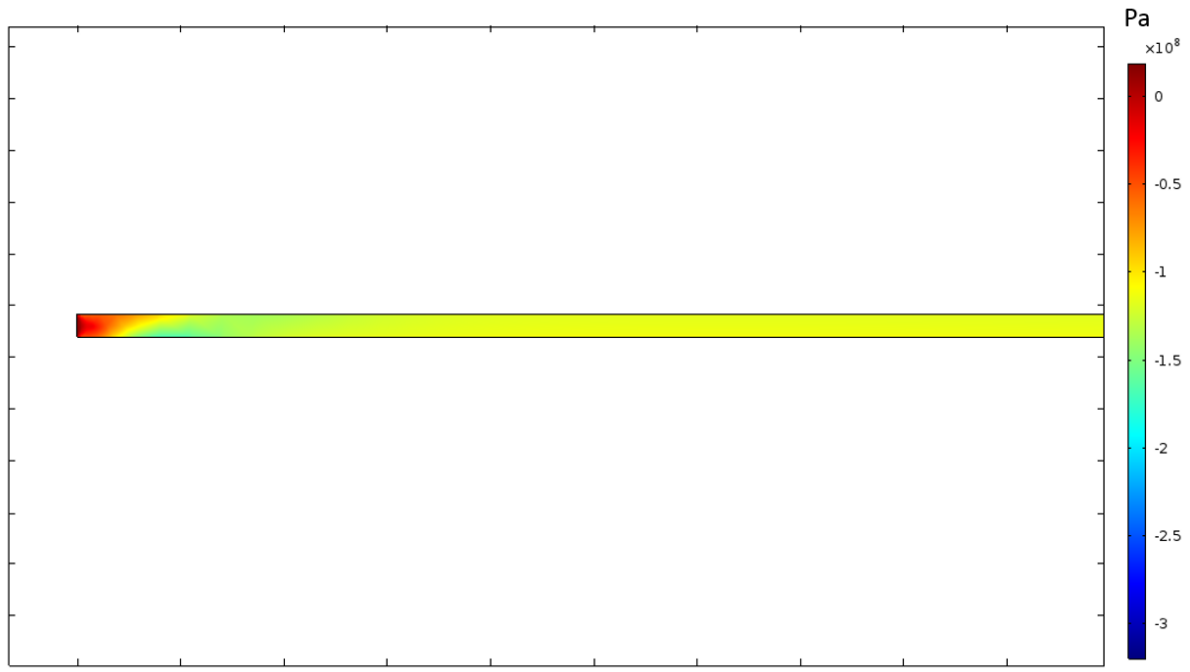

Figure 54: Third principal stress on the middle solar cell at -40°C

At 85°C, the EVA experiences small extensional strains in the range of 1-3%, with higher strains of 7-9% occurring at the corners of the cell.

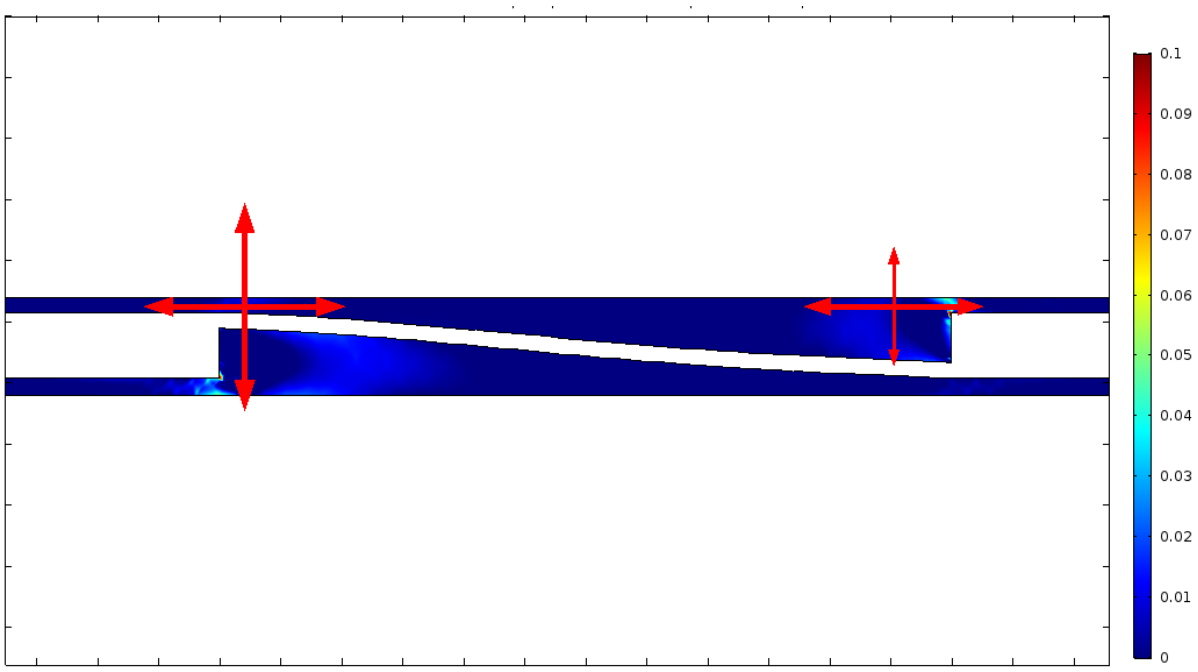

Figure 55: First principal strains in the EVA at 85°C with the strain directions indicated by the red arrows

Interconnects

The expansion and contraction of the assembly during changes in temperature forces the displacement of the cells and the interconnecting ribbons. This displacement, coupled with the mismatched expansion coefficients of the individual components, induces shear stresses in the solder bonds and interconnects. Figures Figure 56 and Figure 57 show the shear stress tensors at -40 and 85°C respectively. It can be seen that the stresses are highest at the edge of the solder which is joined with the interconnecting ribbon. Whilst the interconnecting ribbon has been designed with an s-bend shape in order to accommodate for the cell displacement, the bending and displacement of the ribbon still generates additional stresses.

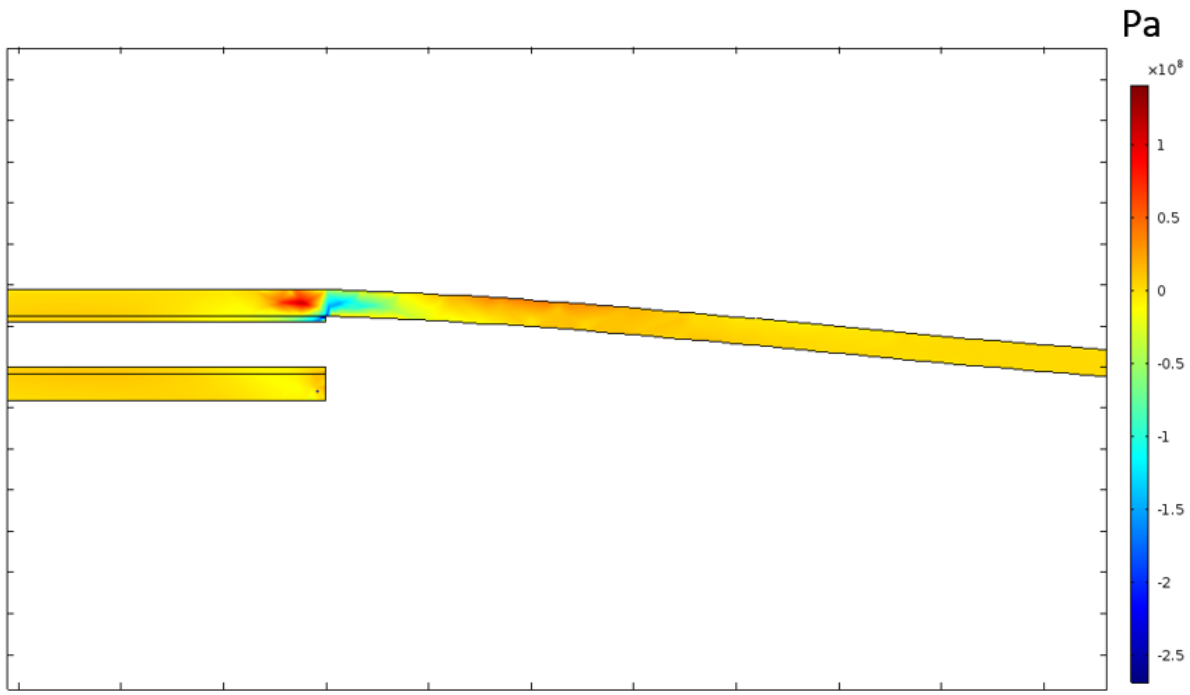

Figure 56: Shear stresses (xy-tensor) on the interconnections at -40°C

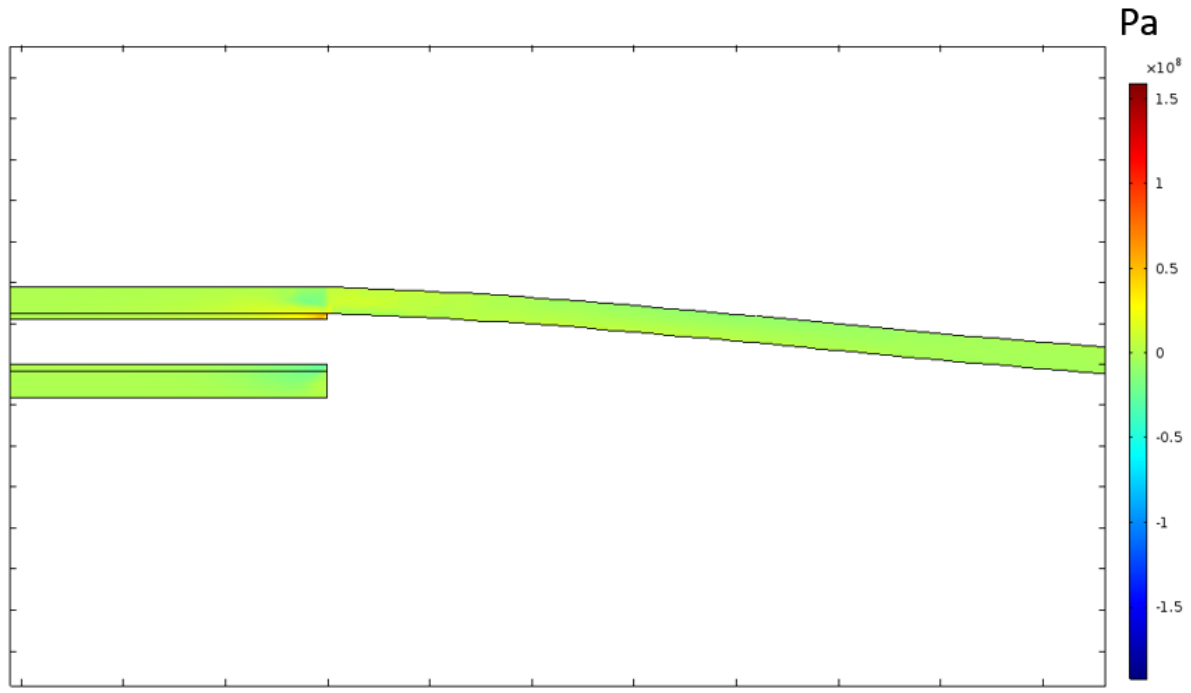

Figure 57: Shear stresses (xy-tensor) on the interconnections at 85°C

6.4 Solder Bond Degradation

As previously discussed in chapter 2, degradation of the solder bonds is commonly reported as one of the major mechanisms contributing to performance degradation in PV modules in the field. Whilst solder bond degradation has largely been attributed to hotter climates, it is not fully understood to what effect different climates have of the rate of degradation and what factors contribute the most damage. In this section, the FEM model is used to calculate the viscoplastic deformation of solder bonds through operating temperatures for each of the locations presented in chapter 5.

Inelastic strain energy density or energy dissipation density, is a metric used for determining irreversible deformation which is synonymous with damage. An empirical fatigue model for solder bonds developed by Darveaux [100] considers the accumulation of inelastic strain energy density as an indicator to predict crack

initiation and crack growth. In this work, the inelastic strain energy density or energy dissipation density is used as a metric for total damage of the solder bonds.

Thermal Cycling

Simulating the thermal cycling 200 accelerated ageing test is a useful first test to understand solder bond degradation behaviour and can be used for comparison with future outdoor simulations. Figure 58 is a screen capture of the solder bonds of the middle cell at the onset of the high temperature dwell during a thermal cycle. The solder bonds for the middle of the module dissipate the most energy, in addition to this it can be seen that the rate of dissipation of energy is highest for the bottom solder bond. Since a significant reduction in DOF can be achieved by reducing the calculation area for viscoplastic deformation, only the solder bond on the front surface of the middle cell is considered for all subsequent simulations.

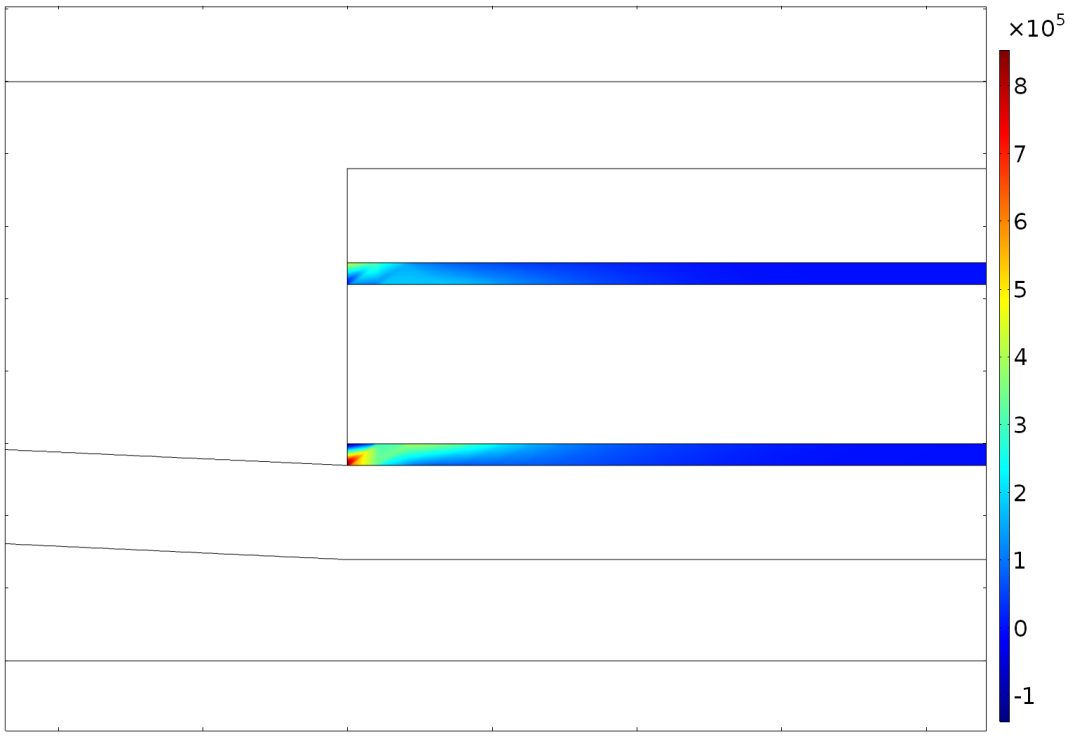

Figure 58: Rate of accumulation of energy dissipation density (W/m^3) for the solder bonds on the middle cell at the onset of the high temperature dwell during a thermal cycle

Figure 59 demonstrates energy dissipation density on the solder bond during one standard thermal cycle. It can be seen that with increasing stress during the ramping periods, damage accumulation increases nearly exponentially. This is characteristic of the behaviour of the solder and explained by the hyperbolic sine term in Anand's model. Additionally, it can be seen that the greatest accumulation damage occurs during the ramp up to higher temperatures. The solders sensitivity to high temperatures is the reason for the large difference. This behaviour is demonstrated further in Figure 60 where creep strain rate is shown to increase hyperbolically with increasing shear stress.

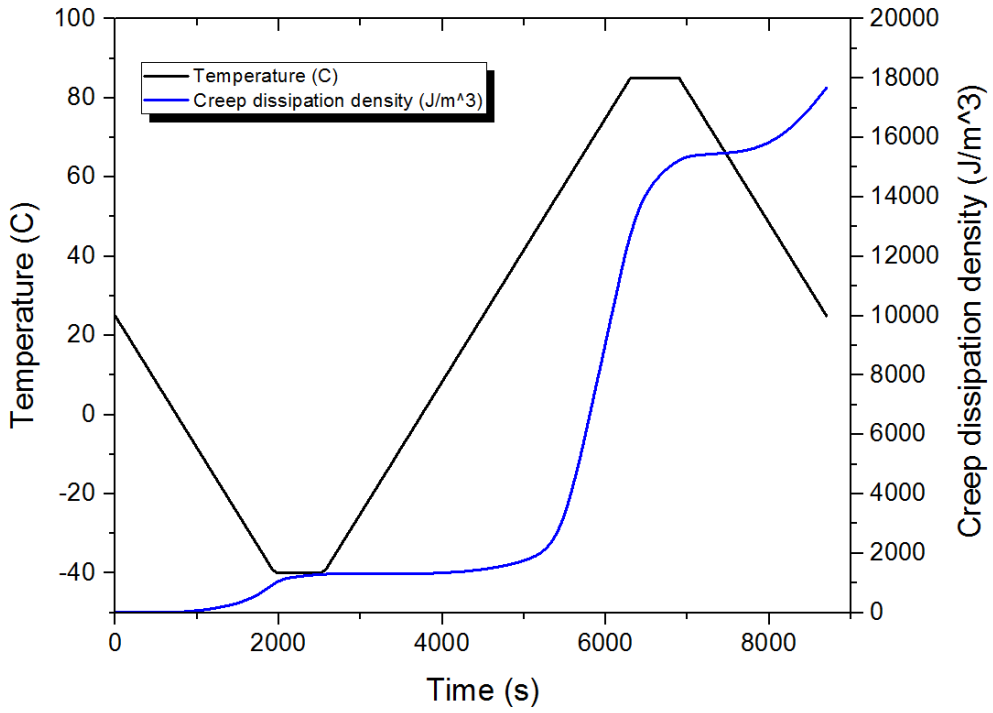

Figure 59: Creep dissipation of the solder during one standard thermal cycle

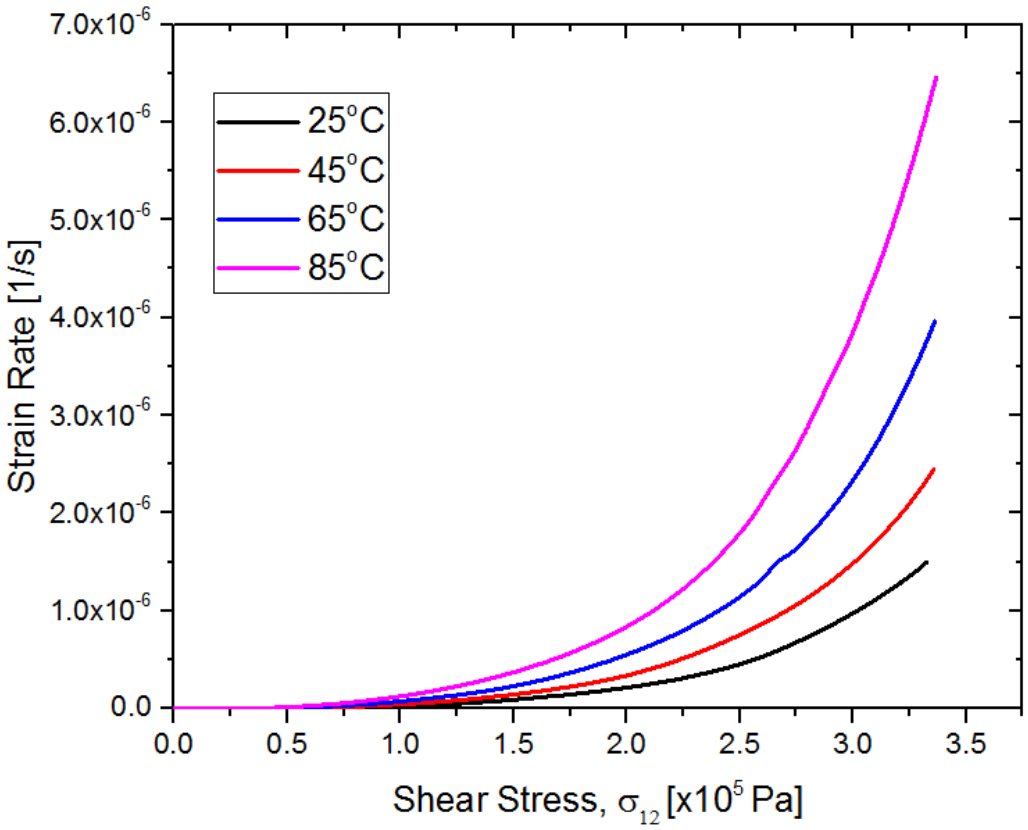

Figure 60: Shear stress vs creep strain rate of solder for different temperatures, demonstrating tthe solders sensitivity to temperature and the hyperbolic nature of strain response

Climate-specific Degradation

The accumulation of inelastic strain energy density on the solder bond is calculated for module temperatures modelled for one year in the climates presented in chapter 4. Figure 61 presents the results from the simulations. The starting point for each climate is at the beginning of the calendar year. It can be seen that the climates which cause higher module temperatures, are also responsible for the highest accumulation of damage on the solder bonds, which is quite unsurprising. However there exists a disparity between the Hot and Dry climates, SOV and GOB, and the Hot and Humid climates, DAR and MAN. The reasons for this disparity will be discussed in the next sub-section. Whilst the hotter climates are in rough agreement with each other, it can

be seen that the temperate climates and warm and humid climates exhibit large differences in damage accumulation. E13 is found to have the highest damage accumulation amongst these and comes under the temperate classification, whereas the next climate in terms of damage is CNR, a warm and humid climate. Following this we have the next temperate climate, CAR, which is unexpectedly met with a similar accumulation of damage from the Cold climate, REG. The climate with the least accumulation of damage by a fairly significant margin is CAB, a Warm and Humid climate.

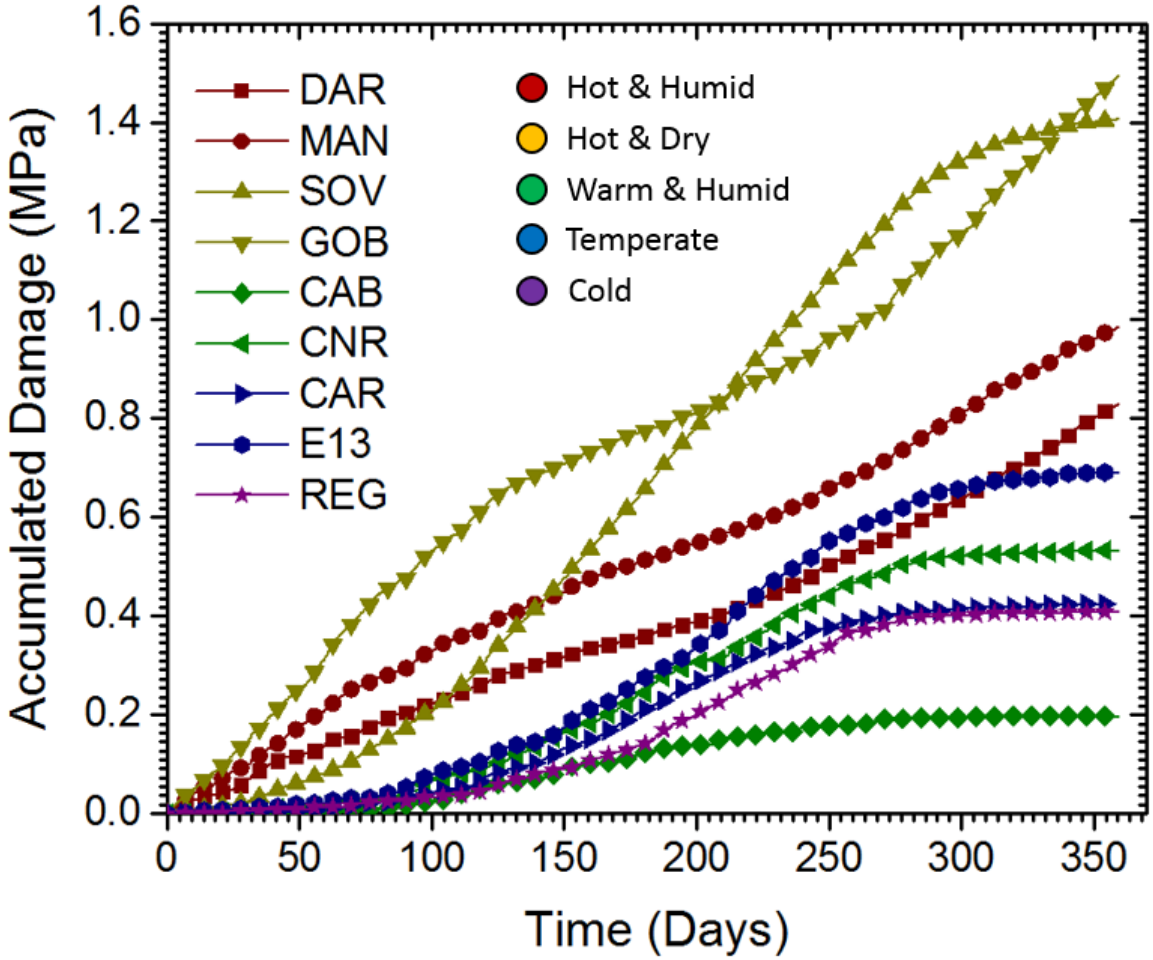

Figure 61: Accumulated inelastic strain energy density (damage) for one year in each location

Whilst CAB and REG both demonstrate a similar rate of accumulation of damage during the first 150 days, REG then accelerates dramatically as it enters the summer

months. During these months it experiences much higher temperatures than CAB, which experiences only mild summers.

It is clear that the classification system used is lacking an important indicator which would categorise these locations more appropriately for solder bond damage potential. The analysis conducted in chapter 5 is referred to in order to determine which properties of the thermal profiles could be most relevant to damage accumulation.

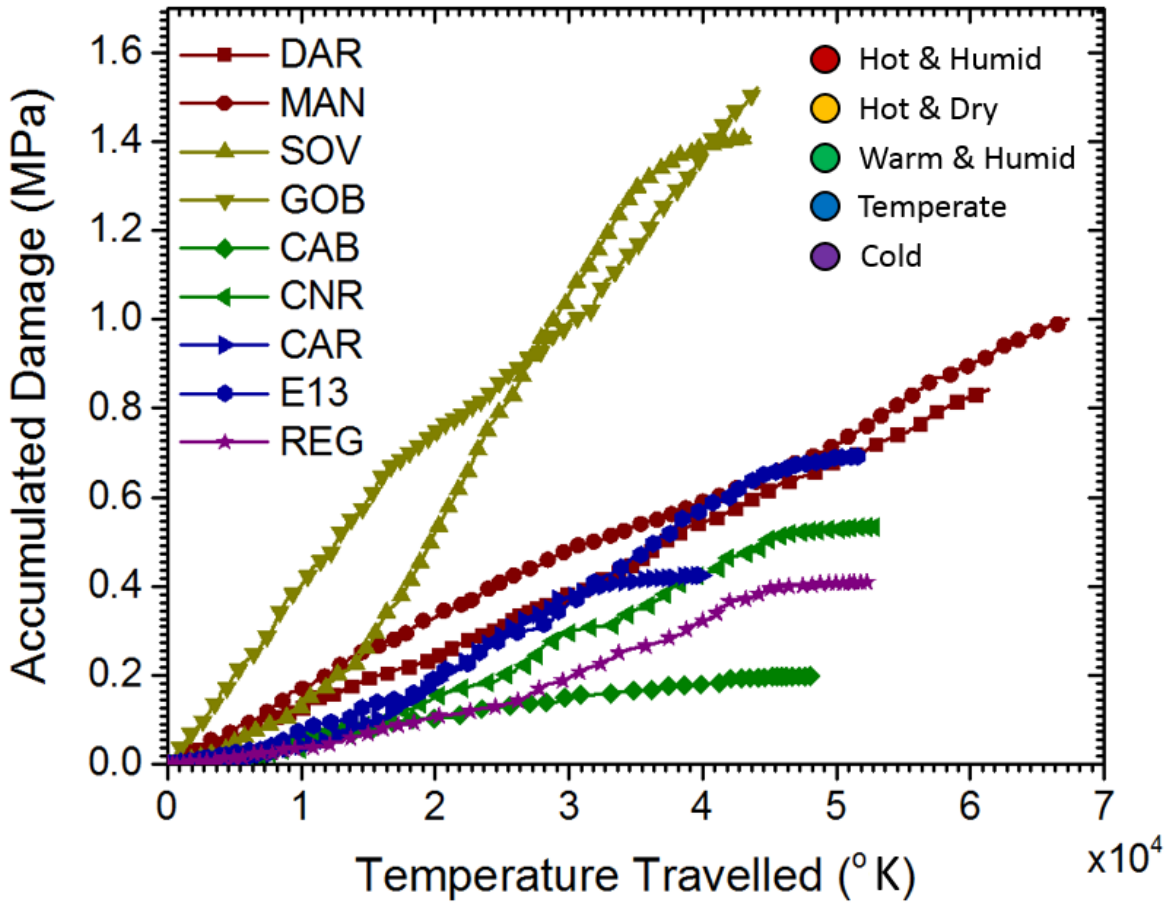

Figure 62: Accumulated damage per degree of temperature travelled

Total temperature travelled has been proposed as a means of classifying climates in terms of their potential for thermomechanical damage. Damage accumulation per degree of temperature travelled is presented in Figure 62. It is clear that the rate of

accumulated damage per degree is not equivalent across all climates and that the damage accumulated per degree is influenced by the variability in other properties of the thermal profile such as absolute temperature, rate of change of temperature and temperature fluctuation frequency. Such properties are therefore examined in order to identify any possible correlations between them and accumulated damage.

Table VIII: Summary of thermal profiles characteristics and total accumulated solder bond damage for one year in each location

Location	Accumulated Damage (Pa)	Mean Daily Max. Module Temperature (°C)	Total Ramping Events	Mean Daily Max. Ramping Event Size (K)
GOB	1520830	61.57	2111	46.48
SOV	1410173	63.77	3052	41.9
MAN	1003800	63.13	7927	36.5
DAR	849194	60.98	7220	33.3
E13	694768	46.8	5709	34.57
CNR	529819	45.09	6102	32.2
CAR	424794	44.05	3865	32.25
REG	409204	34.44	5812	31.5
CAB	197878	35.9	6372	23.6

Each site is summarised in Table VIII in terms of the total accumulated solder bond damage for one year, alongside the mean daily maximum module temperature, total number of ramping events and the mean daily maximum module temperature change. It can be seen that for the two locations which exhibit the highest mean daily maximum module temperatures, SOV and MAN, there is a difference in accumulated damage of approximately 40%. Interestingly, SOV experiences significantly fewer total ramping events than MAN, but does have a higher mean daily maximum ramping event size by 4.58°C, which might suggest that the larger ramping event sizes is what accounts for the increased damage. For the two locations which follow in terms of mean daily maximum module temperature, GOB and DAR, there is a significant

disparity in the accumulated damage over one year with a difference of nearly 80%. While GOB does exhibit a slightly higher mean daily maximum module temperature of 0.59°C, it experiences far fewer total ramping events. The stand-out difference between these two locations is in the mean daily maximum ramping event size, which sees a difference of more than 13.2K, again adding credence to the idea that climates with larger ramping events result in a higher accumulation of damage as opposed to locations with more temperature fluctuations. Three locations, CNR, CAR and REG, have very similar mean daily maximum ramping event sizes. Amongst them, CNR has the highest accumulated damage which is likely attributable to the higher mean daily maximum module temperature and total number of ramping events. The location with the lowest accumulated damage of the three, REG, has a significantly lower mean daily maximum module temperature by 10°C and also has the lowest mean daily maximum ramping event size. The location with the lowest accumulated damage of all sites, CAB, also has the lowest mean daily maximum event size by a wide margin. While the accumulation of solder bond damage is attributable to a combination of the 3 thermal profile properties outlined in Table VIII, it seems that the mean daily maximum ramping event size has a significant influence and could be a strong indicator for damage potential. A strong correlation is observed in Figure 63 between the accumulated damage and mean maximum ramping event size for each location over one year.

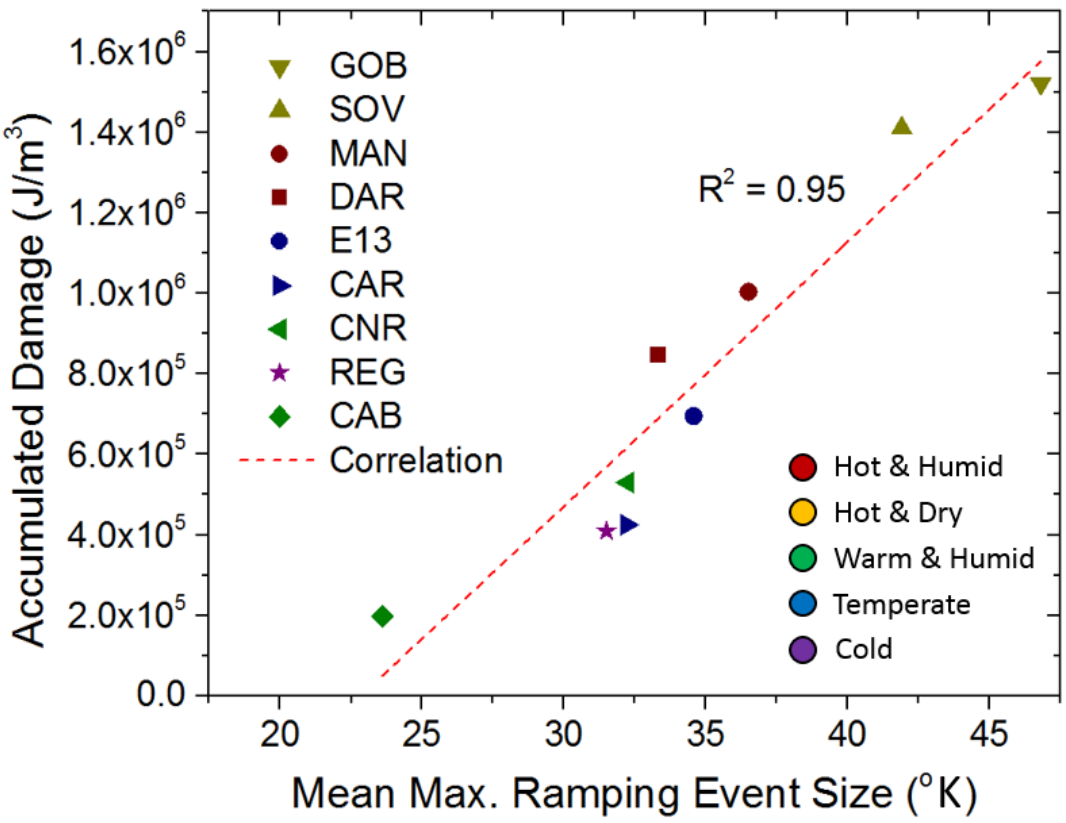

Figure 63: Accumulated damage for one year vs mean maximum ramping event size

While the accumulation of solder bond damage is attributable to a combination of the 3 thermal profile properties outlined in Table VIII, it seems that the mean daily maximum ramping event size has a significant influence and could be a strong indicator for damage potential.

The relevance of the IEC61215 standard tests to long-term degradation and lifetime prediction has been one of the core questions in this thesis. In the previous sub-section it was found that solder bond damage accumulation for 200 thermal cycles was 3.5MJ/m^3. Applying this information to determine the number of thermal cycles required to generate the same amount of damage yields the results presented in Table IX.

Table IX: Number of thermal cycles which would equate to one year of accumulated solder bond damage for one year in each location

Location	Yearly Equivalent Thermal Cycles
GOB	86
SOV	80
MAN	57
DAR	48
E13	39
CNR	30
CAR	24
REG	23
CAB	11

Using this information, a manufacturer could potentially infer potential lifetime of solder bonds within their modules following failure of the bonds caused by the thermal cycling tests. It is important to note here that the results yielded in these simulations are specific to the materials and construction of the particular module, and that simulations should be carried out to understand the impact of changing certain material properties. An exploration of the impact of different materials has been conducted in chapter 7.

6.5 Conclusions

The thermomechanical behaviour of PV mini modules has been simulated using FEM techniques, with a particular focus on the degradation of solder bonds in specific use-environments. It has been shown that hot and dry environments such as those found in Namibia (GOB) and Saudi Arabia (SOV) are most detrimental to the solder bonds. This is then followed by the hot and humid environments like Darwin, Australia and Papua New Guinea. Beyond this, there was no correlation to be found between solder bond damage and climate-type as defined by the classification system used in this work, with disparities in damage shown for the temperate, cold and warm and humid

climates. Whilst mean maximum module temperature and total number of ramping events does play a role in the accumulation of solder bond damage, a strong correlation was found between accumulated damage and the mean daily maximum ramping event size. This lends credence to the IEC61215 thermal cycling profile to accelerate damage, which uses large ramps (of 125K).

In addition, by simulating the accumulated damage during accelerated testing, it was shown how it might be possible to use the current type-approval tests for determining long-term degradation of solder bonds in the outdoors by comparing the accumulated inelastic strain energy density in each scenario. However, there are certain caveats to this in that the simulations do not take into account other mechanisms and changes in material properties over time. For example, changes in the mechanical properties of the backsheet or encapsulant are not accounted for and are likely to degrade differently depending on the environment.

Chapter 7

Influence of Viscoelastic Properties of Encapsulants on Solder Degradation

7.1 Introduction

In the previous chapter, the influence that different operating environments had on the thermomechanical degradation of solder bonds was demonstrated. However, operating environments are not the only variable to consider. The component materials in a device may have a significant influence on thermomechanical behaviour of a module and the potential for solder bond degradation. Encapsulation materials demonstrate complex mechanical behaviours, with a dependence on both temperature and time, attributable to their viscoelastic properties. Given the variability of module operating temperature profiles experienced by modules in various climates, as demonstrated in chapter 5, the influence of the mechanical behaviour of the encapsulant becomes a crucial factor. Different encapsulants may provide varying degrees of mechanical stability, depending on temperature, which may influence the strains imposed on solder bonds in different environments. For this reason, the mechanical behaviour of multiple encapsulants is modelled and the performance, in terms of solder degradation potential, is evaluated for different climatic conditions.

7.2 Modelling Viscoelastic Behaviour of Various Encapsulants

Five different materials are examined which are currently used or have been used at some time as a module encapsulant in the market. Each material has been characterised and modelled according to the Generalized Maxwell model described in chapter 4.

Encapsulant Materials

Ethylene Vinyl-Acetate (EVA)

Two types of EVA are examined, hereby referred to as EVA-1 and EVA-2. Each one is produced by the same manufacturer with different specifications. EVA-1 is referred to as a fast-cure material, whilst EVA-2 is referred to as an ultra-fast-cure material. As can be inferred from the names, the recommended lamination times are different where EVA-1 is recommended for 15 minutes and EVA-2 for 12 minutes. Both types have recommended lamination temperatures between 145 and 150°C. Whilst each laminate is EVA-based, it can be assumed that the chemical makeups are somewhat different in order to facilitate the change in lamination time. Studying both types of EVA provides some insight into the effect that different formulations and additives have on viscoelastic response.

Polyolefin (PL)

The third encapsulant being studied is a cross-linkable polyolefin (PL). Whilst EVA is also a polyolefin, this material is marketed as an EVA-free encapsulant which exhibits PID-resistant properties.

Polyvinyl Butaryl (PVB)

Polyvinyl butaryl (PVB) is the fourth encapsulant under examination. PVB is an older material which is used more often in thin-film and building-integrated devices. It is

the only non-crosslinkable material being studied (although cross-linkable variants are available) and as such it is expected that, particularly at higher temperatures, it will demonstrate the greatest level of instability. PVB is typically recommended for glass/glass module configurations.

Ionomer

The final encapsulant is Ionomer-based. Ionomers have only recently been developed and used for PV packaging, and are typically suggested more for thin-film devices.

In addition to the complex modulus of each material which is determined analytically, the coefficient of thermal expansion and density are required. Each of these are obtained from the datasheets provided by the manufacturer and summarised in Table X.

Table X: Material properties for each encapsulant

Material	Density (kg/m^3)	Coefficient of Thermal Expansion ($1e^{-4}/K$)
EVA-1	960	2.70
EVA-2	960	2.70
Ionomer	1070	2.81
PL	880	3
PVB	1060	1.7

Rheometer

A TA Instruments Dynamic Hybrid Rheometer – 2 (Figure 64) is used to conduct the measurements. The rheometer applies a rotational force to the samples and measures the resulting angular displacement, or strain, with which it is possible to calculate the elastic modulus and viscosity. Sheets of each encapsulant are cured according to the optimum specifications outlined by the manufacturer. Samples with 8mm diameter and 0.6mm thickness are loaded onto the rheometer. A peltier plate is used to control

the sample temperature and a parallel plate geometry of 8mm diameter applies the oscillatory force. An image of the rheometer can be seen in Figure 64.

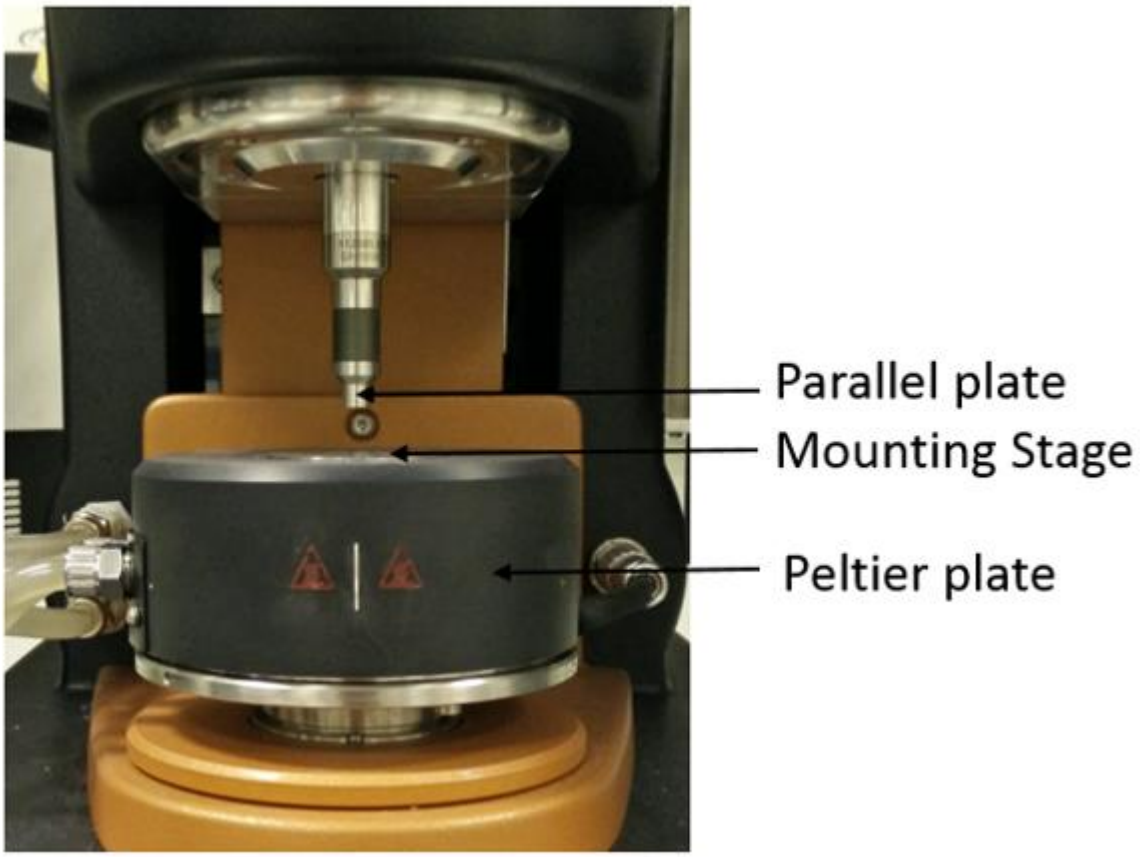

Figure 64: Image of the TA Instruments Hybrid Dynamic Rheometer with peltier plate configuration

Linear Viscoelastic Region

When subjected to large strains, a viscoelastic materials behaviour becomes non-linear, and the aforementioned constitutive equations no longer apply. To accurately evaluate the viscoelastic behaviour it is therefore important that measurements are conducted using deformations within the linear viscoelastic region (LVR). Determination of the LVR is achieved by sweeping the strain rate and monitoring the storage modulus. When the material breaks down a sudden and rapid decrease in storage modulus can be observed indicating that that material is no longer within the LVR. Figure 65 presents storage modulus measurements for a strain rate sweep from

0% to 2% at constant temperature of -40°C. The narrowest LVR can be expected at the lower temperatures as the material is more brittle and more susceptible to permanent deformation at those temperatures. It can be seen that both EVA's and PL exhibit similar LVR's with non-linear behaviour occurring at around 0.3%. The Ionomer has a narrower range, exiting the LVR at around 0.05% and PVB narrower still at 0.04%. For the remaining measurements, the applied strain rate is set to these values such that the linear response is maintained.

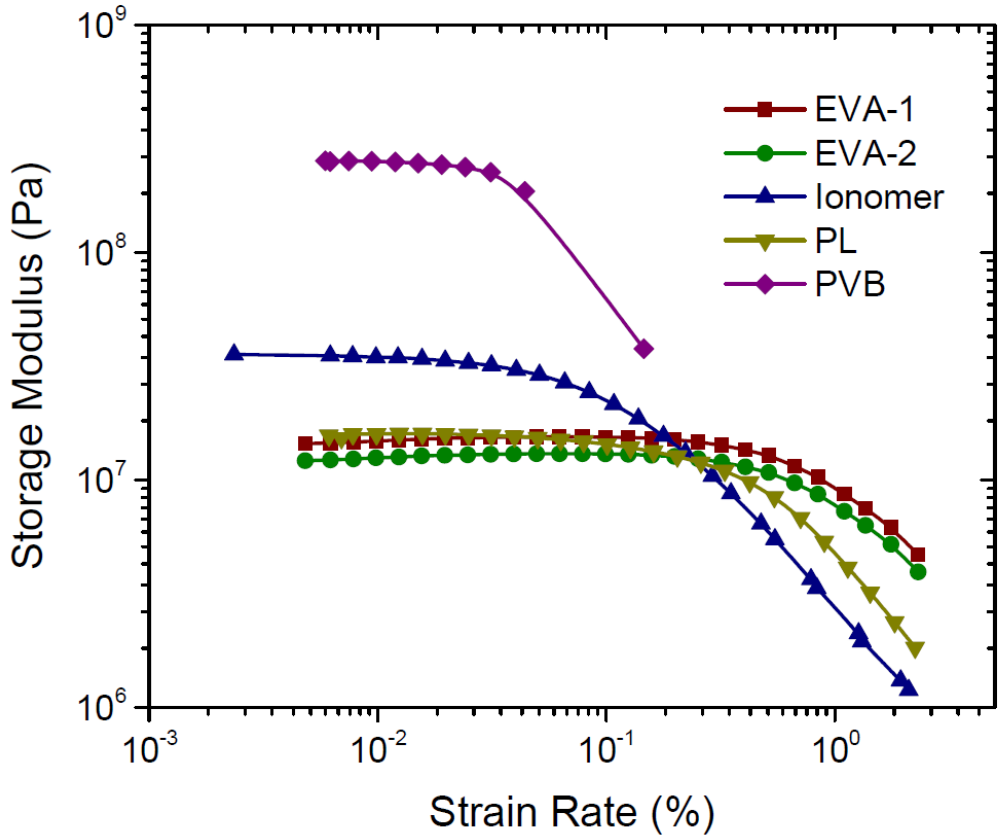

Figure 65: Storage modulus measurements for a strain rate sweep between 0 and 2% for each encapsulant at constant temperature of -40°C

Temperature-Dependent Behaviour

For an initial indication of the mechanical behaviour of each encapsulant, observations of the temperature-dependency between -40°C and 100°C are made. Storage modulus measurements are conducted with a 1Hz oscillation with a temperature ramp rate of

5K/min. Figure 66 presents the results for each encapsulant. The encapsulants demonstrate varying degrees of dependency on temperature. It can be seen that PVB demonstrates the most significant change in storage modulus with increasing temperature with the most dramatic change occurring at around 0°C with a storage modulus decrease of $1x10^2$ Pa. Such a significant change is likely a result of the non-crosslinked nature of the material which, as previously noted, reduces the materials ability to retain its elasticity at elevated temperatures. Both EVA materials demonstrate very similar behaviour with a relatively rapid decrease in storage modulus as the material passes through the glass transition (-40 to -10°C), reaching the rubbery plateau between -10 and 40°C and once again gradually declining with the partial melting of the copolymer. The PL exhibits similar transitions within the same temperature regions as the EVA although with slightly less severity, maintaining a higher storage modulus throughout. Whilst the ionomer has the lowest storage modulus at -40°C, it demonstrates the greatest stability of all the encapsulants undergoing relatively little change across the entire temperature range. The ability of the ionomer to retain its elasticity, particularly at temperatures above 40°C, could suggest that the ionomer would provide most stability to the cells and interconnects, reducing displacement of the cells and therefore the strain imposed on solder bonds.

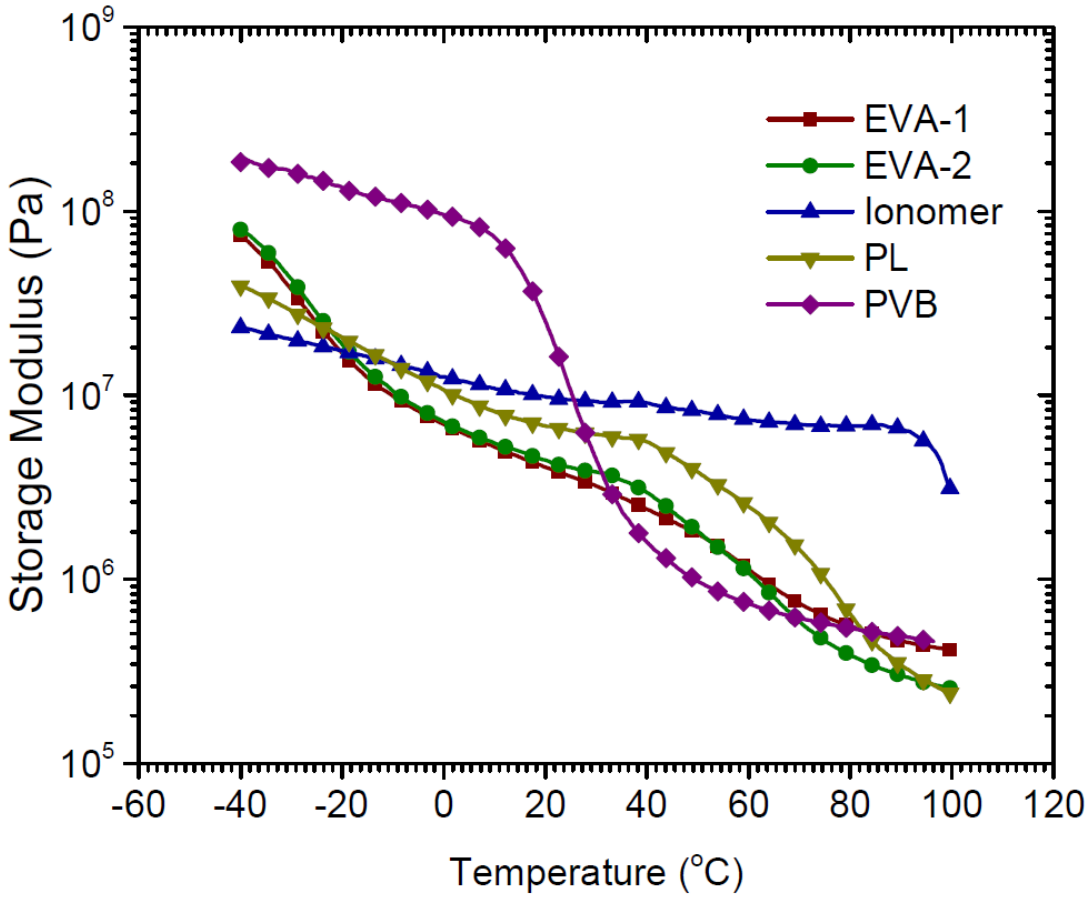

Figure 66: Temperature-dependent storage modulus for each encapsulant measured with an oscillation frequency of 1Hz

Determining Maxwell Element Parameters

Identifying the number of Maxwell elements and the appropriate parameter values is required to capture viscoelastic behaviour using the Generalised Maxwell model as previously described. This information can be determined by fitting the model to storage modulus measurements for the material being modelled. However, in order to obtain sufficient appropriate values, it is necessary to fit the model to modulus data for a wide range of oscillation frequencies (typically in the range 10^{-12} to 10^{12} Hz). It goes without saying that such data cannot be measured practically and so another approach is utilised.

For viscoelastic materials, storage modulus is a function of temperature at constant time and, correspondingly, a function of time at a constant temperature. This relationship is known as Time-Temperature Superposition (TTSP). The principles have been well established by Williams, Landel and Ferry (WLF) [101] .By measuring the storage modulus over a given period at different isotherms, it is possible to shift the isotherm curves horizontally, in the frequency-domain, such that a much larger and continuous curve, known as a "mastercurve", can be produced. The WLF equation (7) is used to determine the shift-factor, α_τ, at a given temperature.

$$Log(\alpha_t) = \frac{-C_1(T-T_g)}{C_2+(T-T_g)} \quad (7)$$

Where C_1 and C_2 are material dependent parameters and T_g is a reference temperature (typically glass transition temperature).

Isothermal measurements of storage modulus are conducted for each material over frequencies 0.1 – 10 Hz at temperatures -40 to 150°C in steps of 10K. The results are presented in Figure 67.

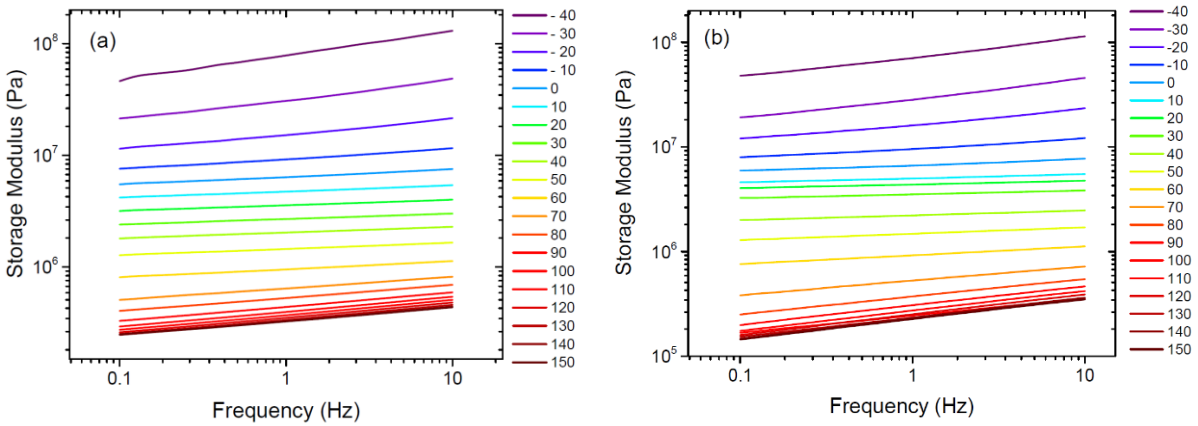

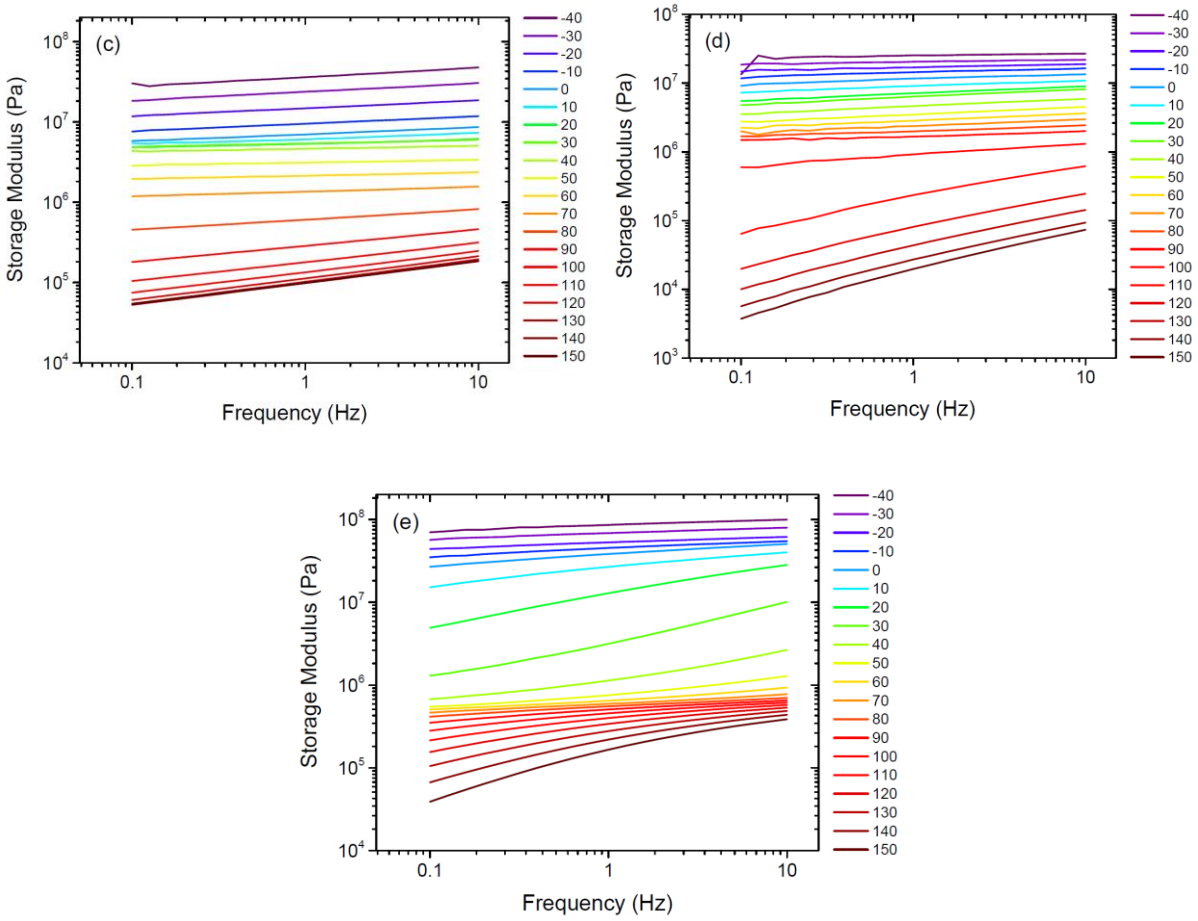

Figure 67: Isothermal storage measurements for (a) EVA-1, (b) EVA-2, (c) PL, (d) Ionomer, (e) PVB

The EVA's both show similar isotherms with an increasing storage modulus with decreasing temperature and significant increases around the glass transition region (-10 to -30°C). With increasing temperature, a decreasing storage modulus is observed until partial melt occurs at around 90°C. The PL demonstrates similar behaviour to the EVA, with a less dramatic increase in storage modulus at the lower temperatures and a more significant decrease at higher temperatures. As expected, the ionomer demonstrates only small decreases in storage modulus as the temperature is increased, until 100°C where a large decrease is observed. Interestingly, the effect of frequency also becomes more significant at the higher temperatures. Whilst most of the materials demonstrate the greatest stability in the range of 10 to 50°C, PVB shows least stability undergoing a large shift in storage modulus in this range.

Mastercurves are generated from the isotherms using the WLF relationship as shown in Figure 68. A reference temperature of 20°C is used while the shift coefficients C_1 and C_2 for each material are shown in Table XI. The mastercurves for the EVAs, Ionomer and PL share similar trends with a gradually increasing storage modulus with frequency. Both EVAs show very similar mastercurves with some deviation with the range of 10^{-2} to 10^{1} rads/s and a larger deviation occurring at the low frequencies. The PL again shows a similar mastercurve to the EVA with slightly higher storage modulus, which is anticipated given the isothermal measurements. The Ionomer mastercurve shows a gradually increasing storage with frequency above 10^{-8} rad/s, below which a sharp reduction in storage modulus is present. This reflects the isothermal measurements whereby a rapid decrease in storage modulus occurs above 90°C as the material melts and undergoes a rapid phase change. The PVB shows a distinctly different mastercurve to the other materials with steady increases in storage modules within the range of 10^{-5} to 10^{-2} rads/s and above 10^{3} rad/s. A sharp increase in storage modulus is observed between 10^{-2} and 10^{3} which is a reflection of the phase change observed in the isothermal measurements between 0 and 50°C.

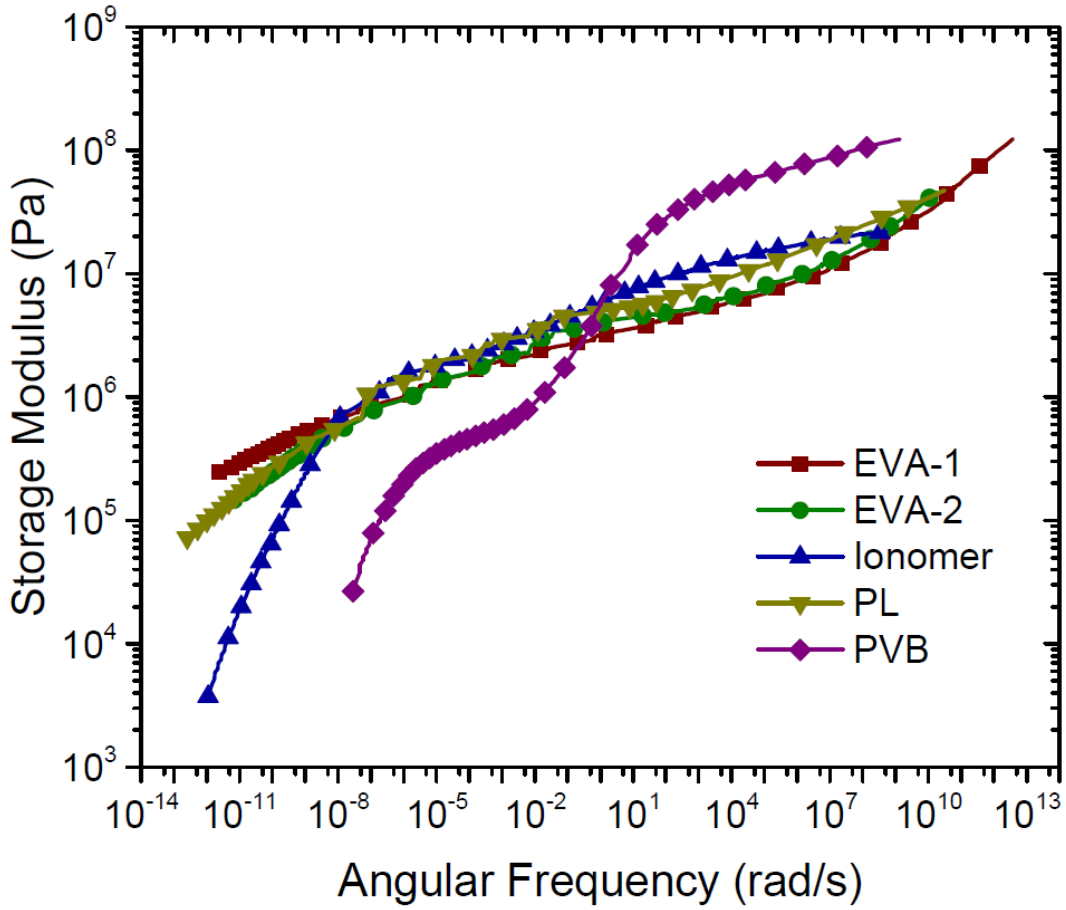

Figure 68: Mastercurves generated from shifting isothermal measurements of each encapsulant

Table XI: WLF shifting coefficients and fit quality for each encapsulant

Encapsulant	C1	C2 (K)	R^2
EVA-1	41.32	242.12	0.98
EVA-2	38.22	238.06	0.97
Ionomer	69.17	606.69	0.99
PL	58.61	382.22	0.98
PVB	22.57	242.69	0.99

Finally, a polynomial least-squared fitting algorithm is used to fit the Generalised Maxwell equation to each materials mastercurve such that Maxwell element parameter values, G_k and τ_k, can be determined. In finite-element simulations using

the Generalised Maxwell model, the computational demands increase with increasing number of Maxwell elements. Therefore, the best fit using the least number of elements is considered when fitting to the mastercurves. The relaxation time,τ_k, and relaxation strength, G_k, for the Maxwell branches determined for each material are outlined in Table XII.

Table XII: Maxwell Branch Parameters for each material

EVA-1		EVA-2		Ionomer		PL		PVB	
τ_k (s)	G_k (MPa)	τ_k (s)	G_k (MPa)	τ_k (s)	G_k (MPa)	τ_k (s)	G_k (MPa)	τ_k (s)	G_k (MPa)
$2.6e^{-14}$	41.80	$3.2e^{-12}$	25.70	$3.1e^{-10}$	1.335	$6.9e^{-12}$	4.95	$7.4e^{-11}$	7.67
$2.5e^{-13}$	30.22	$2.4e^{-11}$	14.90	$2.1e^{-9}$	1.143	$6.0e^{-11}$	3.72	$3.7e^{-10}$	7.62
$2.3e^{-12}$	17.31	$1.8e^{-10}$	8.62	$1.4e^{-8}$	1.224	$5.2e^{-10}$	2.80	$1.8e^{-9}$	7.55
$2.2e^{-11}$	9.75	$1.3e^{-9}$	5.04	$9.6e^{-8}$	1.012	$4.5e^{-9}$	2.14	$9.0e^{-9}$	7.35
$2.0e^{-10}$	5.17	$1.0e^{-8}$	2.99	$6.5e^{-7}$	1.268	$3.9e^{-8}$	1.65	$4.5e^{-8}$	6.75
$1.9e^{-9}$	3.35	$7.4e^{-8}$	1.81	$4.4e^{-6}$	0.939	$3.4e^{-7}$	1.30	$2.2e^{-7}$	6.07
$1.8e^{-8}$	1.81	$5.6e^{-7}$	1.12	$3.0e^{-5}$	1.146	$2.9e^{-6}$	1.02	$1.1e^{-6}$	5.48
$1.7e^{-7}$	1.19	$4.2e^{-6}$	0.72	$2.0e^{-4}$	0.988	$2.5e^{-5}$	0.81	$5.4e^{-6}$	4.79
$1.6e^{-6}$	0.72	$3.1e^{-5}$	0.49	$1.4e^{-3}$	1.032	$2.2e^{-4}$	0.65	$2.7e^{-5}$	4.55
$1.5e^{-5}$	0.52	$2.3e^{-4}$	0.35	$9.3e^{-3}$	0.838	$1.9e^{-3}$	0.52	$1.3e^{-4}$	4.81
$1.4e^{-4}$	0.38	$1.7e^{-3}$	0.27	$6.3e^{-2}$	0.819	$1.6e^{-2}$	0.42	$6.6e^{-4}$	5.16
$1.3e^{-3}$	0.30	$1.3e^{-2}$	0.22	$4.3e^{-1}$	0.747	$1.4e^{-1}$	0.36	$3.3e^{-3}$	5.70
$1.2e^{-2}$	0.24	$9.7e^{-2}$	0.19	2.9	0.603	1.2	0.30	$1.6e^{-2}$	6.28
$1.1e^{-1}$	0.20	$7.2e^{-1}$	0.17	$2.0e^{1}$	0.497	1.1	0.25	$8.0e^{-2}$	5.89
1	0.17	5.4	0.16	$1.3e^{2}$	0.401	9.2	0.19	$4.0e^{-1}$	4.10
9.7	0.14	4.0e	0.14	$9.0e^{2}$	0.303	$8.0e^{2}$	0.15	2.0	2.03
$9.1e^{1}$	0.13	$3.0e^{2}$	0.13	$6.1e^{3}$	0.220	$6.9e^{3}$	0.12	9.8	0.82
$8.5e^{2}$	0.11	$2.3e^{3}$	0.11	$4.1e^{4}$	0.177	$6.0e^{4}$	0.10	$4.8e^{1}$	0.31
$8.0e^{3}$	0.11	$1.7e^{4}$	0.10	$2.8e^{5}$	0.102	$5.2e^{5}$	0.10	$2.4e^{2}$	0.12
$7.5e^{4}$	0.08	$1.3e^{5}$	0.09	$1.9e^{6}$	0.078	$4.5e^{6}$	0.10	$1.2e^{3}$	0.06
$7.0e^{5}$	0.09	$9.4e^{5}$	0.08	$1.3e^{7}$	0.042	$3.9e^{7}$	0.10	$5.9e^{3}$	0.04
$6.5e^{6}$	0.06	$7.0e^{6}$	0.07	$8.6e^{7}$	0.204	$3.4e^{8}$	0.09	$2.9e^{4}$	0.05
$6.1e^{7}$	0.09	$5.2e^{7}$	0.06	$5.8e^{8}$	0.084	$2.9e^{9}$	0.08	$1.4e^{5}$	0.06
$5.7e^{8}$	0.07	$3.9e^{8}$	0.05	$4.0e^{9}$	0.151	$2.5e^{10}$	0.06	$7.2e^{5}$	0.07
$5.3e^{9}$	0.06	$2.9e^{9}$	0.04	$2.7e^{10}$	0.036	$2.2e^{11}$	0.04	$3.6e^{6}$	0.06
$5.0e^{10}$	0.04	$2.2e^{10}$	0.03	$1.8e^{11}$	0.018	$1.9e^{12}$	0.02	$1.8e^{7}$	0.03
$4.7e^{11}$	0.03	$1.6e^{11}$	0.02	$1.2e^{12}$	0.006	$1.6e^{13}$	0.01	$8.7e^{7}$	0.01
$4.4e^{12}$	0.02	$1.2e^{12}$	0.01	$8.3e^{12}$	0.002	$1.4e^{14}$	0.01	$4.3e^{8}$	0.004

Verifying Viscoelastic Modelling

Stress relaxation is characteristic of viscoelastic behaviour. Following the application of a step deformation, the stress (or force) necessary to maintain the deformation decays with time. The stress relaxation behaviour of the materials is used to validate the viscoelastic model parameters. Using the rheometer, a step deformation is applied to cured 8mm diameter samples of each material with an application time of 0.01 s at constant temperatures of -20, 0, 40 and 80°C. The resulting stress is measured over a period of 10 minutes. The same experiment is then modelled in COMSOL Multiphysics using the input parameters of each material for the Generalised Maxwell model.

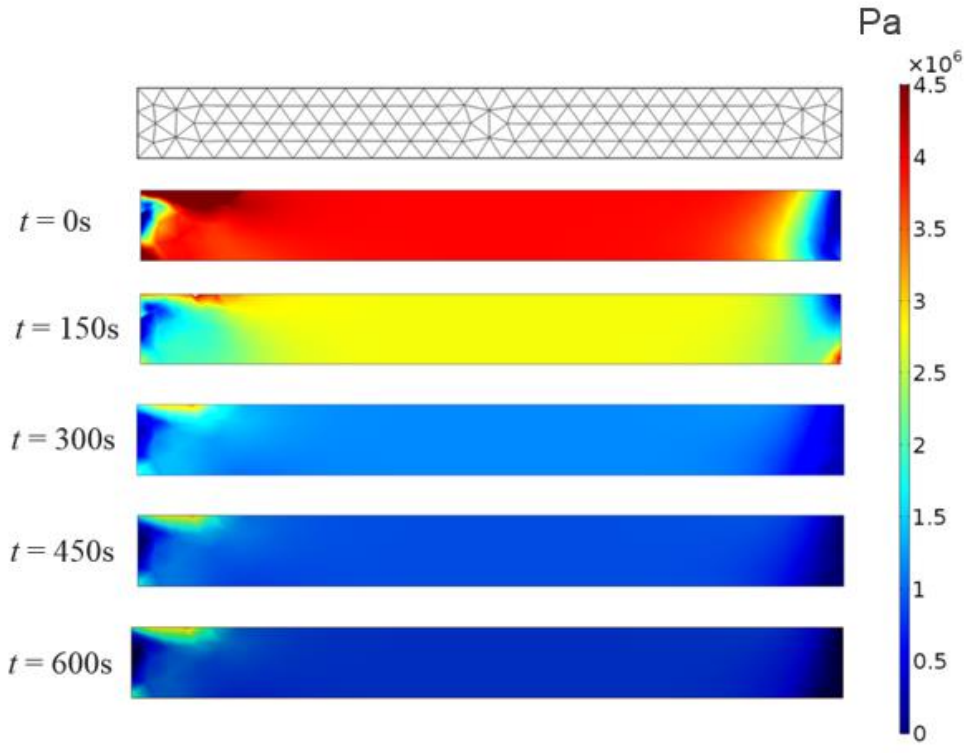

Figure 69: Cross-sectional view of the simulation of EVA-1 stress relaxation experiment at multiple time points at 0°C

Figure 70 compares the measurements from both experiment and simulation for EVA-1. The stress relaxation behaviour is captured quite well in the simulation using the

Maxwell terms which were previously determined. As expected, stress relaxation is greater with increasing temperature as the elastic modulus decreases. Interestingly, stress relaxation at -20°C is also significant. The reason for this is as the material approaches the glass transition, despite having a much higher storage modulus, the loss modulus is also high as the frictional forces associated with movement between polymer chains result in an increased energy dissipation through heat loss. A good agreement between experimental and simulation data is achieved for all materials and temperatures, where the ionomer at -40°C was found to have the worst agreement with a root mean biased error of 0.07.

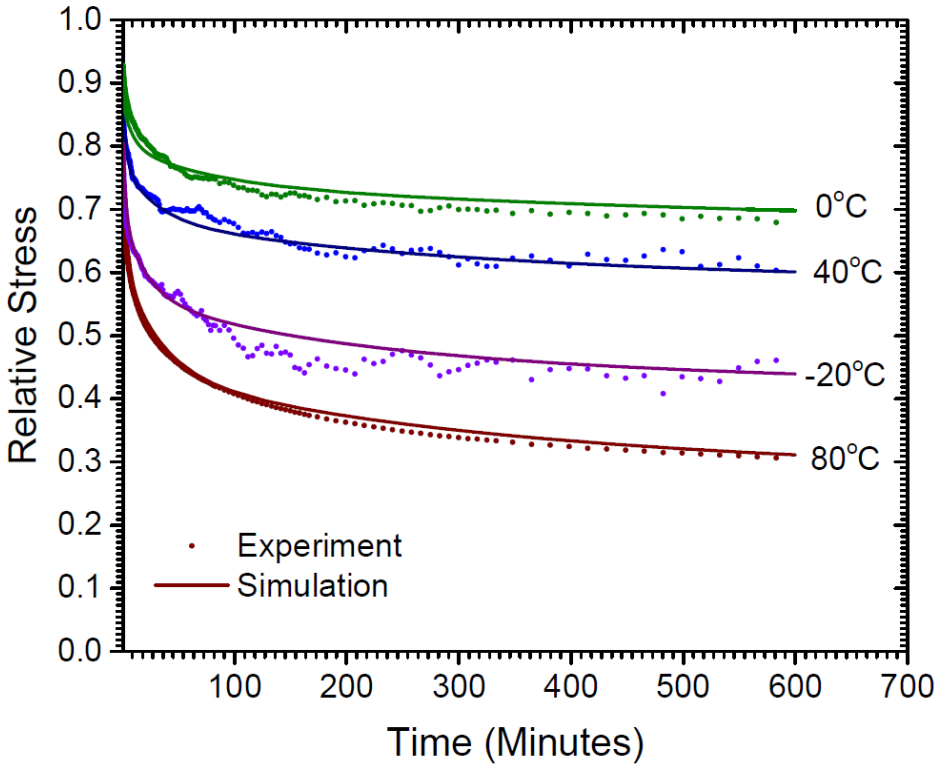

Figure 70: Stress relaxation experiment vs simulation for EVA-1 at different temperatures

7.3 Influence of the encapsulant behaviour

The 2D finite-element model which has previously been described in chapter 6 is used here to compare the influence that the viscoelastic properties of the encapsulant has on the thermomechanical strains and subsequent degradation of the solder bonds.

Thermal Cycling 200

The first simulation is made following the thermal cycling regime outlined by IEC61215. The energy dissipation density of the solder bonds for each encapsulant following the TC200 thermal profile is presented in Figure 71. At the low temperature dwell (around 2500 s), both EVA encapsulants appear to have no discernible difference, sharing the highest amount of dissipated energy. The ionomer exhibits the lowest amount of dissipated energy. A total change in temperature of 125K occurs during the ramp up from the low temperature dwell to the high temperature dwell. This has a significant effect on the inelastic deformation of the solder bond, and is the period in which the majority of deformation and damage occurs. Whilst the melting point of the solder alloy is not reached, higher temperatures increase the rate of creep and viscoplastic deformation. At the high temperature dwell (8000 s), EVA-2 appears to have accumulated the most damage whilst the ionomer has accumulated far less than the other encapsulants, with approximately 12% less energy dissipation than the next encapsulant, PL. Both PL and PVB appear to have dissipated the same amount of energy.

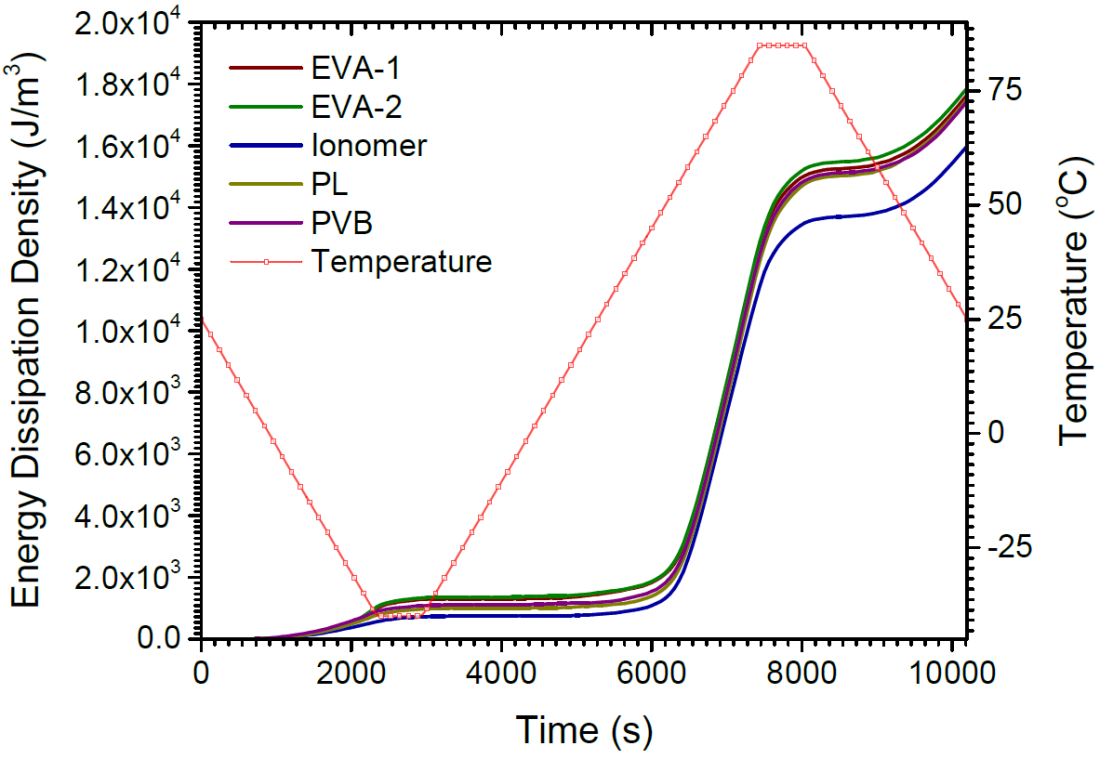

Figure 71: Energy dissipation density following one thermal cycle for each encapsulant

Outdoor Climates

It might be expected that, based on the results of the TC200 simulations, the ionomer would be the best performing encapsulant, with EVA-2 being the worst performing in terms of damage to the solder bonds. However, the thermal profile used for the TC200 tests are not representative of temperature conditions experienced by modules in real environments. Such a rapid increase in temperature over an extended period has not been shown to occur. Given the time-dependent nature of the encapsulants mechanical behaviour, it is important to look at more realistic conditions. Under different rates of temperature change, the encapsulants could behave differently, affecting the viscoplastic deformation potential. For this reason, the energy dissipation density is calculated for two outdoor climate types; temperate and hot and dry. Module temperature data for each location has been taken from the same BSRN data used in chapter 5. For the hot and dry climate, one day is taken at the height of summer

where temperatures are highest and for the temperate climate one day is taken in the winter where temperatures are lowest. As such, the performance of each encapsulant can be evaluated for highest and lowest temperature profiles. Energy dissipation density for the temperate climate is presented Figure 72. In this climate, a maximum temperature change of 18 K occurs over a period of ~4 hours from 0 °C to 18 °C. Both the rate of change of temperature and the absolute temperatures are significantly lower than the TC200 profile. As would be expected, the total energy dissipated is significantly lower. The greatest deformation occurs during the increase in temperature during sunrise. Whilst it appears as though no deformation occurs following peak temperature (50000 s), a slight gradual change does occur, though deformation during cooling at such low temperatures is marginal. Contrary to the results presented in Figure 71, EVA-2 is amongst the lowest in terms of energy dissipated, having dissipated 5.4 % less energy than EVA-1. This would suggest that EVA-2 is more stable within this temperature range. The ionomer continues to be the best performer for this climate, and there is a more significant difference between the other encapsulants. If conclusions were to be drawn based solely on the certification testing procedures, then EVA-2 might be considered the worst encapsulant. However, in the field under realistic operating conditions, it might be that EVA-2 is one of the better performers. In addition to this, despite both EVAs being based on the same material, it would appear that the additives and processing introduced by the manufacturer leads to a marked difference in mechanical behaviour.

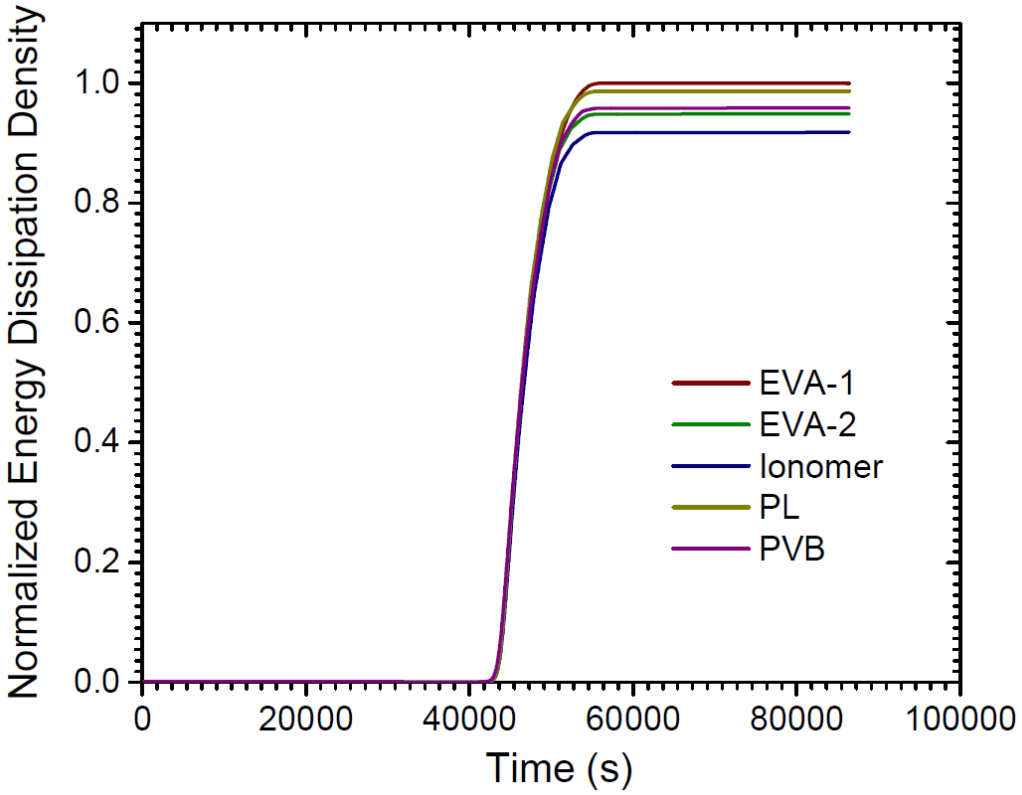

Figure 72: Energy dissipation density through temperature climate data, normalised to the most damaging encapsulant

Energy dissipation density for the hot location is presented in Figure 73. In this case, a total temperature change of 50K occurs over a time period of approximately 6 hours from 18°C to 68°C. The elevated temperature and duration of the temperature rise has resulted in a significantly higher energy dissipation than seen in the cold climate. At the peak temperature (~46000 s) it is found that the PVB results in the greatest amount of energy dissipation. Interestingly, EVA-1 becomes the better performing EVA-based encapsulant for this environment. A similar difference is demonstrated between EVA-1 and PL. The ionomer is once again the encapsulant which causes the least energy dissipation.

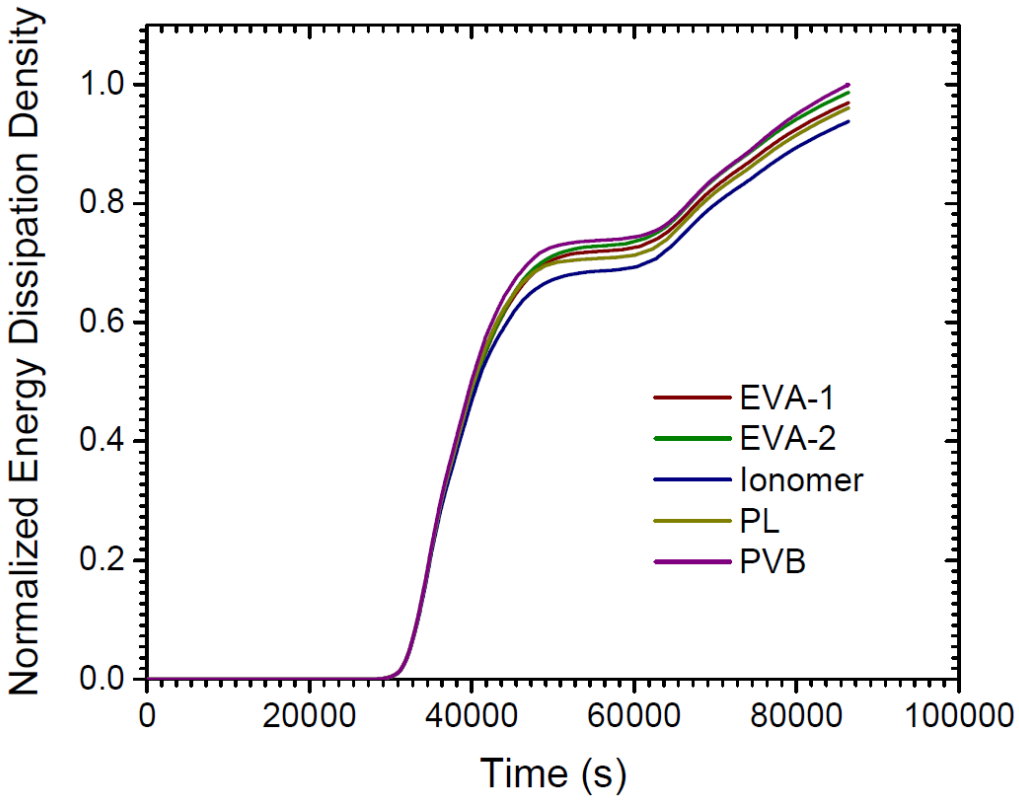

Figure 73: Energy dissipation density through hot and dry climate data, normalised to the most damaging encapsulant

7.4 Conclusions

Degradation of solder bonds within a PV module assembly was evaluated through simulation of the viscoplastic deformation under 3 environmental conditions and quantified through calculation of the energy dissipation density. Module operating temperatures for real outdoor environments, one cold and one hot, were used for the simulations as well as the thermal cycling profile mandated by the IEC61215 certification protocols. The viscoelastic properties of the encapsulation materials has been shown to have a direct influence on the imposed strains (and therefore degradation potential) of the solder bonds. The mechanical behaviour for each encapsulant is dependent on the absolute temperature and the rate of change of temperature, as expected of the viscoelastic properties.

The ionomer-based encapsulant was found be the best performer, with the lowest calculated total energy dissipation under each condition. This is likely due to the higher physical stability demonstrated by the encapsulant, which does not undergo dramatic material phase change with temperature compared with the other encapsulants. The other encapsulation materials have been shown to perform better or worse than each other, depending on the climate. Whilst EVA-2 and PVB outperformed EVA-1 and PL in the colder environment, the opposite was the case for the hot environment. The environment-dependent performance is indicative of the viscoelastic properties of the encapsulants, where the elastic modulus is dependent on the absolute temperature and the rate of strain which is applied during changes in temperature.

In addition to this, the certification testing protocol TC200 suggested that the degradation potential of solder bonds would be highest when EVA-2 was used as the encapsulation material, and lowest when ionomer was used with no discernable difference between the other encapsulants. To draw any conclusions about the ability of an encapsulant to provide mechanical stability based on these tests could be misleading, as the encapsulant may perform better or worse depending on the location of deployment.

Conclusions and Outlook

Thermomechanical stresses and degradation potential for solder bonds within PV modules operating under normal conditions are not well understood. However, they are an important consideration when evaluating the long-term performance and financial viability of systems. Degradation of the structural integrity of solder bonds within a module has a direct effect on series resistance and output power, in addition to catalysing destructive secondary mechanisms such as hot-spots. Whilst so-called accelerated ageing tests are in place to determine a modules susceptibility to solder bond degradation, the information provided by such tests are very limited in that any correlation between the tests and actual outdoor performance are undetermined, if they even exist at all. As such, a meaningful method for quantifying the potential for solder bond degradation in specific environments has not been determined. The thermomechanical behaviour and resulting solder bond degradation within different climates has been simulated using finite element techniques. A quantification of the potential for solder bonds to degrade has been presented as well as identification of the key factors affecting degradation. In addition, an evaluation of the influence of the viscoelastic properties of the encapsulants has been given.

An analysis of the thermal exposure which can be expected from a range of climates has been presented as the first step of this work. Module operating temperatures are shown to vary significantly between climates with the highest module temperatures, unsurprisingly, occurring within the hotter environments. Thermomechanical stress can be attributed to mismatching thermal expansion coefficients between components and as such the changes in temperature become a core focus of the analysis. In terms of overall number of temperature fluctuations, hot and humid environments were

found to have the most where hot and dry climates were found to have the least. A correlation between the clearness index and temperature fluctuations is established. Days where the mean instantaneous clearness index are between 0.1 - 0.3 or 0.7 - 0.9 (over cast or clear sky, respectively), fewer module temperature fluctuations occur than in days where the mean instantaneous clearness index is between 0.4 - 0.6, which can be characterised as intermittently cloudy. In addition to the total number of ramping events, the mean daily maximum ramping event size is also considered. It is found that hotter environments, particularly the hot and dry environments, have the highest mean daily maximum ramping event sizes, which is later shown to have a significant impact on solder bond damage accumulation. Absolute temperatures are also examined in anticipation that they will influence the thermomechanical behaviour of modules, particularly influencing the viscoelastic properties of the polymer encapsulants.

The thermomechanical behaviour of PV mini-modules is simulated using FEM techniques. Modules are shown to deform with a bending moment at the temperature extremes of -40 and 85 °C, with a maximum displacement of up to 3 mm. Deformation is shown to be caused by the large mismatch in thermal expansion coefficient the between backsheet and glass. Restrictions on the backsheets freedom to expand or contract as required results in the generation of tensile stresses and strains which pulls on the glass, causing the observed bending. The displacement of the cells and the mismatched thermal expansion coefficients is shown to generate shear stresses on the solder bonds, which contributes to the accumulation of damage of the bonds. It is shown that for one year of exposure of normal operating conditions in the outdoors, hot and dry environments such as those found in the Namibian desert or Saudi Arabia are most detrimental to solder bonds, resulting in the highest accumulation of inelastic strain energy (damage). Whilst mean maximum module temperature and total

number of ramping events is shown to influence the accumulation of solder bond damage, a strong correlation was found between accumulated damage and the mean daily maximum ramping event size. In addition to this, simulations were conducted to evaluate the accumulation of damage during IEC61215s thermal cycling program. By comparing the damage accumulated per cycle and the damage accumulated in the outdoor locations it was possible to determine an equivalent number of thermal cycles for one year of exposure in each location, where the highest damaging location would require 86 thermal cycles to replicate and the lowest would require 11. Whilst this equivalence was useful for comparing 1 year, there is a caveat in that the simulations do not consider the degradation of other components such as the backsheet or encapsulant. After extended use in the outdoors, the degradation of these components changes their mechanical properties, which in turn affects the thermomechanical behaviour of the module. The degradation of other components and the changing material properties over time should be considered for longer term evaluations.

The degradation of solder bonds in different climates was shown for modules with a common design and material selection. In anticipation that changing the materials would also change the behaviour and degradation potential a study was conducted looking at different encapsulants. The viscoelastic properties of 5 different polymers used for encapsulation has been shown to have an effect on the strains generated during normal operating conditions and therefore influences the potential for solder bond degradation. It is shown that the intended deployment environment could inform the selection of the encapsulant, with some materials providing greater thermomechanical stability than others at specific temperatures and temperature fluctuation profiles.

The work presented in this thesis has provided a greater insight into the thermomechanical behaviour and climate-specific degradation potential for PV

modules. It has determined that a strong correlation exists between the size of temperature ramping events and the accumulated damage of solder bonds.

As shown in this work, the stresses generated on the solder bonds is a result of the interactions between each of the components within the module. The majority of the simulations were conducted using the properties of virgin materials and the accumulation of damage is calculated assuming constant material properties throughout. In reality, exposure to environmental conditions would affect the material properties of all components in the module. This would be particularly true of the backsheet and encapsulant which can undergo changing viscoelastic properties following exposure to humidity, UV and temperature. It has already been demonstrated in this work that different viscoelastic properties have an influence on the degradation of solder bonds. In the future, it would be worth considering the evolving nature of the stresses applied to the solder with aged encapsulation since the damage generated in a fresh module would likely not be the same in an aged module. As an example, Badie et al [102] demonstrated a decreasing storage modulus for EVA following thermal ageing. The effects this has on the solder should be examined.

Whilst the influence of different types of encapsulants was examined consideration should also be given to other component materials such as solder alloy, ribbons, glass and backsheet. The Restrictions of Hazardous Substances Directive 2002/95/EC is a motion by the European Union to restrict the use of, amongst other things, lead in solder alloys. As such, there is motive to make use of lead-free solder alloys, the most common being Sn3.0Ag0.5Cu [103]. The mechanical properties and viscoplastic response is commonly thought to result in a less reliable bond when subject to thermal cycling, however, this is disputed and it has been shown that within temperature limits of 0°C and 100°C, lead-free solders were more reliable than leaded solders. Given that real-world PV module operating temperatures largely fall within those

limits, it would be worth examining the durability of those solders for real-world conditions. If found to be more reliable then leaded solder under real operating conditions, then the argument could be put forward that the already-unrealistic lower limit temperature of -40°C in the standard thermal cycling test should be amended as it subjects the solder to stress not seen in the field.

Further arguments towards to amendment of the lower limit for the standard thermal cycling test can be made when considering the encapsulant. Persistent cycling through -40°C forces the encapsulant to repeatedly pass through the glass transition region. While it is currently unknown what effect this has on the properties of the encapsulant, it has been shown in this work that such conditions are unrealistic and is likely placing unnecessary stresses on the encapsulant.

It is the opinion of the author that increasing the lower limits for the standard thermal cycling test should be considered. Increasing the lower limit to somewhat more realistic temperatures, such as -20°C, will remove the uncertainty of placing unrealistic stress on both encapsulant and solder. In addition, this could reduce the costs and capital requirements for testing, which become more significant when required to cool to -40°C.

One of the main outcomes of this work was the demonstration that 200 standard thermal cycles, as mandated in IEC61215, grossly underestimates the damage accumulated in the outdoors, particularly for Hot & Dry conditions such as those found in Namibia or Saudi Arabia. Placing a 25-year warranty on modules in such environments based on TC200 is entirely unjustified given that the damage accumulation following 200 thermal cycles could be equivalent to less than 3 years of outdoor exposure. For the most damaging environments, up to 1500 cycles could be recommended, however, the cost of conducting such tests becomes high. A classification system which guarantees modules for specific use-environments could

be more appropriate. Manufacturers who wish to guarantee their modules for Hot & Dry conditions would be required to conduct the extended thermal cycling tests and manufacturers wishing to only guarantee for temperate conditions could run fewer thermal cycles and be placed under a different classification. It is the opinion of the author that modules design and material selection should be informed by the intended use-environment.

Publications

Conference Publications

M. Owen-Bellini, J. Zhu, T. R. Betts, R. Gottschalg, Environmental Stress Potentials of Different Climatic Regions, *31st European Photovoltaic Solar Energy Conference and Exhibition (31st EUPVSEC),* Hamburg, Germany, 2015

M. Owen-Bellini, J. Zhu, T. R. Betts, R. Gottschalg, Module Temperature Stress Potentials in the UK: What is most relevant?, *12th Photovoltaic Science Application and Technology (PVSAT-12)*, Liverpool, UK, 2016

M. Owen-Bellini, J. Zhu, T. R. Betts, R. Gottschalg, Thermo-Mechanical Stresses of Silicon Photovoltaic Modules, *13th Photovoltaic Science Application and Technology (PVSAT-12)*, Bangor, UK, 2017

M. Owen-Bellini, D. Montiel-Chicharro, J. Zhu, T. R. Betts, R. Gottschalg, Influence of Viscoelastic Properties of Encapsulation Materials on the Thermomechanical Behavior of Photovoltaic Modules, *IEEE 44th Photovoltaic Specialists Conference (PVSC-44)*, Washington D.C., USA, 2017

J. Zhu, M. Owen-Bellini, D. Montiel-Chicharro, T .R. Betts, R. Gottschalg, Effect of viscoelasticity of EVA encapsulants on photovoltaic module solder joint degradation due to thermomechanical fatigue, *27th International Photovoltaic Science and Engineering Conference, 2017*

Journal Publications

M. Owen-Bellini, D. Montiel-Chicharro, J. Zhu, T. R. Betts, R. Gottschalg, Influence of Viscoelastic Properties of Encapsulation Materials on the Thermomechanical Behavior of Photovoltaic Modules, *IEEE Journal of Photovoltaics*, 2017

J. Zhu, D. Montiel-Chicharro, M. Owen-Bellini, T. R. Betts, R. Gottschalg, Does current injection during environmental stress testing accelerate the target degradation mechanisms?, *Japanese Journal of Applied Physics*, 2017

References

[1] International Electrotechnical Commision, "IEC 61215: Crystalline Silicon Terrestrial Photovoltaic (PV) Modules—Design Qualification and Type Approval," *International Electrotechnical Commission*, vol. 3. 2005.

[2] J. Wohlgemuth and S. Kurtz, "Photovoltaic Module Qualification Plus Testing," *Proc. 40th IEEE Photovoltaics Spec. Conf.*, pp. 3589–3594, 2014.

[3] S. Djordjevic, D. Parlevliet, and P. Jennings, "Detectable faults on recently installed solar modules in Western Australia," *Renew. Energy*, vol. 67, pp. 215–221, 2014.

[4] P. Hacke, K. Terwilliger, R. Smith, S. Glick, J. Pankow, M. Kempe, S. K. I. Bennett, and M. Kloos, "System voltage potential-induced degradation mechanisms in PV modules and methods for test," *Proc. 37th IEEE Photovolt. Spec. Conf.*, pp. 814–820, Jun. 2011.

[5] D. C. Jordan, T. J. Silverman, B. Sekulic, and S. R. Kurtz, "PV degradation curves: non-linearities and failure modes," *Prog. Photovoltaics Res. Appl.*, vol. 25, no. 7, pp. 583–591, 2017.

[6] J. M. Kuitche, R. Pan, and G. Tamizhmani, "Investigation of dominant failure mode(s) for field-aged crystalline silicon PV modules under desert climatic conditions," *IEEE J. Photovoltaics*, vol. 4, no. 3, pp. 814–826, 2014.

[7] B. Li, T. Arends, J. Kuitche, W. Shisler, Y. Kang, and G. Tamizhmani, "21st European Photovoltaic Solar Energy Conference , 4-8 September 2006 , Dresden , Germany 21st European Photovoltaic Solar Energy Conference , 4-8 September 2006 , Dresden , Germany," no. September, pp. 2078–2080, 2006.

[8] "Photovoltaics Report," Freiburg, Germany, 2016.

[9] M. Green, "Crystalline Silicon Solar Cells," in *Clean Electricity from PhotoVoltaics*, 2001, pp. 1–49.

[10] A. Gabor, M. Ralli, S. Montminy, L. Alegria, C. Bordonaro, J. Woods, and L. Felton, "Soldering induced damage to thin Si solar cells and detection of cracked cells in modules," *21st Eur. Photovolt. Sol. Energy Conf.*, 2006.

[11] B. Lee, J. Z. Liu, B. Sun, C. Y. Shen, and G. C. Dai, "Thermally conductive and

electrically insulating EVA composite encapsulant for solar photovoltaic (PV) cell," *Express Polym. Lett.*, vol. 2, no. 5, pp. 357–363, 2008.

[12] M. Kempe, "Overview of scientific issues involved in selection of polymers for PV applications," in *Proceedings of 37th IEEE Photovoltaic Specialists Conference*, 2011, pp. 85–90.

[13] K. R. Mcintosh, J. N. Cotsell, J. S. Cumpston, A. W. Norris, N. E. Powell, and B. M. Ketola, "An optical comparison of silicone and EVA encapsulants for conventional silicon PV modules : a ray-tracing study," in *Proceedings of 34th IEEE Photovoltaic Specialists Conference*, 2009, pp. 544–549.

[14] R. G. Ross and M. I. Smokler, "Flat-Plate Solar Array Project: Final Report: Volume VI," *Eng. Sci. Reliab.*, 1986.

[15] K. Agroui and G. Collins, "Characterisation of EVA encapsulant material by thermally stimulated current technique," *Sol. Energy Mater. Sol. Cells*, vol. 80, no. 1, pp. 33–45, Oct. 2003.

[16] F. Pern, "Ethylene vinyl acetate (EVA) encapsulants for photovoltaic modules: Degradation and discoloration mechanisms and formulation modifications for improved," *Die Angew. Makromol. Chemie*, vol. 252, pp. 195–216, 1997.

[17] B. Koll, "Alternative Interlayer for glazing-integrated PV," in *Proc. 21st European Photovoltaic Solar Energy Conference and Exhibition*, 2008.

[18] M. Kempe, "Evaluation of encapsulant materials for PV applications," *Photovoltaics Int.*, vol. 9, 2010.

[19] S. C. Pop, "Ionomer-based PID-resistant encapsulant for PV modules," in *Proc. 29th European Photovoltaic Solar Energy Conference and Exhibition*, 2014.

[20] J. Kapur, K. M. Stika, C. S. Westphal, J. L. Norwood, and B. Hamzavytehrany, "Prevention of Potential-Induced Degradation With Thin Ionomer Film," *IEEE J. Photovoltaics*, vol. 5, no. 1, pp. 219–223, 2015.

[21] M. C. Alonso-García, J. M. Ruiz, and F. Chenlo, "Experimental study of mismatch and shading effects in the I-V characteristic of a photovoltaic module," *Sol. Energy Mater. Sol. Cells*, vol. 90, no. 3, pp. 329–340, 2006.

[22] R. G. Ross, "PV Reliability Development Lessons From JPL Flat Plate Solar Array Project," *IEEE J. Photovoltaics*, vol. 4, no. 1, pp. 291–298, 2014.

[23] G. J. Ã. Jorgensen, K. M. Terwilliger, J. A. Delcueto, S. H. Glick, M. D. Kempe, J. W. Pankow, F. J. Pern, and T. J. Mcmahon, "Moisture transport , adhesion , and corrosion protection of PV module packaging materials," *Sol. Energy Mater. Sol.*

Cells, vol. 90, pp. 2739–2775, 2006.

[24] M. Kempe, "Design Criteria for Photovoltaic Back-Sheet and Front-Sheet Materials," *Photovoltaics Int.*, vol. 2, 2008.

[25] M. Chang, C. Chen, C. H. Hsueh, W. J. Hsieh, E. Yen, K. L. Ho, H. P. Chuang, C. Y. Lee, and H. Chen, "The Reliability Investigation of PV Junction Box based on 1GW Worldwide Field Database," in *Proceedings of 42nd IEEE Photovoltaic Specialist Conference*, 2015, pp. 6–9.

[26] M. I. Smokler, D. H. Otth, and R. G. Ross, "The block program approach to photovoltaic module development," in *Proceedings of 18th IEEE Photovoltaics Specialist Conference*, 1985, pp. 1150–1158.

[27] J. H. Wohlgemuth, D. W. Cunningham, P. Monus, J. Miller, and A. Nguyen, "Long term reliability of photovoltaic modules," *Conf. Rec. 2006 IEEE 4th World Conf. Photovolt. Energy Conversion, WCPEC-4*, vol. 2, pp. 2050–2053, 2007.

[28] M. A. Quintana, D. L. King, T. J. McMahon, and C. R. Osterwald, "Commonly observed degradation in field-aged photovoltaic modules," in *Proceedings of 29th IEEE Photovoltaic Specialist Conference*, 2002, pp. 1436–1439.

[29] J. Singh, J. Belmont, and G. Tamizhmani, "Degradation analysis of 1900 PV modules in a hot-dry climate: Results after 12 to 18 years of field exposure," *Proc. 39th IEEE Photovoltaics Spec. Conf.*, pp. 3270–3275, 2013.

[30] K. Yedidi, J. Mallineni, B. Knisely, J. Kutiche, and G. Tamizhmani, "Failure and Degradation Modes and Rates of PV Modules in a Hot-Dry Climate: Results after 16 years of field exposure," in *Proceedings of 40th IEEE Photovoltaics Specialists Conference*, 2014, pp. 3245–3247.

[31] D. C. Jordan, J. H. Wohlgemuth, and S. R. Kurtz, "Technology and climate trends in pv module degradation," *27th Eur. Photovolt. Sol. Energy Conf. Exhib.*, no. October, pp. 3118–3124, 2012.

[32] M. A. Quintana, D. L. King, F. M. Hosking, J. A. Kratochvil, R. W. Johnson, B. R. Hansen, N. G. Dhere, and M. B. Pandit, "Diagnostic analysis of silicon photovoltaic modules after 20-year field exposure," *Conf. Rec. Twenty-Eighth IEEE Photovolt. Spec. Conf. - 2000 (Cat. No.00CH37036)*, pp. 1420–1423, 2000.

[33] D. L. King, M. A. Quintana, J. A. Kratochvil, D. E. Ellibee, and B. R. Hansen, "Photovoltaic module performance and durability following long-term field exposure," *Prog. Photovoltaics Res. Appl.*, vol. 8, no. 2, pp. 241–256, 2000.

[34] D. L. King, M. A. Quintana, J. A. Kratochvil, D. E. Ellibee, and B. R. Hansen,

"Photovoltaic module performance and durability following long-term field exposure," *AIP Conf. Proc.*, pp. 565–571, 1999.

[35] J.-S. Jeong, N. Park, and C. Han, "Field failure mechanism study of solder interconnection for crystalline silicon photovoltaic module," *Microelectron. Reliab.*, vol. 52, no. 9–10, pp. 2326–2330, Sep. 2012.

[36] G. Shaur, "Long term stability of PV-modules, damage cases and damage analyses," in *16th European photovoltaic solar energy conference and exhibition*, 2000.

[37] R. Meier, F. Kraemer, S. Wiese, K. Wolter, J. Bagdahn, P. Csp, and H. Saale, "Reliability of copper-ribbons in photovoltaic modules under thermo-mechanical loading," in *Proceedings of 35th IEEE Photovoltaics Specialists Conference*, 2010, pp. 1283–1288.

[38] J. Muñoz, E. Lorenzo, F. Martínez-Moreno, L. Marroyo, and M. García, "An investigation into hot-spots in two large grid-connected PV plants," *Prog. Photovoltaics Res. Appl.*, vol. 16, no. 8, pp. 693–701, Dec. 2008.

[39] J. Wohlgemuth and W. Herrmann, "Hot Spot Tests for Crystalline Silicon Modules," *Photovolt. Spec. Conf. 2005. Conf. Rec. Thirty-first IEEE*, no. 1, pp. 1062–1063, 2005.

[40] M. Paggi, I. Berardone, A. Infuso, and M. Corrado, "Fatigue degradation and electric recovery in Silicon solar cells embedded in photovoltaic modules," *Sci. Rep.*, vol. 4, pp. 1–7, 2014.

[41] N. Park, J. Jeong, and C. Han, "Estimation of the degradation rate of multi-crystalline silicon photovoltaic module under thermal cycling stress," *Microelectron. Reliab.*, vol. 54, no. 8, pp. 1562–1566, 2014.

[42] M. Sander, S. Dietrich, M. Pander, M. Ebert, and J. Bagdahn, "Systematic investigation of cracks in encapsulated solar cells after mechanical loading," *Sol. Energy Mater. Sol. Cells*, vol. 111, pp. 82–89, Apr. 2013.

[43] S. Pingel, Y. Zemen, O. Frank, T. Geipel, and J. Berghold, "Mechanical stability of solar cells within solar panels," in *Proceedings of 24th European PV Solar Energy Conference*, 2009, pp. 3459–3464.

[44] F. Reil, J. Althaus, W. Vaassen, W. Herrmann, and K. Strohkendl, "The effect of transportation impacts and dynamic load tests on the mechanical and electrical Behaviour of Crystalline PV Modules," in *25th European PV Solar Energy Conference*, 2010, pp. 3989–3992.

[45] M. Köntges, S. Kajari-Schröder, I. Kunze, and U. Jahn, "Crack Statistic of

Crystalline Silicon Photovoltaic Modules," in *Proceedings of 25th European PV Solar Energy Conference*, 2011, vol. 26, pp. 3290–3294.

[46] M. Assmus, S. Jack, K.-A. Weiss, and M. Koehl, "Measurement and simulation of vibrations of PV-modules induced by dynamic mechanical loads," *Prog. Photovoltaics Res. Appl.*, vol. 19, no. 6, pp. 688–694, Sep. 2011.

[47] M. Kontges, I. Kunze, S. Kajari-Schroder, X. Breitenmoser, and B. Bjørneklett, "The risk of power loss in crystalline silicon based photovoltaic modules due to micro-cracks," *Sol. Energy Mater. Sol. Cells*, vol. 95, no. 4, pp. 1131–1137, Apr. 2011.

[48] S. Kajari-Schröder, I. Kunze, and M. Köntges, "Criticality of cracks in PV modules," *Energy Procedia*, vol. 27, pp. 658–663, Jan. 2012.

[49] S. Kajari-Schroder, I. Kunze, U. Eitner, and M. Kontges, "Spatial and orientational distribution of cracks in crystalline photovoltaic modules generated by mechanical load tests," *Sol. Energy Mater. Sol. Cells*, vol. 95, no. 11, pp. 3054–3059, Nov. 2011.

[50] S. Kurtz, J. Wohlgemuth, T. Sample, M. Yamamichi, J. Amano, P. Hacke, and M. Kempe, "Ensuring Quality of PV Modules," in *37th IEEE Photovoltaics Specialist Conference*, 2011, pp. 842–847.

[51] V. Saly, M. Ruzinsky, and P. Redi, "Accelerated testing of small Photovoltaic modules and encapsulations at elevated voltage, temperature and humidity," in *7th European PV Solar Energy Conference*, 2001.

[52] K. R. McIntosh, N. E. Powell, A. W. Norris, J. N. Cotsell, and B. M. Ketola, "The effect of damp-heat and UV aging tests on the optical properties of silicone and EVA encapsulants," *Prog. Photovoltaics Res. Appl.*, vol. 19, no. 3, pp. 294–300, May 2011.

[53] M. V. Konidari, K. G. Papadokostaki, and M. Sanopoulou, "Moisture-induced effects on the tensile mechanical properties and glass-transition temperature of poly(vinyl alcohol) films," *J. Appl. Polym. Sci.*, vol. 120, no. 6, pp. 3381–3386, Jun. 2011.

[54] M. D. Kempe, G. J. Jorgensen, K. M. Terwilliger, T. J. McMahon, C. E. Kennedy, and T. T. Borek, "Acetic acid production and glass transition concerns with ethylene-vinyl acetate used in photovoltaic devices," *Sol. Energy Mater. Sol. Cells*, vol. 91, no. 4, pp. 315–329, 2007.

[55] F. J. Pern, "Luminescence and absorption characterization of ethylene-vinyl acetate encapsulant for PV modules before and after weathering degradation,"

Polym. Degrad. Stab., vol. 41, no. 2, pp. 125–139, 1993.

[56] F. J. Pern, C. Branch, and N. Renewable, "Factors that affect the EVA encapsulant upon accelerated exposure," in *1st World Conference on Photovoltaic Energy Conversion*, 1994, pp. 897–900.

[57] M. M. Kusato Hirota and T. Amioka, "Durability test of Poly-Ethylen-Terephtalate (PET) film for backsheet," in *NREL PV Module Reliability Workshop*, 2011.

[58] N. Kim, H. Kang, K. J. Hwang, C. Han, W. S. Hong, D. Kim, E. Lyu, and H. Kim, "Study on the degradation of different types of backsheets used in PV module under accelerated conditions," *Sol. Energy Mater. Sol. Cells*, vol. 120, no. PART B, pp. 543–548, Jan. 2014.

[59] F. Liu, L. Jiang, and S. Yang, "Ultra-violet degradation behavior of polymeric backsheets for photovoltaic modules," *Sol. Energy*, vol. 108, pp. 88–100, 2014.

[60] G. Oreski and G. M. Wallner, "Aging mechanisms of polymeric films for PV encapsulation," *Sol. Energy*, vol. 79, no. 6, pp. 612–617, Dec. 2005.

[61] J. H. Wohlgemuth and S. R. Kurtz, "Using Accelerated Testing to Predict Module Reliability," in *Proceedings of 37th IEEE Photovoltaic Specialists Conference*, 2011.

[62] B. Jaeckel, A. Krtschil, D. Cunningham, N. Forney, C. LaMothe, A. Nguyen, M. Disser, and A. Roth, "A New Standard for Holistic Quality Assurance," in *Proceedings of 26th European PV Solar Energy Conference*, 2011, pp. 3484–3490.

[63] D. Meakin, "Photovoltaic durability initiative (PVDI): a durability program providing bankability and marketing leverage," in *PV Module Reliability Workshop*, 2012.

[64] A. Funcell, "The thresher test: crystalline silicon terrestrial photovoltaic modules long term reliability and degradation," in *PV Module Reliability Workshop*, 2012.

[65] D. C. Jordan, T. J. Silverman, B. Sekulic, and S. R. Kurtz, "PV Degradation Curves: Non-Linearities and Failure Modes," in *Proceedings of 32nd European PV Solar Energy Conference and Exhibition*, 2016.

[66] D. C. Jordan, T. J. Silverman, J. H. Wohlgemuth, S. R. Kurtz, and K. T. VanSant, "Photovoltaic failure and degradation modes," *Prog. Photovoltaics Res. Appl.*, vol. 25, no. 4, pp. 318–326, Apr. 2017.

[67] D. C. Jordan, S. R. Kurtz, K. Vansant, and J. Newmiller, "Compendium of

photovoltaic degradation rates," *Prog. Photovoltaics Res. Appl.*, vol. 24, no. February 2016, pp. 978–989, 2016.

[68] P. L. Hacke, A. F. Sprecher, and H. Conrad, "Microstructure coarsening during thermo-mechanical fatigue of Pb-Sn solder joints," *J. Electron. Mater.*, vol. 26, no. 7, 1997.

[69] D. R. Frear, "Thermomechanical Fatigue of Solder Joints : A New Comprehensive Test Method," *IEEE Trans. Components, Hybrids, Manuf. Technol.*, vol. 12, no. 4, pp. 492–501, 1989.

[70] L. Anand, "Constitutive equations for hot-working of metals," *Int. J. Plast.*, vol. 1, no. 3, pp. 213–231, 1985.

[71] D. L. Evans, "Simplified method for predicting photovoltaic array output," *Sol. Energy*, vol. 27, no. 6, pp. 555–560, 1981.

[72] E. Skoplaki and J. A. Palyvos, "Operating temperature of photovoltaic modules: A survey of pertinent correlations," *Renew. Energy*, vol. 34, no. 1, pp. 23–29, Jan. 2009.

[73] M. Mattei, G. Notton, C. Cristofari, M. Muselli, and P. Poggi, "Calculation of the polycrystalline PV module temperature using a simple method of energy balance," vol. 31, pp. 553–567, 2006.

[74] M. Servant, "Calculation of the cell temperature for photovoltaic modules from climatic data," in *Proceedings of the 9th biennial congress of the Intenrational Solar Eenergy Society*, 1985.

[75] S. Boddar and F. Chervet, "Long-term experimental validation of NOCT method for PV integration under several conditions," in *Proc. 27th European Photovoltaic Solar Energy Conference*, 2012.

[76] M. Koehl, M. Heck, S. Wiesmeier, and J. Wirth, "Modeling of the nominal operating cell temperature based on outdoor weathering," *Sol. Energy Mater. Sol. Cells*, vol. 95, no. 7, pp. 1638–1646, Jul. 2011.

[77] D. Faiman, "Assessing the Outdoor Operating Temperature of Photovoltaic Modules," *Prog. Photovoltaics Res. Appl.*, no. 16, pp. 307–315, 2008.

[78] R. G. Ross, "Interface design considerations for terrestrial solar cell modules," in *Proceedings of 12th IEEE Photovoltaics Specialist Conference*, 1976.

[79] D. L. King, J. A. Kratochvil, and W. E. Boyson, "Photovoltaic array performance model," Report, 2004.

[80] M. K. Fuentes, "A Simplified Thermal Model for Flat-Plate Photovoltaic Arrays," *Sandia Report*. Sandia National Laboratories, 1987.

[81] W. C. Swinbank, "Long-wave radiation from clear skies," *Q. J. R. Meterological Soc.*, vol. 90, no. 386, pp. 488–493, 1964.

[82] B. Liu and R. Jordan, "Daily insolation on surfaces tilted towards equator," *Trans. ASHRAE*, vol. 10, pp. 53–59, 1961.

[83] K. I. M. McKinnon, "Convergence of the Nelder--Mead Simplex Method to a Nonstationary Point," *SIAM J. Optim.*, vol. 9, no. 1, pp. 148–158, 1998.

[84] A. Ohmura, E. G. Dutton, B. Forgan, H. Gilgen, H. Hegner, A. Heimo, G. Konig-Langlo, B. McArthur, G. Muller, R. Philipona, R. Pinker, C. H. Whitlock, K. Dehne, and M. Wild, "Baseline Surface Radiation Network (BSRN/WCRP): New Precision Radiometry for Climate Research," *Bull. Am. Meteorol. Soc.*, vol. 79, no. 10, pp. 2115–2136, 1998.

[85] S. Chattopadhyay, R. Dubey, V. Kuthanazhi, J. J. John, C. S. Solanki, A. Kottantharayil, B. M. Arora, K. L. Narasimhan, J. Vasi, B. Bora, Y. K. Singh, and O. S. Sastry, "All India Survey of Photovoltaic Module Degradation 2014: Survey methodology and statistics," *Proc. 42nd IEEE Photovolt. Spec. Conf.*, 2015.

[86] S. Kurtz, K. Whitfield, G. Tamizhmani, M. Koehl, D. Miller, J. Joyce, J. Wohlgemuth, N. Bosco, M. Kempe, and T. Zgonena, "Evaluation of high-temperature exposure of photovoltaic modules," *Prog. Photovoltaics Res. Appl.*, vol. 19, no. 8, pp. 954–965, 2011.

[87] N. Bosco and S. Kurtz, "Quantifying the Weather: an analysis for thermal fatigue," *Renew. Energy*, 2010.

[88] N. Bosco, T. J. Silverman, and S. Kurtz, "Climate specific thermomechanical fatigue of flat plate photovoltaic module solder joints," *Microelectron. Reliab.*, vol. 62, pp. 124–129, 2016.

[89] A. Ramakrishnan and M. G. Pecht, "A Life Consumption Monitoring Methodology for Electronic Systems," *IEEE Trans. Components Packag. Technol.*, vol. 26, no. 3, pp. 625–634, 2003.

[90] P. Liu, Y. Gao, Q. Cao, Z. Xia, Y. Lei, and F. Guo, "Effect of ramp rate on microstructure and properties of thermomechanically-fatigued Sn-3.5Ag based composite solder joints," *2006 7th Int. Conf. Electron. Packag. Technol. ICEPT '06*, pp. 3–7, 2007.

[91] T.-Y. Pan, "Thermal Cycling Induced Plastic Deformation in Solder Joints—Part

I: Accumulated Deformation in Surface Mount Joints," *J. Electron. Packag.*, vol. 113, no. 1, p. 8, 1991.

[92] A. Woyte, R. Belmans, and J. Nijs, "Fluctuations in instantaneous clearness index: Analysis and statistics," *Sol. Energy*, vol. 81, no. 2, pp. 195–206, 2007.

[93] U. Eitner, M. Kontges, and R. Brendel, "Use of digital image correlation technique to determine thermomechanical deformations in photovoltaic laminates: Measurements and accuracy," *Sol. Energy Mater. Sol. Cells*, vol. 94, no. 8, pp. 1346–1351, Aug. 2010.

[94] "Mechanical properties of glass," *J. Non. Cryst. Solids*, vol. 25, no. 1–3, pp. 293–321, Sep. 1977.

[95] O. Goodman and B. Derby, "The mechanical properties of float glass surfaces measured by nanoindentation and acoustic microscopy," *Acta Mater.*, vol. 59, no. 4, pp. 1790–1799, 2011.

[96] U. Eitner, M. Köntges, and R. Brendel, "Measuring thermomechanical displacements of solar cells in laminates using digital image correlation," pp. 1280–1284, 2009.

[97] J. J. Wortman and R. A. Evans, "Young's Modulus, Shear Modulus, and Poisson's Ratio in Silicon and Germanium," *J. Appl. Phys.*, vol. 36, no. 153, 1965.

[98] R. Hull, *Properties of crystalline silicon*. London: INSPEC, 1999.

[99] Z. N. Cheng, G. Z. Wang, L. Chen, J. Wilde, and K. Becker, "Viscoplastic Anand model for solder alloys and its application," *Solder. Surf. Mt. Technol.*, vol. 12, no. 2, pp. 31–36, 2000.

[100] R. Darveaux, "Effect of simulation methodology on solder joint crack growth correlation," *Proc. - Electron. Components Technol. Conf.*, vol. 124, no. September 2002, pp. 1048–1058, 2000.

[101] M. L. Williams, R. F. Landel, and J. D. Ferry, "The Temperature Dependence of Relaxation Mechanisms in Amorphous Polymers and Other Glass-forming Liquids.," *J. Am. Chem. Soc.*, vol. 77, no. 12, pp. 3701–3707, 1955.

[102] A. Badiee, I. A. Ashcroft, and R. D. Wildman, "The thermo-mechanical degradation of ethylene vinyl acetate used as a solar panel adhesive and encapsulant," *Int. J. Adhes. Adhes.*, vol. 68, pp. 212–218, 2016.

[103] S. Cheng, C. M. Huang, and M. Pecht, "A review of lead-free solders for electronics applications," *Microelectron. Reliab.*, vol. 75, pp. 77–95, 2017.